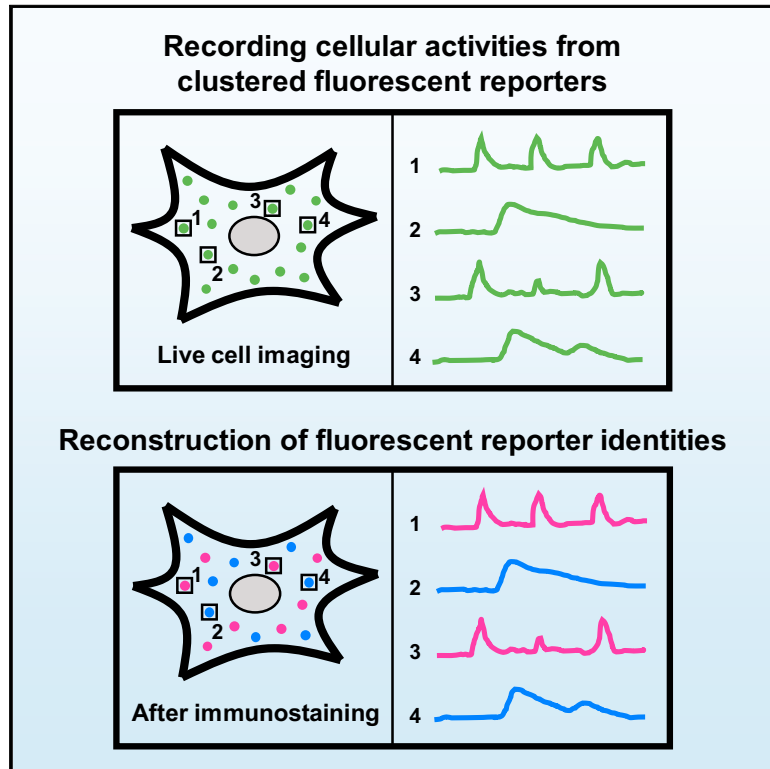


Spatial Multiplexing of Fluorescent Reporters for Imaging Signaling Network Dynamics

Graphical Abstract



Authors

Changyang Linghu, Shannon L. Johnson, Pablo A. Valdes, ..., Mark F. Bear, Amy E. Keating, Edward S. Boyden

Correspondence

edboyden@mit.edu

In Brief

Simultaneous signals such as second messengers and kinase activities, within a single cell, can be captured through the fusion of fluorescent reporters to pairs of self-assembling peptides to generate stable signaling reporter islands.

Highlights

- Clustering fluorescent sensors at points in cells enables many to be imaged at once
- Modular reagent design allows existing sensors to be easily adapted to cluster
- Such “signaling reporter islands” (SiRIs) are safe and robust in cells and *in vivo*
- SiRIs reveal relationships between components of signal transduction networks

Resource

Spatial Multiplexing of Fluorescent Reporters for Imaging Signaling Network Dynamics

Changyang Linghu,^{1,2,3,4,16} Shannon L. Johnson,^{1,2,3,16} Pablo A. Valdes,^{1,5} Or A. Shemesh,^{1,2,3,6,7,8} Won Min Park,⁹ Demian Park,^{1,2,3} Kiryl D. Piatkevich,^{1,2,3,6,7,10} Asmamaw T. Wassie,^{1,2,3,6} Yixi Liu,^{1,2,4,3} Bobae An,^{1,2,3,7} Stephanie A. Barnes,^{7,11} Orhan T. Celiker,^{1,2,3,4} Chun-Chen Yao,⁷ Chih-Chieh (Jay) Yu,^{1,2,3,6} Ru Wang,^{1,2,3} Katarzyna P. Adamala,¹² Mark F. Bear,^{7,11} Amy E. Keating,^{6,13,14} and Edward S. Boyden^{1,2,3,6,7,14,15,17,*}

¹Department of Media Arts and Sciences, Massachusetts Institute of Technology (MIT), Cambridge, MA 02139, USA

²McGovern Institute for Brain Research, MIT, Cambridge, MA 02139, USA

³Center for Neurobiological Engineering, MIT, Cambridge, MA 02139, USA

⁴Department of Electrical Engineering and Computer Science, MIT, Cambridge, MA 02139, USA

⁵Department of Neurosurgery, Harvard Medical School, Brigham and Women's Hospital, Boston, MA 02115, USA

⁶Department of Biological Engineering, MIT, Cambridge, MA 02139, USA

⁷Department of Brain and Cognitive Sciences, MIT, Cambridge, MA 02139, USA

⁸Department of Neurobiology and Pittsburgh Institute for Neurodegenerative Diseases, University of Pittsburgh School of Medicine, Pittsburgh, PA 15213, USA

⁹Tim Taylor Department of Chemical Engineering, Kansas State University, Manhattan, KS 66506, USA

¹⁰School of Life Sciences, Westlake University, Hangzhou, Zhejiang 310024, China

¹¹Picower Institute for Learning and Memory, MIT, Cambridge, MA 02139, USA

¹²Department of Genetics, Cell Biology and Development, University of Minnesota, Minneapolis, MN 55455, USA

¹³Department of Biology, MIT, Cambridge, MA 02139, USA

¹⁴Koch Institute, Massachusetts Institute of Technology, Cambridge, MA 02139, USA

¹⁵Howard Hughes Medical Institute, Cambridge, MA 02139, USA

¹⁶These authors contributed equally

¹⁷Lead Contact

*Correspondence: edboyden@mit.edu

<https://doi.org/10.1016/j.cell.2020.10.035>

SUMMARY

In order to analyze how a signal transduction network converts cellular inputs into cellular outputs, ideally one would measure the dynamics of many signals within the network simultaneously. We found that, by fusing a fluorescent reporter to a pair of self-assembling peptides, it could be stably clustered within cells at random points, distant enough to be resolved by a microscope but close enough to spatially sample the relevant biology. Because such clusters, which we call signaling reporter islands (SiRIs), can be modularly designed, they permit a set of fluorescent reporters to be efficiently adapted for simultaneous measurement of multiple nodes of a signal transduction network within single cells. We created SiRIs for indicators of second messengers and kinases and used them, in hippocampal neurons in culture and intact brain slices, to discover relationships between the speed of calcium signaling, and the amplitude of PKA signaling, upon receiving a cAMP-driving stimulus.

INTRODUCTION

Cells transform extracellular inputs into cellular outputs through signal transduction networks containing many interacting biomolecular components. For example, cells respond to certain extracellular signals by changing intracellular Ca^{2+} dynamics, cyclic AMP (cAMP) concentration, and protein kinase A (PKA) activity, which in turn can then result in a wide variety of cellular output states and functions (Bruce et al., 2003; Ferguson and Storm, 2004; Howe, 2011; Kandel et al., 2014; Waltereit and Weller, 2003). These intracellular signals can interact in complex ways, such as through feedback loops—for example, Ca^{2+} can

modulate adenylate cyclase (AC) production of cAMP, cAMP can activate PKA as well as cAMP-dependent ion channels, and PKA can then in turn modulate Ca^{2+} influx through altering ion channels and intracellular store release; such feedback loops can result in complex dynamics such as coordinated oscillations of Ca^{2+} , cAMP, and PKA activity or the creation of sustained signals downstream of an initial transient or oscillatory stimulus (Abrams et al., 1991; Borodinsky and Spitzer, 2006; Cooper et al., 1995; Mehta and Zhang, 2011; Murphy et al., 2014; Sassone-Corsi, 2012; Wong et al., 1999). Given that the Ca^{2+} /cAMP/PKA network governs many important biological phenomena ranging from the proliferation and differentiation of

cancer cells (Bhullar et al., 2018; Cho-Chung, 1990; Wang et al., 2006) to plasticity and learning in the nervous system (Averaimo and Nicol, 2014; Frey et al., 1993; Giese and Mizuno, 2013; Huang and Kandel, 1994; Lee et al., 1998; Roberson and David Sweatt, 1996; Shelly et al., 2010; Trudeau et al., 1996), understanding how this network computes a specific cellular output from a specific extracellular input is a high priority in biology. And of course, this is just one of countless signal transduction networks of importance in biology and medicine.

Not surprisingly, there has been a push by many bioengineers to create genetically encoded fluorescent reporters of these, and many other, biological signals (Belousov et al., 2006; Berg et al., 2009; Chen et al., 2013; Depry et al., 2011; Ding et al., 2015; Di-Pilato and Zhang, 2009; Hackley et al., 2018; Mehta et al., 2018; Oliveira and Yasuda, 2013; Shimozone et al., 2013; Vinkenborg et al., 2009; Violin et al., 2003). To reveal the relationships between the components of a signaling network, there is increasing desire to use multiple fluorescent reporters of different signals simultaneously, within the same living cell (Hackley et al., 2018; Mehta et al., 2018; Ohta et al., 2018). Imaging two different components of a signaling network in two different cells is rarely sufficient to reveal how they interact: relationships between the components of a signaling network are complex, with nonlinear couplings that may be very difficult to infer, if measurements of different components must be made in different cells. As a simple example, imagine a cell where when signal A increases in amplitude, it suppresses signal B, and when signal A decreases in amplitude, signal B increases. If A and B are measured in separate sets of cells, and then compared only after being averaged across their respective cell populations, the inverse relationship between A and B will be lost.

On a conventional fluorescence microscope, reporters with different fluorescent spectra can be used simultaneously but not reporters based on the same fluorophore, whose signals will mix and result in ambiguous data. Thus, the number of reporters used is limited to the number of spectrally resolvable channels on the microscope. If it were possible to stochastically assemble fluorescent reporters of different biological signals into distinct clusters, randomly located throughout a given cell, and if the clusters are distant enough from each other to be resolved by a microscope but close enough to spatially sample the relevant biology, it might be possible to image more biological signals in a single living cell than permitted by the number of spectrally resolvable channels on a microscope (Figure 1A). Even if the fluorescence spectra of the reporters overlap, or are identical, signals would be accurately reported because of their different locations in space. As long as the clusters stayed stationary during the live-cell imaging, identifying the signals could be done post hoc, after the live-cell imaging was over, by using highly multiplexed fixed-cell imaging methods to identify distinct tags bound to each of the different reporters (e.g., serial antibody staining against distinct immunopeptides fused to each of the distinct fluorescent reporters [Micheva and Smith, 2007; Murray et al., 2015]).

Here, we report that by fusing a given fluorescent reporter to a pair of bioorthogonal, human-designed, self-assembling peptides, we were able to cluster a fluorescent reporter into bright puncta that were stationary, in living cells, over timescales of

at least 1 h. Fusing a fluorescent reporter to just one self-assembling peptide did not result in bright puncta, so it is possible that equipping a reporter with a pair of self-assembling peptides is necessary to enable such reporters to connect to each other in meaningfully scalable ways (Figure 1B). By fusing different fluorescent reporters to different pairs of self-assembling peptides, they could be caused to stochastically cluster at different points in space, separated by micrometers, enabling dense sampling of signals throughout cells. After these fluorescent reporter puncta were imaged in living cells, in response to a cellular input, the identity of each fluorescent reporter could be identified post hoc through multi-round immunostaining against distinct immunopeptides associated with each fluorescent reporter.

We found this reporter clustering architecture, which we call a signaling reporter island (SiRI), to be very modular—that is, given a set of fluorescent reporters, one could reliably design a dual peptide-fused version of each, and then they could be used together within a living cell, with high robustness and safety, without needing laborious trial-and-error iteration. In contrast, engineering a set of fluorescent reporters from scratch so that they can be used together to simultaneously report on a given set of cellular signals, and that exhibit different spectra, requires a lot of effort, because the coupling between the sensor domain and the fluorophore must be optimized within each desired indicator, a process that can take a long time, and one not guaranteed to converge upon a positive outcome.

SiRI-scaffolded reporters possessed the same spectra, kinetics, and responsiveness as unscaffolded reporters and did not alter cell signals, cell health, or physiology. By clustering existing fluorescent reporters for important signals such as Ca^{2+} , cAMP, and PKA within individual cells, we show using cultured hippocampal neurons and brain slices from mice expressing SiRIs *in vivo* that we can derive relationships between the time dynamics of the second messenger Ca^{2+} , in response to a cAMP-driving cellular input stimulus, and the amplitude of enduring PKA signaling. In particular, neurons with faster Ca^{2+} responses upon the driving of cAMP exhibited higher-amplitude PKA signals than those with slower Ca^{2+} responses to cAMP stimulation. We further showed that we could image four, and even five, signals at once by expressing SiRIs containing fluorescent indicators of Ca^{2+} , cAMP, PKA, protein kinase C (PKC), and extracellular signal-regulated kinase (ERK) within single neurons. These inventions and results point to potential broad utility of the spatial multiplexing concept, and the SiRI protein architecture, in biological science.

RESULTS

Dual-Peptide-Based Protein Scaffolds for Assembling Fluorescent Reporters into Functional Clusters

Primary cultures of rodent hippocampal and cortical neurons have been critical for the study of signaling networks involving calcium, cAMP, and protein kinases (Bito et al., 1996; Hardingham et al., 2001; Redmond et al., 2002; Shelly et al., 2010; Sheng et al., 1991; Van der Zee and Douma, 1997), and thus we used them as a testbed for developing SiRIs based on scaffolds that would be bioorthogonal to endogenous signaling and trafficking functions (Figure 1B). We first tested whether short peptides that are

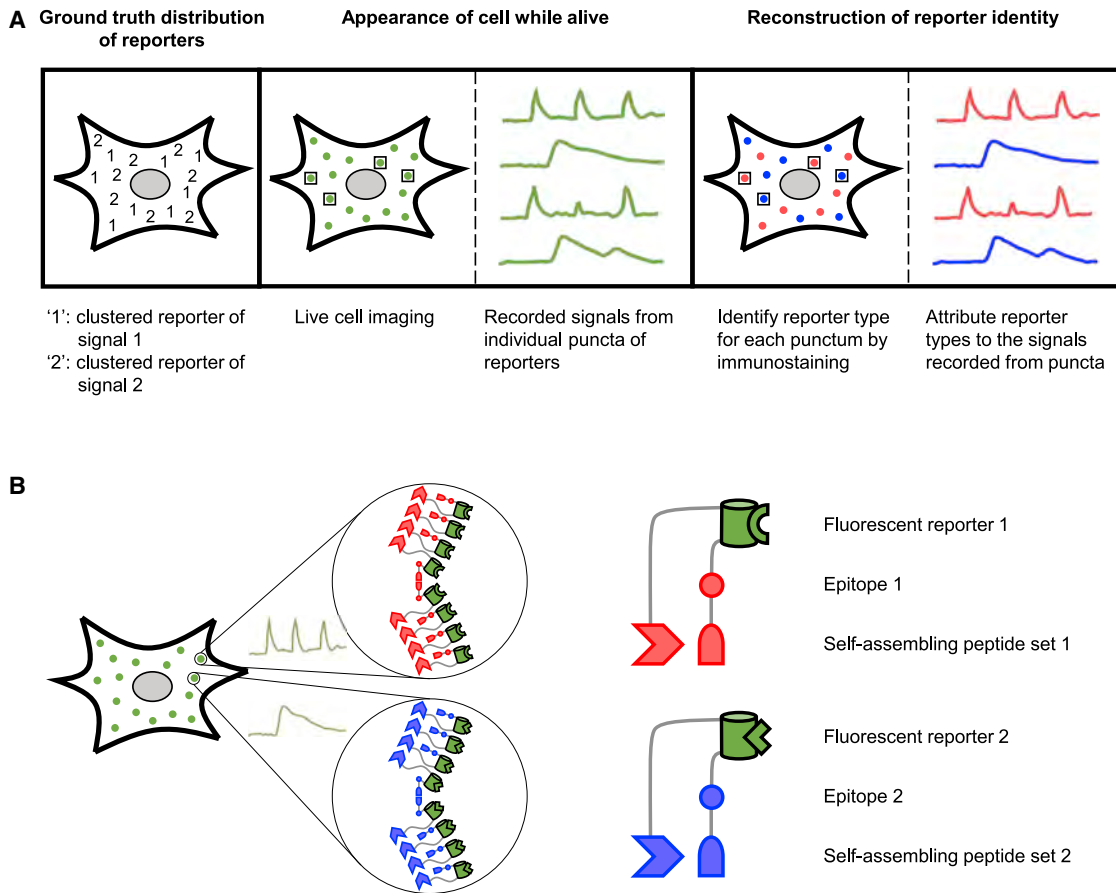


Figure 1. The SiRI Concept

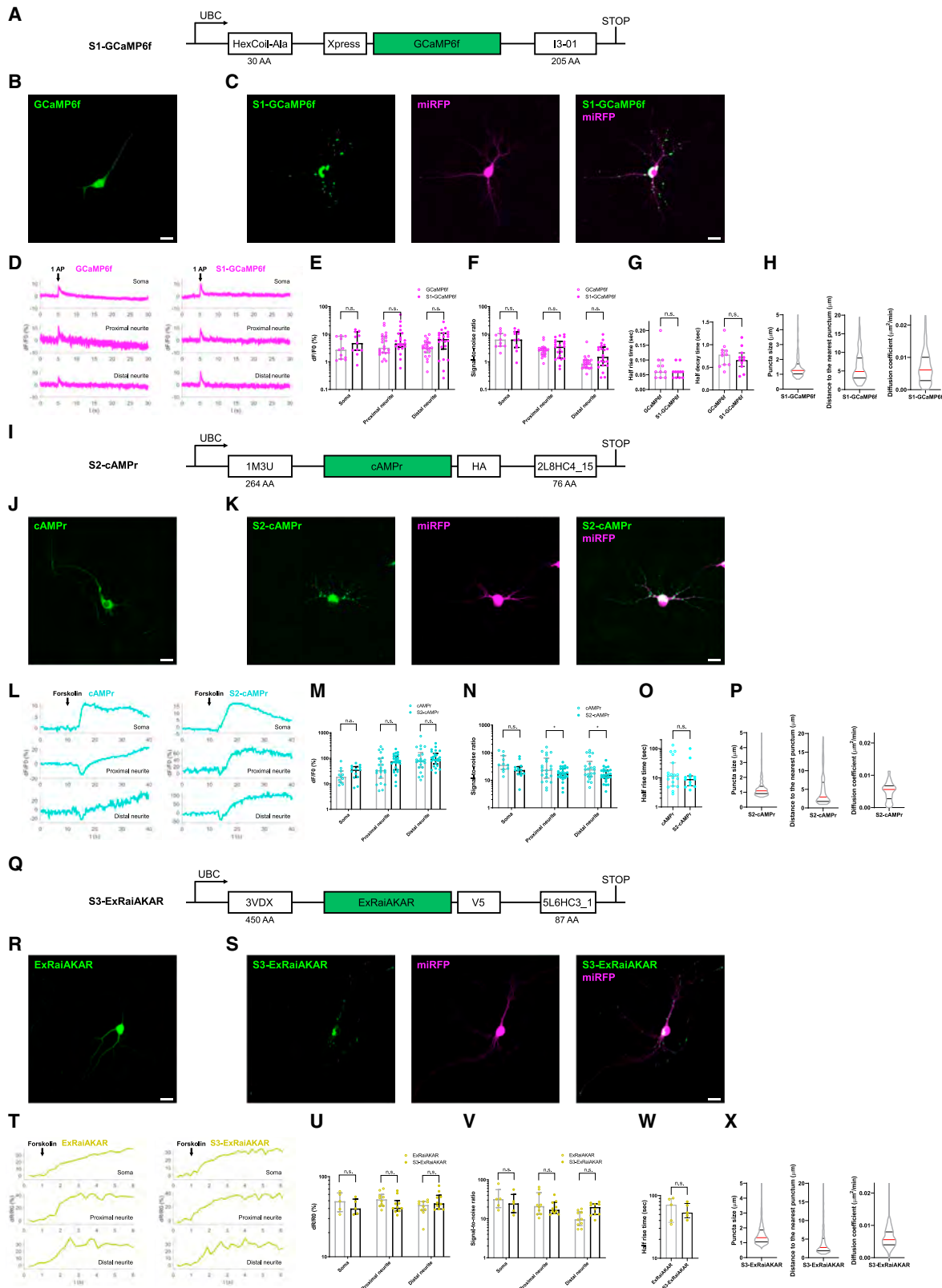
(A) Schematic of the concept. Green dots, live-cell appearance of puncta formed by clustered fluorescent reporters; black squares, regions-of-interest (ROIs) for time-course measurements; green traces, time-course measurements of fluorescent signals from ROIs; red and blue dots, identification of fluorescent reporter identity by multiplexed fixed-cell staining for tags fused to the fluorescent reporters; red and blue traces, the fluorescent signal time courses, now annotated with reporter identity.

(B) Schematic of how fluorescent reporter clustering could be achieved by fusing different fluorescent reporters to different self-assembling peptide pairs, with epitopes to enable post hoc multiplexed antibody staining.

de novo designed, bioorthogonal, self-assembling coiled-coil forming hetero-dimers (Boyle et al., 2012; Gradišar et al., 2013; Moll et al., 2001; Oakley and Kim, 1998; Shekhawat et al., 2009; Tripet et al., 1996), or homo-oligomers (Boyken et al., 2016; Chen et al., 2019; Fletcher et al., 2012; Grigoryan et al., 2011; Huang et al., 2014; Negron and Keating, 2014; Thomson et al., 2014; Zaccai et al., 2011; Zhang et al., 2018) could assemble fluorescent activity reporters into puncta. We fused 2–5 of these motifs to the N terminus or C terminus of GCaMP6f, a high-performance GFP-based Ca^{2+} indicator (Chen et al., 2013), with glycine and serine-rich flexible linkers adapted from Boyle et al., (2012) and Indelicato et al. (2016) (see Table S1 for sequences of all motifs; see Table S2 for all tested constructs and screening results). However, none of these constructs produced resolvable puncta in neurons, perhaps because they formed optically unresolvable small oligomers (Boyle et al., 2012).

We next tested human-designed self-assembling peptides that were not coiled-coil forming proteins but that had been

shown in solution to form large protein assemblies beyond oligomers, such as polyhedra. These peptides include the I3-01 peptide that forms a 60-subunit, 25-nm-sized, 1.33 MDa protein dodecahedron (Hsia et al., 2016) and other supramolecular assembly forming peptides (Garcia-Seisdedos et al., 2017; Gonen et al., 2015). Interestingly, I3-01 was able to form identifiable puncta of GCaMP6f in neurons, that were modestly brighter than the non-puncta cytosol (the fluorescence intensity ratio between the puncta and nearby non-puncta cytosol, or “degree of clustering” D_C , was about 2; see Table S2 for the D_C of all tested constructs); none of the other designs produced any puncta in neurons ($D_C = 1$). Thus, we hypothesized that perhaps self-assembling peptides could result in meaningful puncta, but they needed to be more scalably assembled beyond the sizes achievable with a single self-assembling peptide: perhaps if a fluorescent reporter was fused to two self-assembling peptides, for example, it could form more scalable assemblies, because each protein might enable multiple bridges to form (Figure 1B).



(legend on next page)

We thus decided to fuse GCaMP6f to a pair of self-assembling peptides—one a coiled-coil forming protein, and one a polyhedron forming protein—to see whether the combination of two peptides could enable the formation of more bright, more macroscopic clusters.

We fused the short, coiled-coil forming, homo-tetramer Hex-Coil-Ala (Grigoryan et al., 2011; 30 amino acids long; four Hex-Coil-Ala will assemble into a 12.8 kDa coiled-coil assembly) to I3-01 fused to GCaMP6f. We named the resulting dual self-assembling motif S1 and the reporter construct (including the immunopeptide Xpress for later antibody staining identification) S1-GCaMP6f (Figure 2A). S1-GCaMP6f offered an extremely high D_C of 10^3 to 10^4 (cf. Figures 2B and 2C; quantitation in Table S3), indicating promise as a protein scaffold-based SiRl construct for spatially multiplexed imaging. Ca^{2+} transients reported by S1-GCaMP6f were indistinguishable from those reported by conventional GCaMP6f (single action potential [AP], Figure 2D; multiple APs, Figures S1A and S1B), with similar transient amplitudes (single AP, Figure 2E; multiple APs, Figure S1C) and signal-to-noise (single AP, Figure 2F; multiple APs, Figure S1D) in neurons, compared at the soma, at sites on proximal neurites (5–25 μm away from the soma), and at sites on distal neurites (50–250 μm away from the soma). The rise time and decay time of reported Ca^{2+} transients elicited by single APs were similar between GCaMP6f and S1-GCaMP6f as well (Figure 2G). The amplitude, rise time, and decay time of S1-GCaMP6f-reported Ca^{2+} transients elicited by single APs had no correlation with the number of puncta, the brightness of puncta, or the size of puncta (Figures S1E–S1P), with one reported Ca^{2+} peak per single AP (Figure S1Q). When elicited by extracellular forskolin stimulation, which drives cAMP production and induces extracellular Ca^{2+} influx and/or intracellular Ca^{2+} release in multiple types of cultured neurons (Gorbunova and Spitzer, 2002; Otsuguro et al., 2005; Zanassi et al., 2001), Ca^{2+} signals reported by S1-GCaMP6f appeared similar to those reported by GCaMP6f in amplitude, signal-to-noise ratio, and number of peaks observed (Figures S1R–S1V). Thus, S1 clus-

tering of GCaMP6f into puncta did not alter GCaMP6f functionality. S1-GCaMP6f puncta were ~ 0.5 – $2 \mu\text{m}$ in diameter (Figure 2H, left; consistent across gene dosages, Figure S1W), with median distance to the nearest punctum of $\sim 5 \mu\text{m}$ (Figure 2H, middle; consistent across gene dosages, Figure S1X), and remained almost completely spatially stationary over 1 h periods, with mean squared displacement of $1.8 \mu\text{m}^2$ per hour, or an estimated diffusion coefficient of $0.006 \mu\text{m}^2$ per minute (Figure 2H, right) in live neurons. S1-GCaMP6f puncta brightness (Figure S1Y), but not puncta count (Figure S1Z), increased with gene dosage. S1-GCaMP6f expression did not alter the basal or active electrophysiological properties of neurons (Table S3) and S1-GCaMP6f puncta did not colocalize with subcellular organelles in neurons, including mitochondria, endosomes, lysosomes, Golgi apparatus, and endoplasmic reticulum (Figure S2A).

If the design were modular, one could simply adapt an existing fluorescent indicator into a multiplexable form that is compatible with simultaneous use with other similarly adapted reagents. This could in principle enable any desired set of existing fluorescent reporters to become a multiplexable set. To test this, we chose a high-performance cAMP reporter, cAMP_r (Hackley et al., 2018), and a high-performance protein kinase A (PKA) activity reporter, ExRaiAKAR (Mehta et al., 2018), both of which are GFP-based (and thus cannot be used simultaneously with a conventional microscope). We fused cAMP_r and ExRaiAKAR to *de novo* designed homo-oligomer peptides as well as polyhedron-forming peptides, following the design of S1 as a fusion of Hex-Coil-Ala and I3-01. We paired short coiled-coil forming homooligomers that were previously tested in GCaMP6f fusions with five different peptides that form octahedra or tetrahedra (King et al., 2012, 2014; Lai et al., 2012, 2014, 2016), as well as a group of fiber/foci-forming dihedral homomers (Garcia-Seisdedos et al., 2017). The construct with the largest D_C ($D_C \sim 10^2$; see Table S3 for D_C at soma and neurites) for cAMP_r consisted of 2L8HC4_15, a homo-tetramer (Boyken et al., 2016), 1M3U, the self-assembling subunit of the 1M3U fiber assembly (Garcia-

Figure 2. Design and Characterization of Fluorescent Reporters Clustered by Protein Scaffolds

- (A) Construct design of S1-GCaMP6f. GCaMP6f, GFP-based fluorescent calcium reporter; HexCoil-Ala, a homo-tetramer; Xpress, epitope; I3-01, self-assembling subunit of I3-01 dodecahedron (60-mer); AA, amino acid (see Table S1 for sequences of the motifs; see Table S2 for all tested constructs).
- (B) Representative confocal image of live cultured mouse hippocampal neuron expressing GCaMP6f. Scale bar, 20 μm throughout this figure.
- (C) Representative confocal image of live cultured mouse hippocampal neuron expressing S1-GCaMP6f and mRFP as a cell morphology marker.
- (D) Representative fluorescent signals recorded from the soma, proximal neurites (5–25 μm away from soma throughout this figure), and distal neurites (50–250 μm away from soma throughout this figure) of a cultured mouse hippocampal neuron expressing GCaMP6f versus S1-GCaMP6f in response to an action potential (AP). dF/F_0 , fluorescence change in the GFP channel, from a single punctum (throughout).
- (E) Bar plot of peak fluorescence changes in the GFP channel at the soma, proximal neurites, and distal neurites of cultured mouse hippocampal neurons expressing GCaMP6f or S1-GCaMP6f in response to a single action potential. Bar plots of medians with interquartile ranges are used throughout this paper, with individual values plotted as dots. n.s., not significant; two-way analysis of variance followed by post hoc Bonferroni corrected multiple comparisons test; see Table S4 for full statistics for Figure 2.
- (F) Signal-to-noise ratio for the data of (E). Noise is defined as standard deviation of pre-stimulus baseline throughout this paper.
- (G) Half rise time and half decay time of reported calcium transients at the soma, for the neurons of (E).
- (H) Violin plots of puncta size (left), distance to the nearest punctum (middle), and diffusion constant over 1 h (right), for puncta of S1-GCaMP6f in neurons. Red line, median; black line, interquartile ranges, throughout.
- (I–P) As in (A)–(H) but for S2-cAMP_r. cAMP_r, GFP-based fluorescent cAMP reporter; 1M3U, self-assembling subunit of 1M3U filament assembly; HA, influenza hemagglutinin epitope; 2L8HC4_15, a homo-tetramer; AA, amino acid. Stimulation was with 5 μM forskolin. n.s., not significant; * $p < 0.05$.
- (Q–X) As in (A)–(H) but for S3-ExRaiAKAR. ExRaiAKAR, GFP-based fluorescent PKA activity reporter; 3VDX, self-assembling subunit of 3VDX tetrahedron (12-mer); V5, simian virus 5-derived epitope; 5L6HC3_1, a homo-trimer; AA, amino acid. Stimulation was with 5 μM forskolin. dR/R_0 , changes of fluorescence ratio between 488 nm excitation and 405 nm excitation when imaged in the GFP emission channel. n.s., not significant.
- See also Figures S1, S2, S3, and S4.

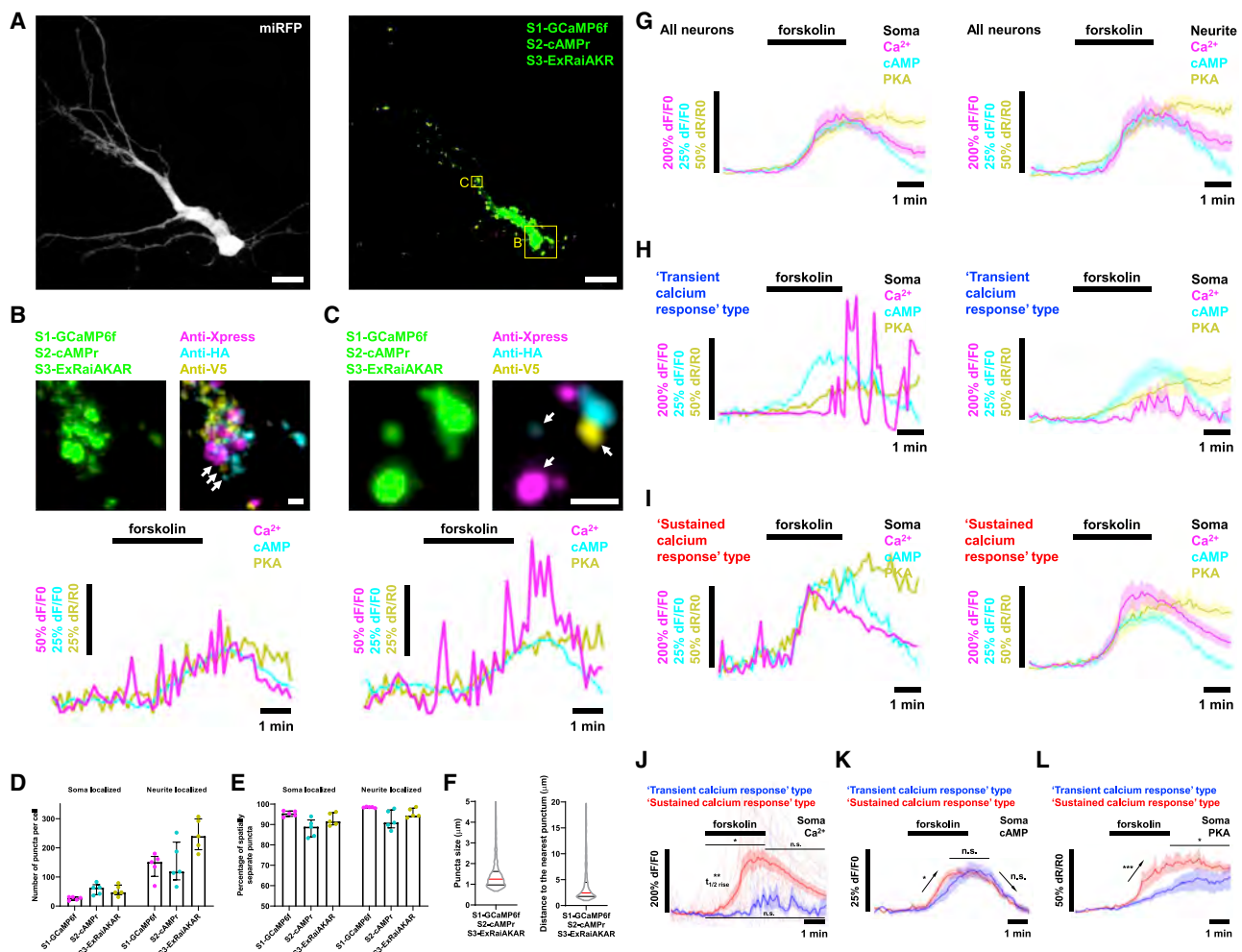


Figure 3. Spatially Multiplexed Imaging of Reporters for Calcium, cAMP, and PKA in Single Cultured Neurons

(A) Maximum intensity projection (MIP) confocal images of a representative live cultured mouse hippocampal neuron co-expressing S1-GCaMP6f, S2-cAMPr, S3-ExRaiAKAR, and miRFP. Left panel, miRFP channel; right panel, GFP channel with high image contrast for better visualization of neurite-localized puncta. Yellow squares, enlarged in (B) and (C). Scale bar, 20 μ m. See Figure S5 for more enlarged views.

(B) Top left, enlarged view of the soma region indicated in (A) with "B," with reduced image contrast for less saturated pixels in this field of view. Top right, MIP confocal image of the same region after fixation and immunostaining against Xpress (magenta), HA (cyan), and V5 (yellow). Bottom, recorded Ca^{2+} (magenta), cAMP (cyan), and PKA (yellow) activities measured from puncta indicated by white arrowheads in the top-right view during live-cell imaging after 3 min of 50 μ M forskolin stimulation. Scale bar, 2 μ m.

(C) As in (B) but for the neurite region indicated in (A) with "C."

(D) Bar plot of the number of soma-localized and neurite-localized puncta per cell identified by immunostaining of neurons co-expressing S1-GCaMP6f, S2-cAMPr, S3-ExRaiAKAR, and miRFP (see Table S4 for full statistics for Figure 3).

(E) Bar plot of the percentage of the soma-localized or neurite-localized puncta of S1-GCaMP6f, S2-cAMPr, or S3-ExRaiAKAR that did not contain the other types of reporters, per cell, for the neurons of (D).

(F) Violin plots of the puncta size (left) and distance to the nearest punctum (right) of all puncta in the GFP channel in live neurons co-expressing S1-GCaMP6f, S2-cAMPr, S3-ExRaiAKAR, and miRFP.

(G) Averaged fluorescent signals of Ca^{2+} (magenta), cAMP (cyan), and PKA activities (yellow) at the soma (left) and on a proximal neurite (right; puncta 20–60 μ m away from soma) under 50 μ M forskolin stimulation for 3 min. Throughout this paper: colored centerlines, mean; colored, shaded boundaries, standard error of mean.

(H) Somatic Ca^{2+} , cAMP, and PKA activities from a representative neuron with a transient calcium response at the soma (left), and averaged somatic Ca^{2+} , cAMP, and PKA activities from all neurons with transient calcium responses at the soma.

(I) As in (H) but for neurons with sustained calcium responses at the soma.

(J) Averaged somatic Ca^{2+} activity from neurons with transient calcium responses at the soma and from neurons with sustained calcium responses at the soma. Thin and light colored lines, somatic Ca^{2+} activities from individual neurons. n.s., not significant; * $p < 0.05$; ** $p < 0.01$; Wilcoxon rank-sum tests for peak responses over indicated time windows (horizontal lines) and times to half rise ($t_{1/2}$ rise).

(legend continued on next page)

Seisedos et al., 2017), and HA, an epitope tag, and we called it S2-cAMPPr (Figure 2I). S2-cAMPPr produced bright puncta in the soma and neurites of cultured mouse hippocampal neurons (Figures 2J and 2K), and reported cAMP amplitudes as accurately as conventional cAMPPr (Figures 2L and 2M), with similar signal-to-noise ratio (Figure 2N) and kinetics (Figure 2O) as conventional cAMPPr, when stimulated with forskolin in the culture media. S2-cAMPPr puncta were comparable in diameter (Figure 2P, left), punctum-punctum distance (Figure 2P, middle), and spatial stationarity (Figure 2P, right) to those of S1-GCaMP6f. Finally, as with S1-GCaMP6f, S2-cAMPPr did not alter the electrophysiological properties of neurons (Table S3) nor colocalize with subcellular organelles within neurons (Figure S2B).

To further explore the generality of our design strategy, we thoroughly characterized a second successful punctum-forming cAMPPr reporter, which we named S2a-cAMPPr, using a different set of scaffolding peptides (Figure S3). To explore how universal the SiRI concept might be, we also generated a prototype RNA-scaffolded version of SiRI, in which fluorescent reporters were fused to RNA binding proteins, which then would cluster reporters onto expressed RNA strands containing repeats targeted by the RNA binding proteins (Figure S4; HeLa cells); however, this strategy did not result in clusters in neurons, and so we did not pursue it further.

We found that dual peptide-scaffolded SiRIs indeed were modularly assemblable: almost all the polyhedron/coil hybrid scaffolds that we tested provided $D_C > 100$, and a given scaffold could be used successfully with different sensors, showing the generality of the strategy (Table S2). The construct with the largest D_C ($D_C \sim 10^2$; see Table S3 for D_C at soma and neurites) for ExRaiAKAR consisted of 5L6HC3_1, a homo-trimer (Boyken et al., 2016), 3VDX, a self-assembling subunit of a tetrahedron (Lai et al., 2016), and V5, an epitope tag, and we called it S3-ExRaiAKAR (Figure 2Q). S3-ExRaiAKAR produced bright puncta in the soma and neurites in cultured mouse hippocampal neurons (Figures 2R and 2S) and reported PKA activity as accurately (Figures 2T and 2U) and with as good signal-to-noise ratio (Figure 2V) and kinetics (Figure 2W) as conventional ExRaiAKAR, when stimulated with forskolin in the culture media. As with S1- and S2- clustered puncta, S3-ExRaiAKAR puncta were small (Figure 2X, left), closely packed (Figure 2X, middle), and stationary (Figure 2X, right) and did not alter the electrophysiological properties of neurons (Table S3) nor colocalize with subcellular organelles (Figure S2C).

Simultaneous Spatially Multiplexed Imaging Reveals Relationships between Multiple Biological Signals in Neurons

We next sought to see whether SiRIs for Ca^{2+} , cAMP, and PKA could be used simultaneously to map out relationships between signals within this complex network in response to a biologically meaningful stimulus. We co-expressed S1-GCaMP6f, S2-

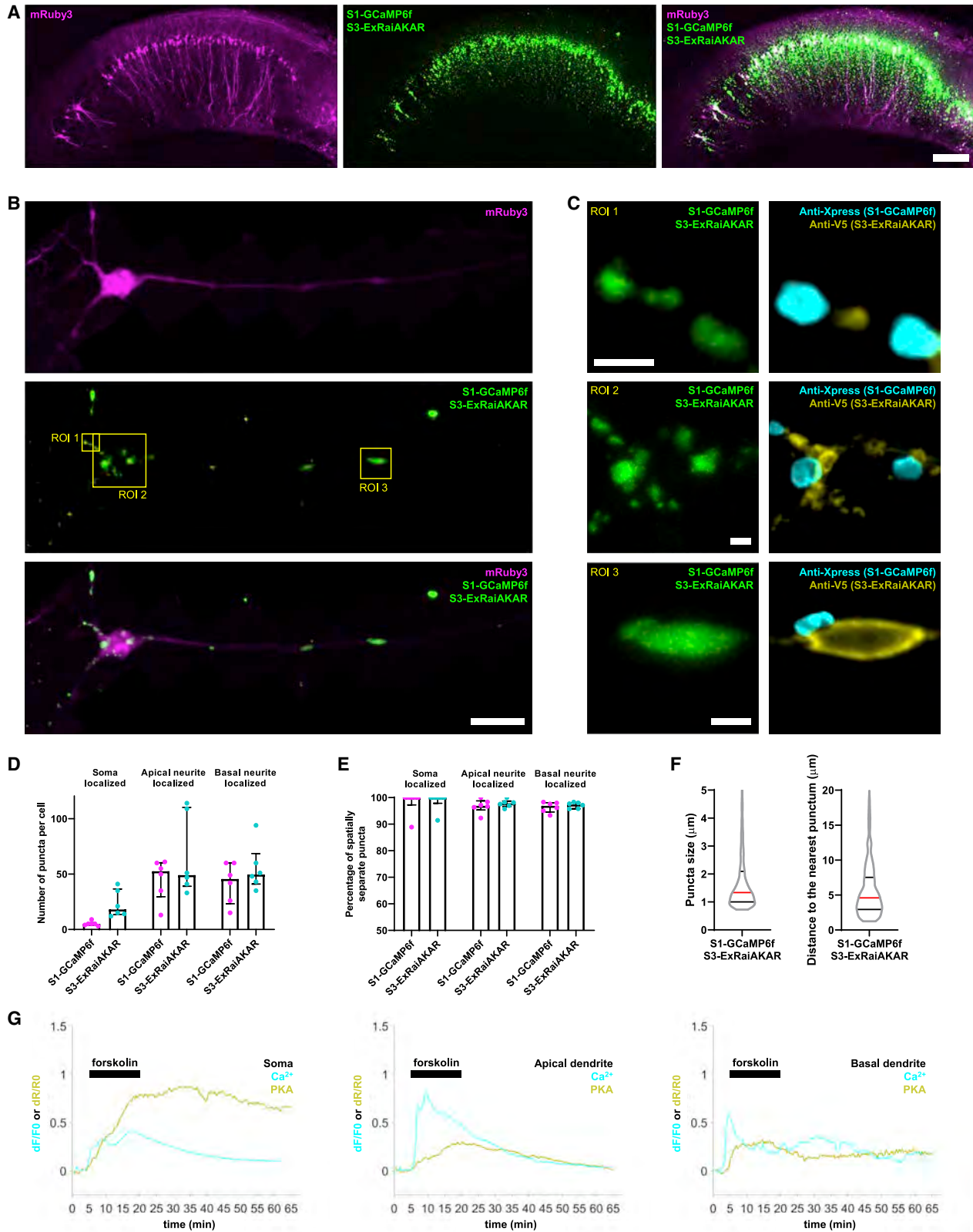
cAMPPr, S3-ExRaiAKAR, and the cell morphology marker miRFP in cultured mouse hippocampal neurons (Figures 3A–3C). We accordingly performed volumetric live imaging of neurons in the GFP channel to record simultaneous Ca^{2+} , cAMP, and PKA responses to forskolin stimulation, a pharmacological driver of cAMP production that has been used on multiple kinds of cultured neurons and has been shown to engage cAMP-dependent modulation of Ca^{2+} concentration and PKA activity (Gorbunova and Spitzer, 2002; Otsuguro et al., 2005; Zanassi et al., 2001); these experiments were able to reveal some of the ways that Ca^{2+} dynamics and cAMP dynamics relate (e.g., through coupled oscillations). While it is possible to simultaneously express three fluorescent reporters of Ca^{2+} , cAMP, and PKA that are based on fluorescent proteins of different colors (Mehta et al., 2018), imaging of these reporters requires either filter switching and the reuse of the camera for serial imaging of the three channels, which can slow down the frame rate of imaging, or multiple light paths and cameras, increasing instrument complexity and expense. We here explored whether we could go at a recording rate of 5 s per volume, using just one filter set. After performing live imaging, we fixed the neurons and performed three-color immunostaining against the epitopes associated with each scaffold (Figures 2A, 2I, and 2Q), so that the reporter identity associated with each puncta could be derived (Figures 3B and 3C, top; see Figures S5A–S5F for additional fields of view of the neuron), and time courses of each signal could be associated with each punctum (Figures 3B and 3C, bottom; see Figures S5A–S5F for additional fields of view of the neuron). Each reporter was found in tens of distinct locations within cell bodies, and hundreds of distinct locations along neurites of neurons (Figure 3D). The vast majority ($\sim 90\%$) of the puncta were unique to one reporter, that is not colocalized with reporters of other kinds, indicating orthogonality of the clustering reagents and spatial separation between the reporters (Figure 3E; puncta with multi-reporter overlap were not analyzed in the dynamics studies that follow). Puncta were comparable in size (Figure 3F, left) and punctum-punctum distance (Figure 3F, right) when expressed together, as when expressed alone (Figure 2). With forskolin provided in this globally administered fashion, we found that Ca^{2+} responses were highly correlated across different sites within the soma, across different points within single neurites, and across neurites within a given neuron, although comparing Ca^{2+} at a point in the soma versus a point in a neurite showed a somewhat lower correlation (Figure S5G); cAMP (Figure S5H) and PKA activity (Figure S5I) were also highly correlated across different points within a neuron. These three SiRIs could be used simultaneously in HeLa cells as well (Figures S5J–S5L).

We imaged Ca^{2+} , cAMP, and PKA activity in neurons before, during, and after 3 min of forskolin stimulation. When averaged across all neurons, we observed increases in Ca^{2+} and cAMP levels that decayed after removal of forskolin, and PKA activity

(K) Averaged somatic cAMP activity for the neurons of (J). n.s., not significant; * $p < 0.05$; Wilcoxon rank-sum tests for rise slopes (arrow near the rise phase), decay slopes (arrow near the decay phase), and peak responses (horizontal line near the peak response).

(L) Averaged somatic PKA activity for the neurons of (J). * $p < 0.05$; *** $p < 0.001$; Wilcoxon rank-sum tests for rise slopes (arrow near the rise phase) and peak responses (horizontal line near the peak response).

See also Figures S5 and S6.



(legend on next page)

that persisted after removal of forskolin, at both somatic (Figure 3G, left) and neurite locations (Figure 3G, right). Thus, SiRIs can be used to perform simultaneous imaging of multiple signals within single living cells, revealing their response to a stimulus. We noticed that some cultured hippocampal neurons exhibited transient, often oscillatory, somatic Ca^{2+} responses, with each increase in Ca^{2+} concentration lasting 1 min or less (Figure 3H), whereas others exhibited sustained Ca^{2+} responses at the soma, with at least one Ca^{2+} elevation event lasting for ~2–6 min (Figure 3I). Neurons with sustained Ca^{2+} responses had significantly higher peak Ca^{2+} increases during forskolin stimulation than neurons with transient Ca^{2+} responses (Figure 3J). However, the peak Ca^{2+} amplitudes measured after forskolin removal, and the peak Ca^{2+} amplitudes when considered over the entire time course of the experiment, were similar across the two groups (Figure 3J). We thus hypothesized that neurons with transient Ca^{2+} responses were also delayed in their Ca^{2+} responses, relative to the neurons with sustained Ca^{2+} responses. Indeed, transient Ca^{2+} response neurons had latencies ~1.2 min longer (~58% longer) than sustained Ca^{2+} response neurons (Figure 3J).

Given that Ca^{2+} and cAMP signals can influence each other bidirectionally, as discussed earlier, we next asked whether such variations in Ca^{2+} dynamics were associated with any variations in cAMP dynamics. Neurons that exhibited sustained, and shorter-latency, Ca^{2+} responses at the soma had faster rises in cAMP at the soma than did those with transient, and longer-latency, Ca^{2+} responses (Figure 3K). This could have resulted because the sustained, shorter-latency Ca^{2+} responses fed back upon the forskolin-driven cAMP responses to accelerate them, or because the faster initial cAMP response to forskolin fed forward to result in faster Ca^{2+} responses. We next analyzed whether these variations in cAMP and Ca^{2+} dynamics were associated with variations in PKA signaling, which as a sustained activity that persists beyond the duration of forskolin stimulation (Figure 3G) may represent an output state of this signaling network in the context of this experiment. Indeed, PKA signals at the soma not only rose faster in neurons with sustained, short-latency Ca^{2+} responses and fast cAMP increases, than in neurons with transient, longer-latency Ca^{2+} responses and slower cAMP increases but also achieved higher activity levels

at the end of the experiment (Figure 3L). Similar relationships were apparent when Ca^{2+} , cAMP, and PKA activities were analyzed at sites along neurites (Figure S6).

Spatially Multiplexed Imaging of Ca^{2+} and PKA in Mouse Hippocampal Brain Slice

We next explored whether we could measure signals within the Ca^{2+} /cAMP/PKA signal transduction network in an intact biological preparation; many studies of acute brain slices have focused on how feedback as well as feedforward parts of the Ca^{2+} /cAMP/PKA signal transduction network work together to govern the efficacy of signaling (Chalifoux and Carter, 2010; Qian et al., 2017; Skeberdis et al., 2006; Wong et al., 1999). We expressed the S1-GCaMP6f and S3-ExRaiAKAR SiRIs in pyramidal neurons in mouse hippocampal area CA1 (Figure 4A), with the goal of studying the relationship between these signals over timescales of ~1 h (i.e., the time course of many long-term potentiation (LTP) experiments); unfortunately, cAMP_{Pr} photobleached too fast (i.e., down to 60% in 8 min) to support hour-long imaging, and so S2-cAMP_{Pr} was omitted in this experiment. S1-GCaMP6f and S3-ExRaiAKAR SiRIs formed puncta that were distributed in somata as well as in neurites of hippocampal CA1 pyramidal neurons (Figure 4B). SiRI expression in the hippocampus and cortex did not alter markers of cellular and synaptic health, including the neuronal nucleus marker NeuN, the apoptotic marker cleaved caspase-3, the astrocyte marker GFAP, the microglial marker Iba1, the synaptic marker Synaptophysin, and the DNA damage marker γ H2AX (Figures S2E–S2K). Post-fixation immunostaining enabled us to identify the reporter within each punctum (Figure 4C, close-up views; Figure S7A, full-neuron views), with puncta plentiful (Figure 4D) and with >90% of the S1-GCaMP6f or S3-ExRaiAKAR puncta not colocalizing with reporters of the other kind (Figure 4E). SiRI puncta in brain slices were comparable in size to those in neuron culture (Figure 4F, left), as were punctum-punctum distances (Figure 4F, right).

We performed volumetric imaging of SiRIs in hippocampal CA1 pyramidal neurons in acute brain slices before, during, and after a 15-min administration of 50 μM forskolin (which, although not our focus, was sufficient to induce LTP; Figure S7B), identifying reporter types by post hoc immunostaining (Figure 4G, representative responses from a single neuron;

Figure 4. Spatially Multiplexed Imaging of Ca^{2+} and PKA Activities in Brain Slice

- (A) Representative confocal images of hippocampus CA1 region in sagittal brain slices from mice co-expressing S1-GCaMP6f, S3-ExRaiAKAR, and mRuby3-6xFLAG. Scale bar, 200 μm .
- (B) Maximum intensity projection (MIP) confocal images of a representative live CA1 pyramidal neuron from mice co-expressing S1-GCaMP6f, S3-ExRaiAKAR, and mRuby3-6xFLAG. Yellow squares, boundaries of regions of interest (ROIs) shown in enlarged views in (C). Scale bar, 20 μm .
- (C) MIP confocal images of the ROIs defined in (B) before (left; S1-GCaMP6f and S3-ExRaiAKAR in the GFP channel) and after (right; cyan, anti-Xpress; yellow, anti-V5) immunostaining. Scale bars, 2.5 μm .
- (D) Bar plot of the number of soma-localized, apical dendrite-localized, or basal dendrite-localized puncta of S1-GCaMP6f or S3-ExRaiAKAR per cell identified by immunostaining of brain slices from mice co-expressing S1-GCaMP6f, S3-ExRaiAKAR, and mRuby3-6xFLAG; see Table S4 for full statistics for Figure 4.
- (E) Bar plot of the percentage of the soma-localized, apical dendrite-localized, or basal dendrite-localized puncta of S1-GCaMP6f or S3-ExRaiAKAR that did not contain the other type of reporter, per cell, for the neurons of (D).
- (F) Violin plots of punctum size (left) and distance to the nearest punctum (right), for all puncta in the GFP channel in live CA1 pyramidal neurons co-expressing S1-GCaMP6f, S3-ExRaiAKAR, and mRuby3-6xFLAG in acute brain slices.
- (G) Representative fluorescent signals for Ca^{2+} (cyan) and PKA (yellow) activities at the soma (left), at a location on the apical dendrite (middle; sampled at locations 30–100 μm away from soma throughout this figure), and at a location on the basal dendrite (right; sampled at locations 10–40 μm away from soma throughout this figure) of CA1 pyramidal neurons before, during, and after a 15-min-long 50 μM forskolin stimulation.
- See also Figures S2 and S7.

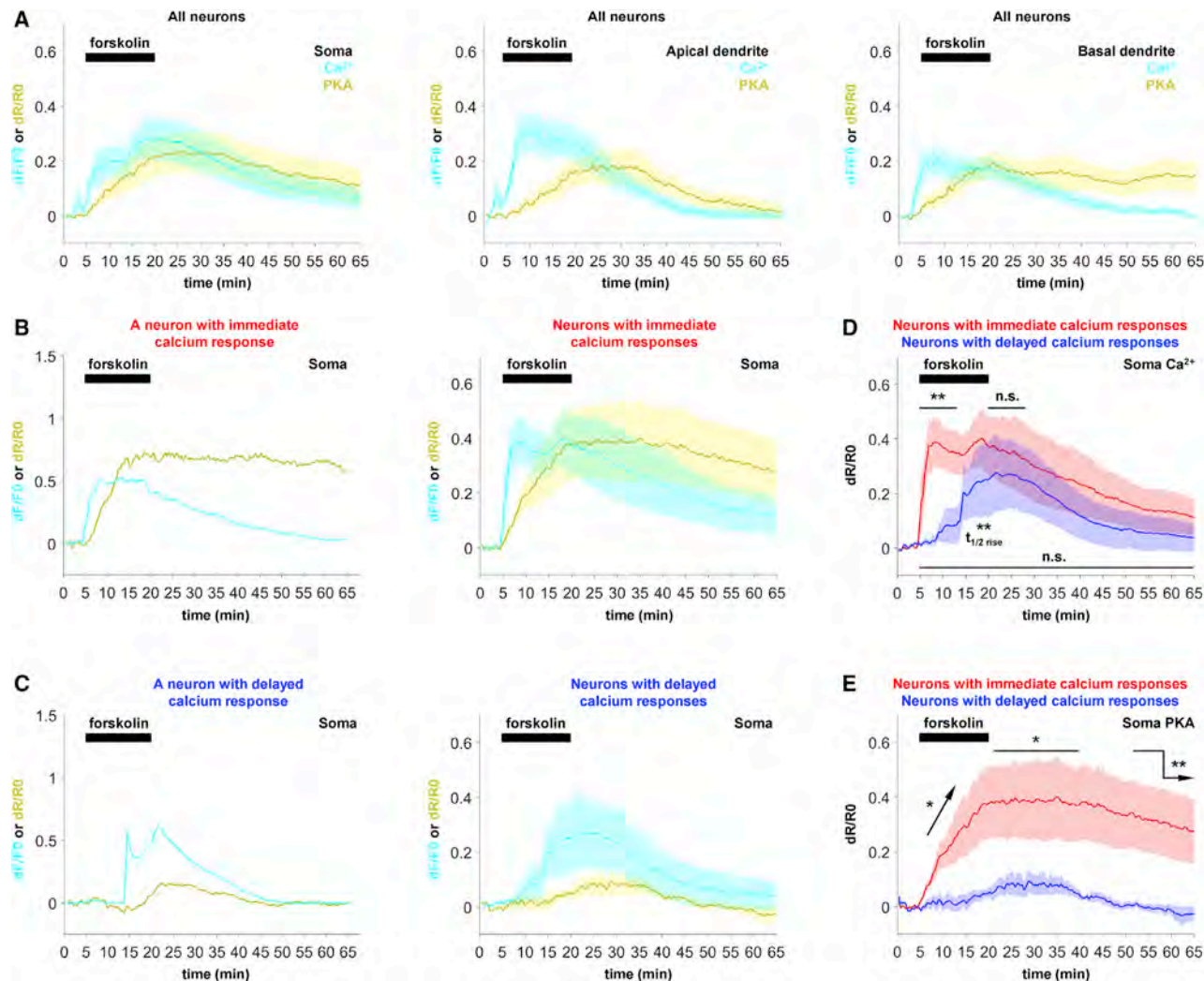


Figure 5. Correlations between Ca^{2+} and PKA Activities in CA1 Pyramidal Neurons in Brain Slice

(A) Averaged fluorescent signals for Ca^{2+} (cyan) and PKA (yellow) activities at the soma (left), at a location on the apical dendrite (middle; sampled at locations 30–100 μm away from soma throughout this figure), and at a location on the basal dendrite (right; sampled at locations 10–40 μm away from soma throughout this figure) of CA1 pyramidal neurons before, during, and after a 15-min-long 50 μM forskolin stimulation.

(B) Somatic Ca^{2+} and PKA activities from a representative neuron where the forskolin treatment induced an immediate somatic calcium response (left) and the averaged soma Ca^{2+} and PKA activities from all neurons with immediate somatic calcium responses.

(C) As in (B) but for neurons with delayed somatic calcium responses.

(D) Averaged somatic Ca^{2+} activity from neurons with immediate somatic calcium responses and from neurons with delayed somatic calcium responses. n.s., not significant; ** $p < 0.01$; Wilcoxon rank-sum tests for peak responses over indicated time windows (horizontal lines) and times to half rise ($t_{1/2 \text{ rise}}$); see Table S4 for full statistics for Figure 5.

(E) Averaged somatic PKA activity from neurons of (D). * $p < 0.05$; ** $p < 0.01$; Wilcoxon rank-sum tests for rise slopes (arrow near the rise phase), peak responses (horizontal line), and durations of PKA activation (arrow on the right hand side of the panel).

See also Figure S7.

Figure 5A, the average response from all recorded neurons). At a population level, neurons exhibited a Ca^{2+} increase during the forskolin administration period, which decayed after forskolin removal, accompanied by a ramp up in PKA activity that was more sustained, similar to the cultured neuron experiments of Figure 3. In contrast to the cultured neuron studies, however, we did not observe prominent Ca^{2+} oscillations within individual cells. However, we noted that some neurons had immediate

Ca^{2+} increases (i.e., within 1 min of the onset of forskolin stimulation, Figure 5B), whereas others had delayed Ca^{2+} responses (i.e., starting 3–15 min after the onset of forskolin stimulation, Figure 5C; one neuron did not have a Ca^{2+} response above baseline at all (>5% dF/F_0) and one neuron had spontaneous Ca^{2+} activity before forskolin stimulation, so these two neurons were not analyzed further) at the cell body, reminiscent of the short-latency versus long-latency responses we observed in cultured

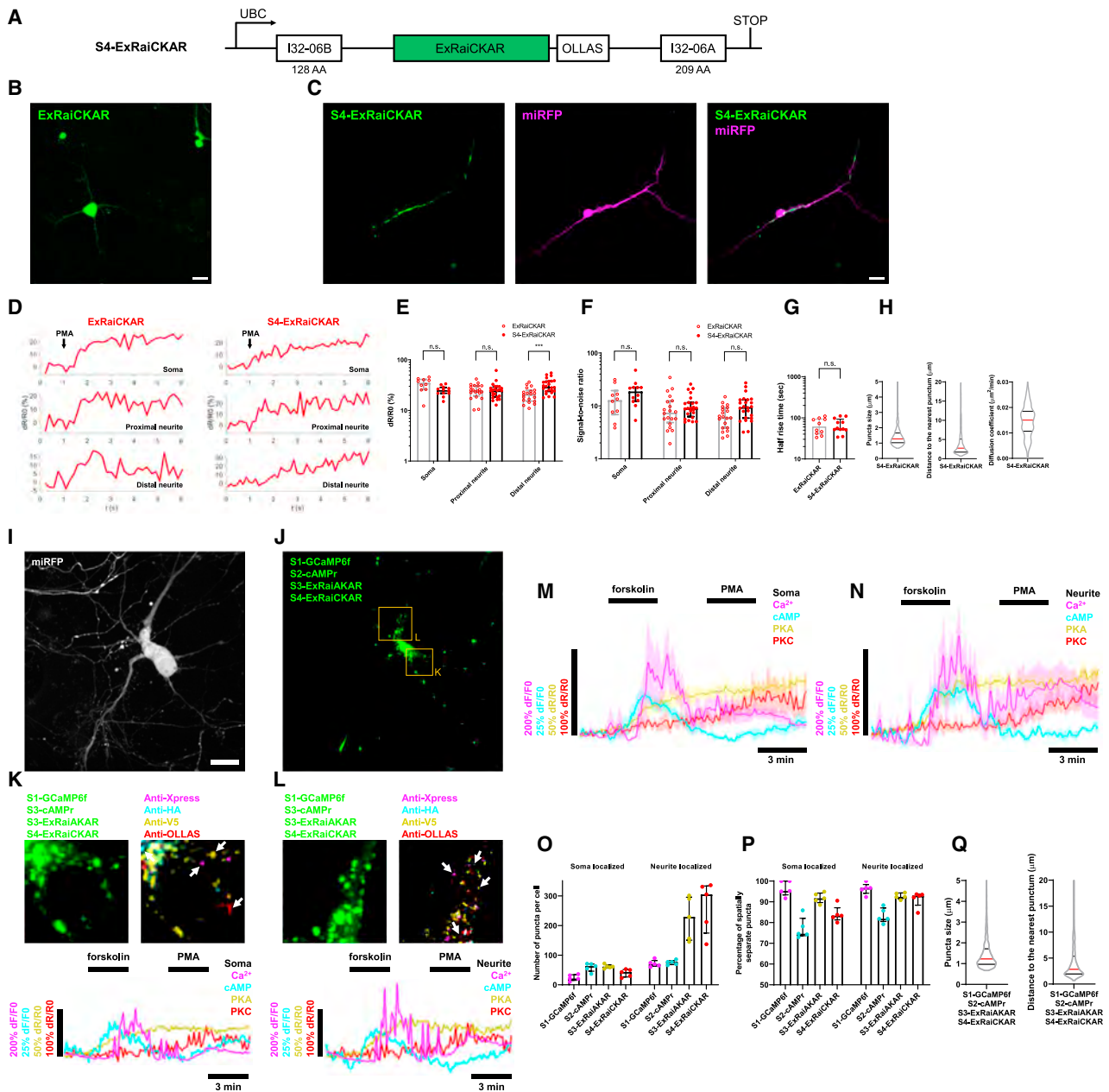


Figure 6. Spatially Multiplexed Imaging of Reporters for Ca^{2+} , cAMP, PKA, and PKC Activities in Cultured Neurons

(A–H) As in Figures 2A–2H but for S4-ExRaiCKAR. ExRaiCKAR, a GFP-based fluorescent PKC activity reporter; I32-06B, self-assembling subunit B of I32-06 two-component icosahedron; OLLAS, *E. coli* OmpF linker and mouse langerin fusion sequence; I32-06A, self-assembling subunit A of I32-06 two-component icosahedron; AA, amino acid. Stimulation was with 100 ng/mL phorbol 12-myristate 13-acetate (PMA) stimulation. n.s., not significant; *** $p < 0.001$; two-way analysis of variance followed by post hoc Bonferroni corrected multiple comparisons test; see Table S4 for full statistics for Figure 6.

(I) A maximum intensity projection (MIP) confocal image in the miRFP channel of a representative live cultured mouse hippocampal neuron co-expressing S1-GCaMP6f, S2-cAMPr, S3-ExRaiAKAR, S4-ExRaiCKAR, and miRFP. Scale bar, 20 μ m.

(J) An MIP confocal image in the GFP channel of the same neuron shown in (I). Orange rectangles, boundaries of the regions to be shown in enlarged views in (K) and (L).

(K) Top left, the enlarged view of the somatic region in (J). Top right, an MIP confocal image of the same region after fixation and two rounds of immunostaining against HA (cyan) and OLLAS (red) in the first round and Xpress (magenta) and V5 (yellow) in the second round. Bottom, recorded fluorescent signals of Ca^{2+} (magenta), cAMP (cyan), PKA (yellow), and PKC (red) activities measured from puncta indicated by white arrowheads in the top-right view during live-cell imaging under two stimulations, 50 μ M forskolin for 3 min, and 100 ng/mL PMA for 3 min.

(L) As in (K) but for the neuritic region in (J).

(legend continued on next page)

neurons. Indeed, the delayed Ca^{2+} response neurons had latencies 12 min longer (880% longer) than did immediate Ca^{2+} response neurons (Figure 5D). Analogous to the cultured-neuron case, neurons with immediate Ca^{2+} responses had significantly higher peak Ca^{2+} increases within the first half of the forskolin stimulation period than did neurons with delayed Ca^{2+} responses (Figure 5D), whereas the peak Ca^{2+} increases within a similar time period after the end of forskolin stimulation, and the peak Ca^{2+} increases over the entire experimental time course, were similar between the two groups (Figure 5D).

We next asked whether these neurons with immediate versus delayed Ca^{2+} signals had different PKA outputs from this signaling network. We found that neurons with immediate Ca^{2+} increases had PKA responses that were faster, and that achieved higher ultimate magnitudes, than those of neurons with delayed Ca^{2+} responses (Figure 5E). Furthermore, neurons that had immediate Ca^{2+} increases had enduring PKA activation, lasting for the entire hour of monitoring, whereas neurons with delayed Ca^{2+} increases had their PKA activity drop to baseline within 30 min (Figure 5E). These results in brain slice parallel the results we obtained in cultured neurons earlier: in both cases, neurons with shorter latency Ca^{2+} responses exhibited faster and larger PKA signals than did neurons with longer latency Ca^{2+} responses.

We then analyzed responses in apical and basal dendrites (identified based on morphology) under forskolin stimulation. However, when we analyzed PKA rise slope, ultimate amplitude, and duration of signaling, there was no clear relationship to the timing of the Ca^{2+} signals (Figures S7C–S7F), either at sites along the apical dendrites (Figures S7C and S7E) or basal dendrites (Figures S7D and S7F), in contrast to the cultured neuron experiments earlier, where dendritic conclusions paralleled somatic conclusions. When we analyzed the correlations between Ca^{2+} signals across different dendritic sites, or between PKA signals across different dendritic sites, we found much lower site-to-site correlations than in the cultured neuron experiments earlier (Figure S7G). Thus, in brain slices, Ca^{2+} -PKA relationships in hippocampal neurons might follow different rules in dendritic compartments than at the cell body.

Spatially Multiplexed Imaging of More than 3 Fluorescent Reporters in Neurons and Combined Spatial and Spectral Multiplexing

We further explored the modularity of SiRI design, generation, and utilization, by seeing whether we could generate, and use, 4 and even 5 SiRIs at once. First, we set out to engineer a clustered variant of ExRaiCKAR, a GFP-based protein kinase C (PKC) activity reporter (Mehta et al., 2018). We wondered

whether we could utilize pairs of two-component polyhedron forming peptides because of their abundance (over a hundred pairs were computationally designed and characterized in Bale et al., 2016 alone), which could potentially open up a new family of designs for SiRI constructs within the domain of dual peptide scaffolding, but of a different subtype. We fused pairs of two-component icosahedron forming peptides (I32-06A + I32-06B, I52_03A + I52_03B, and I53_34A + I53_34B, randomly selected from Bale et al., 2016) to ExRaiCKAR, with one component to the N terminus and the other to the C terminus, together with an epitope tag OLLAS. We found that both I32-06A + I32-06B fused to ExRaiCKAR (which we named S4-ExRaiCKAR; see Figure 6A for the construct design; compare expression in Figures 6B and 6C; see Table S3 for D_C at soma and neurites) and I52_03A + I52_03B fused to ExRaiCKAR produced bright puncta ($D_C \sim 10^2$) in the soma and neurites of cultured mouse hippocampal neurons (S4-ExRaiCKAR had a slightly larger D_C and was thus chosen for further characterization), whereas I53_34A + I53_34B fused ExRaiCKAR did not yield any expression. S4-ExRaiCKAR exhibited responses similar to those of conventional ExRaiCKAR (Figure 6D), with comparable amplitude (Figure 6E), signal-to-noise ratio (Figure 6F), and rise time (Figure 6G), when elicited by phorbol 12-myristate 13-acetate (PMA), a PKC activator. S4-ExRaiCKAR puncta were similar in size (Figure 6H, left) and punctum-punctum distance (Figure 6H, middle) as other SiRIs, with good stationarity in neurons over periods of 1 h (Figure 6H, right). S4-ExRaiCKAR did not alter the electrophysiological properties of neurons (Table S3) nor colocalize with markers of subcellular organelles (Figure S2D).

When we co-expressed S1-GCaMP6f, S2-cAMP_r, S3-ExRaiAKAR, and S4-ExRaiCKAR in neurons, we were able to observe puncta (Figures 6I and 6J) of all 4 kinds, as determined by post-fixation immunostaining (Figures 6K, and 6L, top). To facilitate performing the immunostaining in a multiplexed way, we built upon prior work enabling serial immunostaining facilitated by chemical processing (Asano et al., 2018; Bodenmiller, 2016; Chen et al., 2015; Ku et al., 2016; Lin et al., 2018; Tillberg et al., 2016) (see STAR Methods). To show functionality of all 4 sensors, we challenged neurons with two drugs, 50 μM forskolin for 3 min, followed after a break of 3 min by 100 ng/mL phorbol 12-myristate 13-acetate (PMA), a drug known to drive PKC activation, for 3 min, and observed responses of S1-GCaMP6f, S2-cAMP_r, S3-ExRaiAKAR, and S4-ExRaiCKAR to these interventions (Figures 6K and 6L, bottom, representative traces; Figures 6M and 6N, population data). As expected, forskolin induced cAMP, Ca^{2+} , and PKA activities similar to our previous observations, and PMA induced increases of PKC activity. Expressing 4 reporters at once resulted in many puncta at

(M) Averaged fluorescent signals of Ca^{2+} (magenta), cAMP (cyan), PKA (yellow), and PKC (red) activities at the soma under two stimulations, 50 μM forskolin for 3 min and 100 ng/mL PMA for 3 min.

(N) As in (M) but for neurite signals (from locations 20–60 μm away from the soma).

(O) Bar plot of the number of soma-localized or neurite-localized puncta per cell for S1-GCaMP6f, S2-cAMP_r, S3-ExRaiAKAR, and S4-ExRaiCKAR identified by two rounds of immunostaining in neurons co-expressing S1-GCaMP6f, S2-cAMP_r, S3-ExRaiAKAR, S4-ExRaiCKAR, and miRFP.

(P) Bar plot of the percentage of the soma-localized or neurite-localized puncta of S1-GCaMP6f, S2-cAMP_r, S3-ExRaiAKAR, or S4-ExRaiCKAR that did not contain the other types of reporters, per cell, for the neurons of (O).

(Q) Violin plots of the puncta size (left) and distance to the nearest punctum (right) of all puncta in the GFP channel in live neurons co-expressing S1-GCaMP6f, S2-cAMP_r, S3-ExRaiAKAR, S4-ExRaiCKAR, and miRFP.

See also Figure S2.

the soma and along neurites (Figure 6O), with good lack of colocalization of multiple reporters within individual puncta (Figure 6P; puncta containing multiple reporters were not analyzed for their dynamics). Puncta were comparable in size (Figure 6Q, left) and punctum-punctum distance (Figure 6Q, right) when expressed together, as when expressed alone.

We then went on to combine spatial and spectral multiplexing, by sharing one protein scaffold among multiple reporters that emit different colors. We adapted the S2 scaffold, used above for cAMP_r, for a red fluorescent protein (RFP)-based reporter for extracellular signal-regulated kinase (ERK) activity, RAB-EKARev (Ding et al., 2015; Mehta et al., 2018), resulting in S2-RAB_EKARev (Figure 7A). S2-RAB_EKARev produced bright puncta (Figures 7B and 7C) and exhibited similar transients to those of conventional RAB-EKARev (Figure 7D), with comparable amplitude (Figure 7E), signal-to-noise ratio (Figure 7F), and rise time (Figure 7G), when elicited by (S)-3,5-Dihydroxyphenylglycine (DHPG), an agonist of group I metabotropic glutamate receptors (mGluR1 and mGluR5), which has been shown to drive ERK activity in cultured rat neurons (Mao et al., 2005). When S1-GCaMP6f, S2-cAMP_r, S3-ExRaiAKAR, S4-ExRaiCKAR, and S2-RAB_EKARev were co-expressed in mouse hippocampal neurons, they formed puncta (Figure 7H) that could be identified by post-fixation immunostaining (Figure 7I). S2-cAMP_r and S2-RAB_EKARev co-occupied the same puncta but could be distinguished by their different spectra. When imaged in the GFP and RFP channels after stimulation with 100 μ M DHPG for 3 min, followed by a 3-min break, then 50 μ M forskolin for 3 min, signals reported by all 5 indicators could be identified (Figure 7J; population data in Figure 7K). We note that the combination of spatial and spectral multiplexing can enable the readout of SiRI reporter identity without requiring immunostaining (Figures S7H and S7I).

DISCUSSION

We here report that, by fusing a fluorescent reporter to a pair of bioorthogonal, human-designed, self-assembling peptides, it can be safely, robustly, and with high fidelity, clustered into bright, stationary puncta (with brightness 100–10,000 times brighter than the surrounding background) within living cells, both *in vitro* and *in vivo*. We found that this protein architecture, which we call a SiRI, is very modular—that is, given a desired set of signals to be imaged at once within a single living cell, one can reliably adapt a set of existing fluorescent indicators by fusing each to a different pair of self-assembling peptides, so that each will cluster, stochastically, at a different set of points throughout the cell. These puncta end up micrometers from each other, so that many different signals can be dynamically imaged within a living cell at the same time, even if they all possess the same fluorescence spectrum. Because the fluorescent reporters are highly immobile during hour-long imaging experiments, the fluorescent reporter within each SiRI can be identified by post hoc immunostaining for distinct epitopes fused to each reporter. In short, SiRIs allow the high multiplexing capacity of fixed-cell imaging (e.g., many previous studies have used serial antibody staining to label essentially unlimited numbers of protein targets) to be translated to help the live-cell imaging case, using the spatial dimension as a resource.

SiRIs are easy to design, with a highly modular architecture—most of the SiRIs we designed worked well upon initial validation testing, with minimal trial-and-error refinement required. Of course, one limitation on SiRI use is that they cannot report on extremely close, e.g., nanodomain signals (Tenner et al., 2020); they can only be used to answer scientific questions where micrometer resolution is acceptable. In the future, creating a wide diversity of such scaffolds with different kinds of spacing could allow tradeoffs between the number of signals that can be simultaneously observed, and the spatial sampling that is permitted. For a cell with 10,000 microscope-resolvable spots, for example, one might someday be able to have 100 kinds of reporters distributed sparsely at 100 points each, or 10 reporters distributed more densely at 1,000 points each. Being able to deliver this many different constructs to a single cell, however, may require advances in genetic engineering and gene delivery beyond what is currently possible. Going forward, we may be able to take advantage of the recent rapid development of *de novo*/computationally designed, bio-orthogonal protein motifs (Garcia-Seisdedos et al., 2017; Hsia et al., 2016; Huang et al., 2016; King et al., 2012; Lai et al., 2016) and RNA motifs (Delebecque et al., 2011) to enable new modular clustering motifs.

We examined, in cultured hippocampal neurons and in acute mouse hippocampal brain slices, the coupling between Ca²⁺, cAMP, and PKA signals, three signals of immense importance for a large number of normal biological functions, and that go awry in many pathological contexts. In summary, neurons that had shorter-latency cAMP and Ca²⁺ responses to forskolin exhibited stronger PKA activation than neurons with longer-latency cAMP and Ca²⁺ responses, thus revealing how an output signal like PKA is governed by the properties of the messengers upstream. Importantly, such relationships between the different components of this signal transduction network cannot be derived by observing these signals in separate cells, and then comparing them after averaging.

By reducing the reliance of live-cell multi-signal imaging on spectral multiplexing, SiRIs may avoid concerns related to bleedthrough caused by using multiple, spectrally similar fluorescent reporters within the same cell. Spatial multiplexing may also free up optical channels that could be used for other purposes, such as cellular control. For example, one might use the GFP channel to observe cellular activity readout from multiple GFP-based reporters and then utilize the red channel of the microscope to operate red-light driven optogenetic tools (Chuong et al., 2014; Klapoetke et al., 2014). Thus, we anticipate that the spatial multiplexing concept may open up many other possibilities in biology, beyond what we demonstrate here.

STAR★METHODS

Detailed methods are provided in the online version of this paper and include the following:

- KEY RESOURCES TABLE
- RESOURCE AVAILABILITY
 - Lead Contact
 - Materials Availability
 - Data and Code Availability

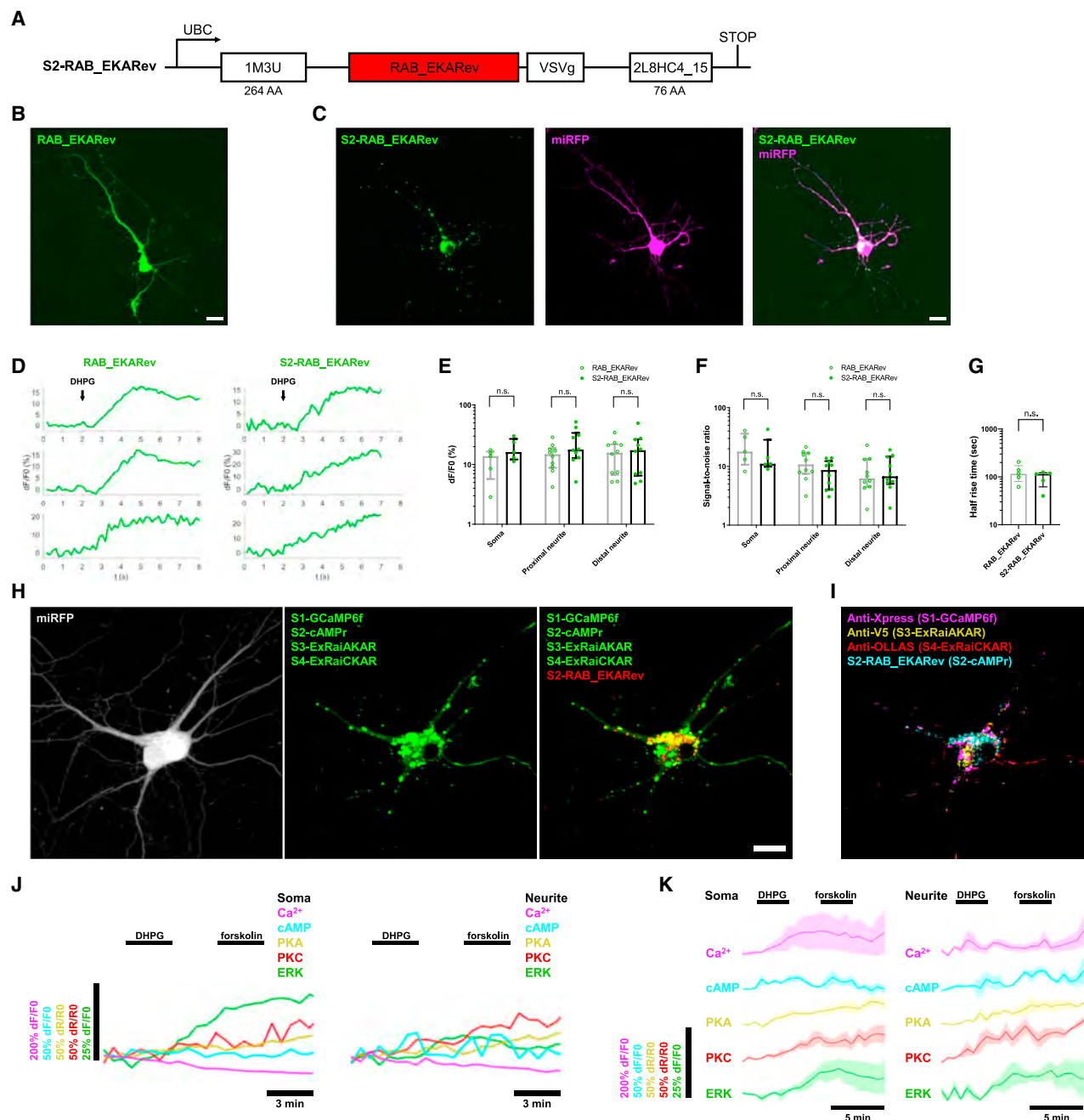


Figure 7. Combined Spatial and Spectral Multiplexing for Simultaneous Imaging of Five Signals within Single Neurons

(A–G) As in Figures 2A–2G but for S2-RAB_EKARev. RAB_EKARev, an RFP-based fluorescent ERK activity reporter; 1M3U, self-assembling subunit of 1M3U assembly; VSVg, vesicular stomatitis virus G protein fragment epitope; 2L8HC4_15, a homo-tetramer; AA, amino acid. Stimulation was with 100 μ M DHPG. n.s., not significant; two-way analysis of variance followed by post hoc Bonferroni corrected multiple comparisons test; see Table S4 for full statistics for Figure 7. (H) Maximum intensity projection (MIP) confocal images in the miRFP channel (left), GFP channel (middle), and GFP and RFP channels merged (right), of a representative live cultured mouse hippocampal neuron co-expressing S1-GCaMP6f, S2-cAMP, S3-ExRaiAKAR, S4-ExRaiCKAR, S2-RAB_EKARev, and miRFP. Scale bar, 20 μ m. (I) A composite image from the registration between the MIP confocal image of the same neuron in (H) in the RFP channel before fixation and the MIP confocal image of the same neuron after fixation and immunostaining against Xpress (magenta), V5 (yellow), and OLLAS (red). (J) Recorded fluorescent signals for Ca²⁺ (magenta), cAMP (cyan), PKA (yellow), PKC (red), and ERK (green) activities at the soma (left) and neurites (right; 30 μ m away from soma) of the same neuron in (H) under two stimulations, 100 μ M DHPG for 3 min and 50 μ M forskolin for 3 min. (K) Averaged fluorescent signals of Ca²⁺ (magenta), cAMP (cyan), PKA (yellow), PKC (red), and ERK (green) activities at the soma (left) and along neurites (right; 20–60 μ m away from soma) under two stimulations, 100 μ M DHPG for 3 min and 50 μ M forskolin for 3 min.

See also Figure S7.

- **EXPERIMENTAL MODEL AND SUBJECT DETAILS**
- **METHOD DETAILS**
 - Molecular Cloning
 - Transfection
 - In Utero Electroporation
 - Fluorescence Microscopy of HeLa cells and Primary Neurons
 - Electrophysiology - Current and Voltage Clamp Recording of Cultured Neurons
 - Electrophysiology and Imaging of Acute Brain Slice
 - Immunostaining of Cultured Cells
 - Multiplexed Immunostaining of Cultured Cells
 - Immunostaining of Brain Slices
 - RNA Fluorescent *In Situ* Hybridization (RNA FISH)
- **QUANTIFICATION AND STATISTICAL ANALYSIS**
 - Image Analysis
 - Statistical analysis:

SUPPLEMENTAL INFORMATION

Supplemental Information can be found online at <https://doi.org/10.1016/j.cell.2020.10.035>.

ACKNOWLEDGMENTS

We thank Daniel Goodwin for help with data analysis and Guangyu Xu and Jian-Ping Zhao for useful discussion. C.L. acknowledges the Friends of the McGovern Institute Graduate Fellowship and the J. Douglas Tan Postdoctoral Fellowship. S.L.J. acknowledges the MIT K. Lisa Yang and Hock E. Tan Center for Molecular Therapeutics in Neuroscience Fellowship and the MIT Media Lab. E.S.B. was supported by Lisa Yang, John Doerr, the Open Philanthropy Project, the HHMI-Simons Faculty Scholars Program and HHMI Investigatorship, Human Frontier Science Program RGP0015/2016, U.S. Army Research Laboratory, and the U.S. Army Research Office under contract/grant number W911NF1510548, the MIT Media Lab, the Picower Institute Innovation Fund, NIH R01MH122971, NIH RF1NS113287, NIH 1R24MH106075, NIH 1R01NS102727, NIH R44EB021054, NIH 1R01DA045549, NIH 1R01MH114031, NIH 2R01DA029639, NIH 1R01EB024261, NIH Director's Pioneer Award 1DP1NS087724, NIH 1R01GM104948, and NSF CBET 1344219.

AUTHOR CONTRIBUTIONS

C.L., S.L.J., and E.S.B. made high-level designs and plans, interpreted the data, and wrote the paper. C.L., S.L.J., and E.S.B. developed the protein scaffold and RNA-scaffold-based molecular strategies together with W.M.P., O.A.S., K.P.A., and A.E.K. C.L. designed the constructs for screening, and C.L. and S.L.J. performed screening and live-cell imaging experiments. C.L. and D.P. performed imaging and electrophysiology experiments on acute mouse brain slices with the help from K.D.P., B.A., S.A.B., and M.F.B. C.L., S.L.J., P.A.V., A.T.W., Y.L., C.-C. Yu, and R.W. performed immunostaining and RNA FISH experiments. C.L., S.L.J., O.T.C., and C.-C. Yao performed data analysis and statistical analysis. E.S.B. oversaw all aspects of the project.

DECLARATION OF INTERESTS

C.L., S.L.J., and E.S.B. declare they applied for a US patent based on the work presented in this paper.

Received: June 15, 2020

Revised: October 5, 2020

Accepted: October 21, 2020

Published: November 23, 2020

REFERENCES

- Abrams, T.W., Karl, K.A., and Kandel, E.R. (1991). Biochemical studies of stimulus convergence during classical conditioning in Aplysia: dual regulation of adenylate cyclase by Ca²⁺/calmodulin and transmitter. *J. Neurosci.* *11*, 2655–2665.
- Asano, S.M., Gao, R., Wassie, A.T., Tillberg, P.W., Chen, F., and Boyden, E.S. (2018). Expansion Microscopy: Protocols for Imaging Proteins and RNA in Cells and Tissues. *Curr. Protoc. Cell Biol.* *80*, e56.
- Averaimo, S., and Nicol, X. (2014). Intermingled cAMP, cGMP and calcium spatiotemporal dynamics in developing neuronal circuits. *Front. Cell. Neurosci.* *8*, 376.
- Bale, J.B., Gonen, S., Liu, Y., Sheffler, W., Ellis, D., Thomas, C., Cascio, D., Yeates, T.O., Gonen, T., King, N.P., et al. (2016). Accurate design of megadalton-scale two-component icosahedral protein complexes. *Science* *353*, 389–394.
- Belousov, V.V., Fradkov, A.F., Lukyanov, K.A., Staroverov, D.B., Shakhbazov, K.S., Terskikh, A.V., and Lukyanov, S. (2006). Genetically encoded fluorescent indicator for intracellular hydrogen peroxide. *Nat. Methods* *3*, 281–286.
- Berg, J., Hung, Y.P., and Yellen, G. (2009). A genetically encoded fluorescent reporter of ATP:ADP ratio. *Nat. Methods* *6*, 161–166.
- Bhullar, K.S., Lagarón, N.O., McGowan, E.M., Parmar, I., Jha, A., Hubbard, B.P., and Rupasinghe, H.P.V. (2018). Kinase-targeted cancer therapies: progress, challenges and future directions. *Mol. Cancer* *17*, 48.
- Bito, H., Deisseroth, K., and Tsien, R.W. (1996). CREB phosphorylation and dephosphorylation: a Ca²⁺- and stimulus duration-dependent switch for hippocampal gene expression. *Cell* *87*, 1203–1214.
- Bodenmiller, B. (2016). Multiplexed Epitope-Based Tissue Imaging for Discovery and Healthcare Applications. *Cell Syst.* *2*, 225–238.
- Borodinsky, L.N., and Spitzer, N.C. (2006). Second messenger pas de deux: the coordinated dance between calcium and cAMP. *Sci. STKE* *2006*, pe22, pe22.
- Boyken, S.E., Chen, Z., Groves, B., Langan, R.A., Oberdorfer, G., Ford, A., Gilmore, J.M., Xu, C., DiMaio, F., Pereira, J.H., et al. (2016). De novo design of protein homo-oligomers with modular hydrogen-bond network-mediated specificity. *Science* *352*, 680–687.
- Boyle, A.L., Bromley, E.H.C., Bartlett, G.J., Sessions, R.B., Sharp, T.H., Williams, C.L., Curmi, P.M.G., Forde, N.R., Linke, H., and Woolfson, D.N. (2012). Squaring the circle in peptide assembly: from fibers to discrete nanostructures by de novo design. *J. Am. Chem. Soc.* *134*, 15457–15467.
- Bruce, J.I.E., Straub, S.V., and Yule, D.I. (2003). Crosstalk between cAMP and Ca²⁺ signaling in non-excitable cells. *Cell Calcium* *34*, 431–444.
- Chalifoux, J.R., and Carter, A.G. (2010). GABAB receptors modulate NMDA receptor calcium signals in dendritic spines. *Neuron* *66*, 101–113.
- Chen, T.-W., Wardill, T.J., Sun, Y., Pulver, S.R., Renninger, S.L., Baohan, A., Schreiter, E.R., Kerr, R.A., Orger, M.B., Jayaraman, V., et al. (2013). Ultrasensitive fluorescent proteins for imaging neuronal activity. *Nature* *499*, 295–300.
- Chen, F., Tillberg, P.W., and Boyden, E.S. (2015). Expansion microscopy. *Science* *347*, 543–548.
- Chen, Z., Boyken, S.E., Jia, M., Busch, F., Flores-Solis, D., Bick, M.J., Lu, P., VanAernum, Z.L., Sahasrabudhe, A., Langan, R.A., et al. (2019). Programmable design of orthogonal protein heterodimers. *Nature* *565*, 106–111.
- Cho-Chung, Y.S. (1990). Role of cyclic AMP receptor proteins in growth, differentiation, and suppression of malignancy: new approaches to therapy. *Cancer Res.* *50*, 7093–7100.
- Chuong, A.S., Miri, M.L., Busskamp, V., Matthews, G.A.C., Acker, L.C., Sørensen, A.T., Young, A., Klapoetke, N.C., Henninger, M.A., Kodandaramaiah, S.B., et al. (2014). Noninvasive optical inhibition with a red-shifted microbial rhodopsin. *Nat. Neurosci.* *17*, 1123–1129.
- Cooper, D.M.F., Mons, N., and Karpen, J.W. (1995). Adenylyl cyclases and the interaction between calcium and cAMP signalling. *Nature* *374*, 421–424.

- Delebecque, C.J., Lindner, A.B., Silver, P.A., and Aldaye, F.A. (2011). Organization of Intracellular Reactions with Rationally Designed RNA Assemblies. *Science* *333*, 470–474.
- Depry, C., Allen, M.D., and Zhang, J. (2011). Visualization of PKA activity in plasma membrane microdomains. *Mol. Biosyst.* *7*, 52–58.
- Ding, Y., Li, J., Enterina, J.R., Shen, Y., Zhang, I., Tewson, P.H., Mo, G.C.H., Zhang, J., Quinn, A.M., Hughes, T.E., et al. (2015). Ratiometric biosensors based on dimerization-dependent fluorescent protein exchange. *Nat. Methods* *12*, 195–198.
- DiPilato, L.M., and Zhang, J. (2009). The role of membrane microdomains in shaping beta2-adrenergic receptor-mediated cAMP dynamics. *Mol. Biosyst.* *5*, 832–837.
- Ferguson, G.D., and Storm, D.R. (2004). Why calcium-stimulated adenylyl cyclases? *Physiology (Bethesda)* *19*, 271–276.
- Fletcher, J.M., Boyle, A.L., Bruning, M., Bartlett, G.J., Vincent, T.L., Zaccai, N.R., Armstrong, C.T., Bromley, E.H.C., Booth, P.J., Brady, R.L., et al. (2012). A basis set of de novo coiled-coil peptide oligomers for rational protein design and synthetic biology. *ACS Synth. Biol.* *1*, 240–250.
- Frey, U., Huang, Y.Y., and Kandel, E.R. (1993). Effects of cAMP simulate a late stage of LTP in hippocampal CA1 neurons. *Science* *260*, 1661–1664.
- Garcia-Seisdedos, H., Empereur-Mot, C., Elad, N., and Levy, E.D. (2017). Proteins evolve on the edge of supramolecular self-assembly. *Nature* *548*, 244–247.
- Giese, K.P., and Mizuno, K. (2013). The roles of protein kinases in learning and memory. *Learn. Mem.* *20*, 540–552.
- Golding, I., and Cox, E.C. (2004). RNA dynamics in live *Escherichia coli* cells. *Proc. Natl. Acad. Sci. USA* *101*, 11310–11315.
- Gonen, S., DiMaio, F., Gonen, T., and Baker, D. (2015). Design of ordered two-dimensional arrays mediated by noncovalent protein-protein interfaces. *Science* *348*, 1365–1368.
- Gorbunova, Y.V., and Spitzer, N.C. (2002). Dynamic interactions of cyclic AMP transients and spontaneous Ca(2+) spikes. *Nature* *418*, 93–96.
- Gradišar, H., Božič, S., Doles, T., Vengust, D., Hafner-Bratkovič, I., Mertelj, A., Webb, B., Šali, A., Klavžar, S., and Jerala, R. (2013). Design of a single-chain polypeptide tetrahedron assembled from coiled-coil segments. *Nat. Chem. Biol.* *9*, 362–366.
- Grigoryan, G., Kim, Y.H., Acharya, R., Axelrod, K., Jain, R.M., Willis, L., Drndic, M., Kikkawa, J.M., and DeGrado, W.F. (2011). Computational design of virus-like protein assemblies on carbon nanotube surfaces. *Science* *332*, 1071–1076.
- Hackley, C.R., Mazzoni, E.O., and Blau, J. (2018). cAMP: A single-wavelength fluorescent sensor for cyclic AMP. *Sci. Signal.* *11*, eaah3738.
- Hardingham, G.E., Arnold, F.J.L., and Bading, H. (2001). Nuclear calcium signaling controls CREB-mediated gene expression triggered by synaptic activity. *Nat. Neurosci.* *4*, 261–267.
- Howe, A.K. (2011). Cross-talk between calcium and protein kinase A in the regulation of cell migration. *Curr. Opin. Cell Biol.* *23*, 554–561.
- Hsia, Y., Bale, J.B., Gonen, S., Shi, D., Sheffler, W., Fong, K.K., Nattermann, U., Xu, C., Huang, P.-S., Ravichandran, R., et al. (2016). Corrigendum: Design of a hyperstable 60-subunit protein icosahedron. *Nature* *540*, 150.
- Huang, Y.-Y., and Kandel, E.R. (1994). Recruitment of Long-lasting and Protein Kinase A-dependent Long-term Potentiation in the CA1 Region of Hippocampus Requires Repeated Tetanization. *Learn Mem.* *1*, 74–82.
- Huang, P.-S., Oberdorfer, G., Xu, C., Pei, X.Y., Nannenga, B.L., Rogers, J.M., DiMaio, F., Gonen, T., Luisi, B., and Baker, D. (2014). High thermodynamic stability of parametrically designed helical bundles. *Science* *346*, 481–485.
- Huang, P.-S., Boyken, S.E., and Baker, D. (2016). The coming of age of de novo protein design. *Nature* *537*, 320–327.
- Indelicato, G., Wahome, N., Ringler, P., Müller, S.A., Nieh, M.-P., Burkhard, P., and Twarock, R. (2016). Principles Governing the Self-Assembly of Coiled-Coil Protein Nanoparticles. *Biophys. J.* *110*, 646–660.
- Kandel, E.R., Dudai, Y., and Mayford, M.R. (2014). The molecular and systems biology of memory. *Cell* *157*, 163–186.
- King, N.P., Sheffler, W., Sawaya, M.R., Vollmar, B.S., Sumida, J.P., André, I., Gonen, T., Yeates, T.O., and Baker, D. (2012). Computational design of self-assembling protein nanomaterials with atomic level accuracy. *Science* *336*, 1171–1174.
- King, N.P., Bale, J.B., Sheffler, W., McNamara, D.E., Gonen, S., Gonen, T., Yeates, T.O., and Baker, D. (2014). Accurate design of co-assembling multi-component protein nanomaterials. *Nature* *510*, 103–108.
- Klapoetke, N.C., Murata, Y., Kim, S.S., Pulver, S.R., Birdsey-Benson, A., Cho, Y.K., Morimoto, T.K., Chuong, A.S., Carpenter, E.J., Tian, Z., et al. (2014). Independent optical excitation of distinct neural populations. *Nat. Methods* *11*, 338–346.
- Ku, T., Swaney, J., Park, J.Y., Albanese, A., Murray, E., Cho, J.H., Park, Y.G., Mangena, V., Chen, J., and Chung, K. (2016). Multiplexed and scalable super-resolution imaging of three-dimensional protein localization in size-adjustable tissues. *Nat. Biotechnol.* *34*, 973–981.
- Lai, Y.-T., Cascio, D., and Yeates, T.O. (2012). Structure of a 16-nm cage designed by using protein oligomers. *Science* *336*, 1129.
- Lai, Y.-T., Reading, E., Hura, G.L., Tsai, K.-L., Laganowsky, A., Asturias, F.J., Tainer, J.A., Robinson, C.V., and Yeates, T.O. (2014). Structure of a designed protein cage that self-assembles into a highly porous cube. *Nat. Chem.* *6*, 1065–1071.
- Lai, Y.-T., Hura, G.L., Dyer, K.N., Tang, H.Y.H., Tainer, J.A., and Yeates, T.O. (2016). Designing and defining dynamic protein cage nanoassemblies in solution. *Sci. Adv.* *2*, e1501855, e1501855.
- Lee, H.K., Kameyama, K., Huganir, R.L., and Bear, M.F. (1998). NMDA induces long-term synaptic depression and dephosphorylation of the GluR1 subunit of AMPA receptors in hippocampus. *Neuron* *21*, 1151–1162.
- Lin, J.R., Izar, B., Wang, S., Yapp, C., Mei, S., Shah, P.M., Santagata, S., and Sorger, P.K. (2018). Highly multiplexed immunofluorescence imaging of human tissues and tumors using t-CyCIF and conventional optical microscopes. *eLife* *7*, e31657.
- Mao, L., Yang, L., Arora, A., Choe, E.S., Zhang, G., Liu, Z., Fibuch, E.E., and Wang, J.Q. (2005). Role of protein phosphatase 2A in mGluR5-regulated MEK/ERK phosphorylation in neurons. *J. Biol. Chem.* *280*, 12602–12610.
- Mehta, S., and Zhang, J. (2011). Reporting from the field: genetically encoded fluorescent reporters uncover signaling dynamics in living biological systems. *Annu. Rev. Biochem.* *80*, 375–401.
- Mehta, S., Zhang, Y., Roth, R.H., Zhang, J.F., Mo, A., Tenner, B., Huganir, R.L., and Zhang, J. (2018). Single-fluorophore biosensors for sensitive and multiplexed detection of signalling activities. *Nat. Cell Biol.* *20*, 1215–1225.
- Micheva, K.D., and Smith, S.J. (2007). Array tomography: a new tool for imaging the molecular architecture and ultrastructure of neural circuits. *Neuron* *55*, 25–36.
- Moll, J.R., Ruvinov, S.B., Pastan, I., and Vinson, C. (2001). Designed heterodimerizing leucine zippers with a range of pIs and stabilities up to 10(–15) M. *Protein Sci.* *10*, 649–655.
- Murphy, J.G., Sanderson, J.L., Gorski, J.A., Scott, J.D., Catterall, W.A., Sather, W.A., and Dell’Acqua, M.L. (2014). AKAP-anchored PKA maintains neuronal L-type calcium channel activity and NFAT transcriptional signaling. *Cell Rep.* *7*, 1577–1588.
- Murray, E., Cho, J.H., Goodwin, D., Ku, T., Swaney, J., Kim, S.-Y., Choi, H., Park, Y.-G., Park, J.-Y., Hubbert, A., et al. (2015). Simple, Scalable Proteomic Imaging for High-Dimensional Profiling of Intact Systems. *Cell* *163*, 1500–1514.
- Negron, C., and Keating, A.E. (2014). A set of computationally designed orthogonal antiparallel homodimers that expands the synthetic coiled-coil toolkit. *J. Am. Chem. Soc.* *136*, 16544–16556.
- Oakley, M.G., and Kim, P.S. (1998). A buried polar interaction can direct the relative orientation of helices in a coiled coil. *Biochemistry* *37*, 12603–12610.

- Ohta, Y., Furuta, T., Nagai, T., and Horikawa, K. (2018). Red fluorescent cAMP indicator with increased affinity and expanded dynamic range. *Sci. Rep.* **8**, 1866.
- Oliveira, A.F., and Yasuda, R. (2013). An improved Ras sensor for highly sensitive and quantitative FRET-FLIM imaging. *PLoS ONE* **8**, e52874.
- Otsuguro, K., Gautam, S.H., Ito, S., Habara, Y., and Saito, T. (2005). Characterization of forskolin-induced Ca²⁺ signals in rat olfactory receptor neurons. *J. Pharmacol. Sci.* **97**, 510–518.
- Piatkevich, K.D., Jung, E.E., Straub, C., Linghu, C., Park, D., Suk, H.J., Hochbaum, D.R., Goodwin, D., Pneumatikakis, E., Pak, N., et al. (2018). A robotic multidimensional directed evolution approach applied to fluorescent voltage reporters. *Nat. Chem. Biol.* **14**, 352–360.
- Qian, H., Patriarchi, T., Price, J.L., Matt, L., Lee, B., Nieves-Cintrón, M., Buonarati, O.R., Chowdhury, D., Nanou, E., Nystoriak, M.A., et al. (2017). Phosphorylation of Ser1928 mediates the enhanced activity of the L-type Ca²⁺ channel Cav1.2 by the β 2-adrenergic receptor in neurons. *Sci. Signal.* **10**, eaaf9659.
- Redmond, L., Kashani, A.H., and Ghosh, A. (2002). Calcium regulation of dendritic growth via CaM kinase IV and CREB-mediated transcription. *Neuron* **34**, 999–1010.
- Roberson, E.D., and David Sweatt, J. (1996). Transient Activation of Cyclic AMP-dependent Protein Kinase during Hippocampal Long-term Potentiation **271**, 30436–30441.
- Sassone-Corsi, P. (2012). The cyclic AMP pathway. *Cold Spring Harb. Perspect. Biol.* **4**, a011148.
- Schmidt, U., Weigert, M., Broaddus, C., and Myers, G. (2018). Cell detection with star-convex polygons. *Lecture Notes in Computer Science (Including Subseries Lecture Notes in Artificial Intelligence and Lecture Notes in Bioinformatics)* (Springer Verlag), pp. 265–273.
- Shekhawat, S.S., Porter, J.R., Sriprasad, A., and Ghosh, I. (2009). An autoinhibited coiled-coil design strategy for split-protein protease sensors. *J. Am. Chem. Soc.* **131**, 15284–15290.
- Shelly, M., Lim, B.K., Cancedda, L., Heilshorn, S.C., Gao, H., and Poo, M.M. (2010). Local and long-range reciprocal regulation of cAMP and cGMP in axon/dendrite formation. *Science* **327**, 547–552.
- Sheng, M., Thompson, M.A., and Greenberg, M.E. (1991). CREB: a Ca(2+)-regulated transcription factor phosphorylated by calmodulin-dependent kinases. *Science* **252**, 1427–1430.
- Shimozono, S., Imura, T., Kitaguchi, T., Higashijima, S., and Miyawaki, A. (2013). Visualization of an endogenous retinoic acid gradient across embryonic development. *Nature* **496**, 363–366.
- Skeberdis, V.A., Chevaleyre, V., Lau, C.G., Goldberg, J.H., Pettit, D.L., Suadican, S.O., Lin, Y., Bennett, M.V.L., Yuste, R., Castillo, P.E., and Zukin, R.S. (2006). Protein kinase A regulates calcium permeability of NMDA receptors. *Nat. Neurosci.* **9**, 501–510.
- Tarantino, N., Tinevez, J.Y., Crowell, E.F., Boisson, B., Henriques, R., Mhlanga, M., Agou, F., Israël, A., and Laplantine, E. (2014). TNF and IL-1 exhibit distinct ubiquitin requirements for inducing NEMO-IKK supramolecular structures. *J. Cell Biol.* **204**, 231–245.
- Tenner, B., Getz, M., Ross, B., Ohadi, D., Bohrer, C.H., Greenwald, E., Mehta, S., Xiao, J., Rangamani, P., and Zhang, J. (2020). Spatially compartmentalized phase regulation of a Ca²⁺-cAMP-PKA oscillatory circuit. *bioRxiv*, 10.902312.
- Thévenaz, P., Ruttimann, U.E., and Unser, M. (1998). A pyramid approach to subpixel registration based on intensity. *IEEE Trans. Image Process.* **7**, 27–41.
- Thomson, A.R., Wood, C.W., Burton, A.J., Bartlett, G.J., Sessions, R.B., Brady, R.L., and Woolfson, D.N. (2014). Computational design of water-soluble α computational desi. *Science* **346**, 485–488.
- Tillberg, P.W., Chen, F., Piatkevich, K.D., Zhao, Y., Yu, C.C., English, B.P., Gao, L., Martorell, A., Suk, H.J., Yoshida, F., et al. (2016). Protein-retention expansion microscopy of cells and tissues labeled using standard fluorescent proteins and antibodies. *Nat. Biotechnol.* **34**, 987–992.
- Tinevez, J.-Y., Perry, N., Schindelin, J., Hoopes, G.M., Reynolds, G.D., Laplantine, E., Bednarek, S.Y., Shorte, S.L., and Eliceiri, K.W. (2017). TrackMate: An open and extensible platform for single-particle tracking. *Methods* **115**, 80–90.
- Tripet, B., Yu, L., Bautista, D.L., Wong, W.Y., Irvin, R.T., and Hodges, R.S. (1996). Engineering a de novo-designed coiled-coil heterodimerization domain off the rapid detection, purification and characterization of recombinantly expressed peptides and proteins. *Protein Eng.* **9**, 1029–1042.
- Trudeau, L.E., Emery, D.G., and Haydon, P.G. (1996). Direct modulation of the secretory machinery underlies PKA-dependent synaptic facilitation in hippocampal neurons. *Neuron* **17**, 789–797.
- Van der Zee, E.A., and Douma, B.R.K. (1997). Historical review of research on protein kinase C in learning and memory. *Prog. Neuropsychopharmacol. Biol. Psychiatry* **21**, 379–406.
- Vinkenborg, J.L., Nicolson, T.J., Bellomo, E.A., Koay, M.S., Rutter, G.A., and Merckx, M. (2009). Genetically encoded FRET sensors to monitor intracellular Zn²⁺ homeostasis. *Nat. Methods* **6**, 737–740.
- Violin, J.D., Zhang, J., Tsien, R.Y., and Newton, A.C. (2003). A genetically encoded fluorescent reporter reveals oscillatory phosphorylation by protein kinase C. *J. Cell Biol.* **161**, 899–909.
- Waltereit, R., and Weller, M. (2003). Signaling from cAMP/PKA to MAPK and synaptic plasticity. *Mol. Neurobiol.* **27**, 99–106.
- Wang, G., Jones, S.J.M., Marra, M.A., and Sadar, M.D. (2006). Identification of genes targeted by the androgen and PKA signaling pathways in prostate cancer cells. *Oncogene* **25**, 7311–7323.
- Weigert, M., Schmidt, U., Haase, R., Sugawara, K., and Myers, G. (2019). Star-convex Polyhedra for 3D Object Detection and Segmentation in Microscopy. *arXiv*, 1908.03636.
- Wong, S.T., Athos, J., Figueroa, X.A., Pineda, V.V., Schaefer, M.L., Chavkin, C.C., Muglia, L.J., and Storm, D.R. (1999). Calcium-stimulated adenylyl cyclase activity is critical for hippocampus-dependent long-term memory and late phase LTP. *Neuron* **23**, 787–798.
- Zaccari, N.R., Chi, B., Thomson, A.R., Boyle, A.L., Bartlett, G.J., Bruning, M., Linden, N., Sessions, R.B., Booth, P.J., Brady, R.L., and Woolfson, D.N. (2011). A de novo peptide hexamer with a mutable channel. *Nat. Chem. Biol.* **7**, 935–941.
- Zanassi, P., Paolillo, M., Feliciello, A., Avvedimento, E.V., Gallo, V., and Schinelli, S. (2001). cAMP-dependent protein kinase induces cAMP-response element-binding protein phosphorylation via an intracellular calcium release/ERK-dependent pathway in striatal neurons. *J. Biol. Chem.* **276**, 11487–11495.
- Zhang, Q., Huang, H., Zhang, L., Wu, R., Chung, C.-I., Zhang, S.-Q., Torra, J., Schepis, A., Coughlin, S.R., Kornberg, T.B., and Shu, X. (2018). Visualizing Dynamics of Cell Signaling In Vivo with a Phase Separation-Based Kinase Reporter. *Mol. Cell* **69**, 334–346.

STAR★METHODS

KEY RESOURCES TABLE

REAGENT or RESOURCE	SOURCE	IDENTIFIER
Antibodies		
Anti-Xpress Antibody, Mouse	Invitrogen, Thermofisher Scientific	Cat#R910-25; RRID: AB_2556552
Anti-V5 Antibody, Chicken	Abcam	Cat#ab9113; RRID: AB_307022
Anti-HA Antibody, Rabbit	Abcam	Cat#ab9110; RRID: AB_307019
Anti-E-epitope Antibody, Rabbit	Genscript	Cat#A00631; RRID: AB_914600
Anti-OLLAS Antibody, Rat	Invitrogen, Thermofisher Scientific	Cat#MA5-16125; RRID: AB_11152481
Anti-FLAG Antibody, Rabbit	Invitrogen, Thermofisher Scientific	Cat# 740001; RRID: AB_2610628
Anti-Synaptophysin, Mouse	Millipore Sigma	Cat#S5768; RRID: AB_477523
Anti-phospho-Histone H2A.X, Mouse	Millipore Sigma	Cat#05-636; RRID: AB_309864
Anti-AIF, Rabbit	Cell Signaling Technology	Cat#8653, kit; RRID: AB_10634755
Anti-EEA1, Rabbit	Cell Signaling Technology	Cat#8653, kit; RRID: AB_2096811
Anti-LAMP1, Rabbit	Cell Signaling Technology	Cat#8653, kit; RRID: AB_2687579
Anti-PDI, Rabbit	Cell Signaling Technology	Cat#8653, kit; RRID: AB_2156433
Anti-RCAS1, Rabbit	Cell Signaling Technology	Cat#8653, kit; RRID: AB_2736985
Anti-Cleaved Caspase-3, Rabbit	Cell Signaling Technology	Cat#9664T; RRID: AB_2070042
Anti-GFAP, Rabbit	Cell Signaling Technology	Cat#12389T; RRID: AB_2631098
Anti-NeuN, Guinea Pig	Synaptic Systems	Cat#266004; RRID: AB_2619988
Anti-Iba1, Rabbit	Wako Chemicals	Cat#019-19741; RRID: AB_839504
Goat Anti-Guinea Pig IgG (H+L) Secondary Antibody, Alexa Fluor 647	Abcam	Cat#ab150187; RRID: AB_2827756
Goat Anti-Mouse IgG (H+L) Secondary Antibody, Alexa Fluor 647	Abcam	Cat#ab150115; RRID: AB_2687948
Goat Anti-Mouse IgG (H+L) Highly Cross-Adsorbed Secondary Antibody, Alexa Fluor 594	Invitrogen, Thermofisher Scientific	Cat#A-11032; RRID: AB_2534091
Goat Anti-Mouse IgG1 Cross-Adsorbed Secondary Antibody, Alexa Fluor 546	Invitrogen, Thermofisher Scientific	Cat#A-21123; RRID: AB_141592
Goat Anti-Chicken IgY (H+L) Secondary Antibody, Alexa Fluor 647	Invitrogen, Thermofisher Scientific	Cat#A-21449; RRID: AB_2535866
Goat Anti-Chicken IgY (H+L), Cross-Adsorbed Secondary Antibody, Alexa Fluor 594	Invitrogen, Thermofisher Scientific	Cat#A32759; RRID: AB_2762829
Goat Anti-Chicken IgY (H+L) Secondary Antibody, CF543	Biotium	Cat#20311
Goat Anti-Rabbit IgG (H+L) Secondary Antibody, Alexa Fluor 647	Invitrogen, Thermofisher Scientific	Cat#A-21245; RRID: AB_2535813
Goat Anti-Rabbit IgG (H+L), Highly Cross-Adsorbed Secondary Antibody, Alexa Fluor 594	Invitrogen, Thermofisher Scientific	Cat#A32740; RRID: AB_2762824
Donkey Anti-Rabbit IgG (H+L), Highly Cross-Adsorbed Secondary Antibody, CF543	Biotium	Cat#20308
Goat Anti-Rat IgG (H+L), Cross-Adsorbed Secondary Antibody, Alexa Fluor 647	Invitrogen, Thermofisher Scientific	Cat#A-21247; RRID: AB_141778
Donkey Anti-Rat IgG (H+L), Highly Cross-Adsorbed Secondary Antibody, Alexa Fluor 594	Invitrogen, Thermofisher Scientific	Cat#A-21209; RRID: AB_2535795

(Continued on next page)

Continued

REAGENT or RESOURCE	SOURCE	IDENTIFIER
FISH Probes		
MBS probe (GACATGGGTGATCCTCATGT)	This study; LGC Biosearch Technologies	N/A
MBS/PBS Linker 1 probe (ATCTAATGAACCCGGAATA)	This study; LGC Biosearch Technologies	N/A
MBS/PBS Linker 2 probe (TTCTAGGCAATTAGGTACCT)	This study; LGC Biosearch Technologies	N/A
PBS 1 probe (AGCGACGCCATATCGTCTGC)	This study; LGC Biosearch Technologies	N/A
PBS 2 probe (AGCGAGCCCATATGCTCTGC)	This study; LGC Biosearch Technologies	N/A
Bacterial and Virus Strains		
NEB Stable Competent <i>E. coli</i>	New England Biolabs	Cat#C3040I & C3040H
Z-Competent <i>E. coli</i>	Zymo Research	Cat#T3001 & T3002
AAV-2/9-hSyn-mRuby3-6xFLAG	Janelia Viral Tools Facility	N/A
AAV-DJ-CAG-GCaMP6f	Janelia Viral Tools Facility	N/A
AAV-DJ-UBC-S1-GCaMP6f	Janelia Viral Tools Facility	N/A
AAV-2/9-UBC-S2-cAMPr	Janelia Viral Tools Facility	N/A
AAV-2/9-UBC-S3-ExRaiAKAR	Janelia Viral Tools Facility	N/A
AAV-2/9-UBC-S4-ExRaiCKAR	Janelia Viral Tools Facility	N/A
AAV-2/9-UBC-S2a-cAMPr	Janelia Viral Tools Facility	N/A
Chemicals, Peptides, and Recombinant Proteins		
Dulbecco's Modified Eagle Media	GIBCO, ThermoFisher Scientific	Cat#11995040
Heat inactivated fetal bovine serum	Corning, VWR	Cat#45000-736
Penicillin/Streptomycin	GIBCO, ThermoFisher Scientific	Cat#15140-22
Sodium pyruvate	GIBCO, ThermoFisher Scientific	Cat#11360070
Matrigel	Corning, VWR	Cat#47743-715
Papain	Worthington Biochem	Cat#3126
Ovomucoid trypsin inhibitor	Worthington Biochem	Cat#LS003087
Minimum Essential Media, no glutamine, no phenol	Life Technologies	Cat#51200-038
Glucose	Millipore Sigma	Cat#G7528
Holo-Transferrin bovine	Millipore Sigma	Cat#T1283
HEPES	Millipore Sigma	Cat#H3375
glutaGRO	Corning, VWR	Cat#45001-086
Insulin	Millipore Sigma	Cat#407709
B27 supplement	GIBCO, ThermoFisher Scientific	Cat#17504-044
AraC	Millipore Sigma	Cat#C6645
Acetic acid	Millipore Sigma	Cat#A6283
NucBlue Live ReadyProbes Reagent	Invitrogen, ThermoFisher	Cat#R37605
Calcium chloride	Millipore Sigma	Cat#C5080
Choline chloride	Millipore Sigma	Cat#C1879
Magnesium chloride	Millipore Sigma	Cat#M2670
D-glucose	Millipore Sigma	Cat#G7528
Ascorbic acid	Millipore Sigma	Cat#A5960
Pyruvic acid	Millipore Sigma	Cat#P8574

(Continued on next page)

Continued

REAGENT or RESOURCE	SOURCE	IDENTIFIER
Sodium chloride	Millipore Sigma	Cat#S7653
Magnesium sulfate	Millipore Sigma	Cat#63138
Potassium chloride	Millipore Sigma	Cat#P5405
Sodium bicarbonate	Millipore Sigma	Cat#S6297
Sodium phosphate	Millipore Sigma	Cat#71507
Forskolin	Millipore Sigma	Cat#F6886
Phorbol 12-myristate 13-acetate (PMA)	Millipore Sigma	Cat#P8139
(S)-3,5-Dihydroxyphenylglycine hydrate (S-DHPG)	Millipore Sigma	Cat#D3689
GABAzine	Tocris Bioscience	Cat#1262
NBQX	Tocris Bioscience	Cat#0373
TissuePrep buffered 10% formalin	Electron Microscopy Sciences	Cat#15742-10
Glycine	Millipore Sigma	Cat#G5417
Normal donkey serum	ThermoFisher Scientific	Cat#01-6201
Normal horse serum	ThermoFisher Scientific	Cat#31874
Normal bovine serum	Abcam	Cat#ab7479
Fast Green FCF dye	Millipore Sigma	Cat#68724
Formamide	Millipore Sigma	Cat#F9037
Dextran sulfate	Millipore Sigma	Cat#42867
acryloyl-X (6-((acryloyl)amino)hexanoic acid, succinimidyl ester (AcX)	ThermoFisher Scientific	Cat#A20770
anhydrous DMSO	ThermoFisher Scientific	Cat#D12345
N,N'-methylenebisacrylamide	Millipore Sigma	Cat#M7279
Sodium acrylate	Millipore Sigma	Cat#408220
Acrylamide	Millipore Sigma	Cat#A9099
4-hydroxy-2,2,6,6-tetramethylpiperidin-1-oxyl (4HT)	Millipore Sigma	Cat#176141
Tetramethylethylenediamine (TEMED)	Millipore Sigma	Cat#411019
Ammonium persulfate (APS)	Millipore Sigma	Cat#248614
Sodium dodecyl sulfate (SDS)	Millipore Sigma	Cat#L6026
β -mercaptoethanol	Millipore Sigma	Cat#M6250
Tris-Ethylenediaminetetraacetic acid (EDTA)	Millipore Sigma	Cat#93283
Tris, 1 M, 8 pH	Life Technologies	Cat#AM9855
MAXBlock Blocking medium	Active Motif	Cat#15252
MAXWash Washing medium	Active Motif	Cat#15254
MAXStain Staining medium	Active Motif	Cat#15253
Critical Commercial Assays		
Plasmid mini-prep kit	QIAGEN	Cat#27104
TransIT-X2 Dynamic Delivery System kit	Mirus Bio, VWR	Cat#10766-888
Calcium phosphate transfection kit	Invitrogen, ThermoFisher Scientific	Cat#K278001
Experimental Models: Cell Lines		
HeLa	ATCC	CCL-2
Experimental Models: Organisms/Strains		
Swiss Webster mice, pregnant female	Taconic	N/A
Recombinant DNA		
See Tables S1 and S2	This study	N/A

(Continued on next page)

Continued

REAGENT or RESOURCE	SOURCE	IDENTIFIER
Deposited Data		
Sequences of SiRIs	This study	GenBank: MT449928, GenBank: MT449929, GenBank: MT449930, GenBank: MT449931, GenBank: MT449932, GenBank: MT449933, GenBank: MT449934, GenBank: MT449935
Software and Algorithms		
StarDist	(Schmidt et al., 2018; Weigert et al., 2019)	https://github.com/mpicbg-csbd/stardist
ImageJ	NIH	https://imagej.nih.gov/ij/download.html
Fiji software GPL v2	Fiji	https://fiji.sc/Fiji
TrackMate	(Tinevez et al., 2017)	https://imagej.net/TrackMate
StackReg	(Thévenaz, Ruttimann and Unser, 1998)	http://bigwww.epfl.ch/thevenaz/stackreg/
MultiStackReg v1.45	http://bradbusse.net/	http://bradbusse.net/downloads.html
MATLAB	Mathworks	https://www.mathworks.com/
MATLAB script, msd analyzer	(Tarantino et al., 2014)	https://www.mathworks.com/matlabcentral/fileexchange/40692-mean-square-displacement-analysis-of-particles-trajectories
Prism	Graphpad	https://www.graphpad.com/scientific-software/prism/
Other		
Inverted epi-fluorescence wide-field Nikon Eclipse Ti microscope	Nikon	N/A
SPECTRA X light engine	LumenCor	N/A
Confocal Scanner Unit	Yokogawa	Cat#CSU-W1
Zyla 5.5 Megapixel camera	Andor	N/A
Zyla PLUS 4.2 Megapixel camera	Andor	N/A
40X 1.15 NA water immersion objective	Nikon	Cat#MRD77410
438/24 nm donor excitation filter, for CFP/YFP FRET reporter (ICUE3 and AKAR4)	Semrock	N/A
483/32 nm CFP emission filter, for CFP/YFP FRET reporter (ICUE3 and AKAR4)	Semrock	N/A
542/27 nm YFP emission filter, for CFP/YFP FRET reporter (ICUE3 and AKAR4)	Semrock	N/A
527/50 nm emission filter, for GFP based reporters (GCaMP6f, cAMP _r , ExRaiAKAR, ExRaiCKAR)	Semrock	N/A
582/15 nm emission filter, for RFP based reporter (RAB_EKARev)	Semrock	N/A
631/28 nm excitation filter, for miRFP	Semrock	N/A
664 long-pass emission filter, for miRFP	Semrock	N/A
Glass coverslips, round, diameter 12 mm, thickness 0.09-0.12 mm	Carolina	Cat#633009
Platinum tweezerrode, 5 mm	BTX Online	Cat#45-0489
ECM 830 electroporator	Harvard Apparatus	Cat#W3 45-005
Axopatch 200B amplifier	Molecular Devices	N/A
Multiclamp 700B Microelectrode amplifier	Molecular Devices	N/A
Digidata 1440 digitizer	Molecular Devices	N/A
Digidata 1550B plus Humslinger	Molecular Devices	N/A
Compressome VF-300	Precisionary Instruments	N/A

(Continued on next page)

Continued

REAGENT or RESOURCE	SOURCE	IDENTIFIER
Flaming/Brown micropipette puller	Sutter Instruments	Cat#P-97
Borosilicate glass pipettes with filament	Warner Instruments	Cat#G120F-4
RC-41LP, quick change chamber, low profile	Warner Instruments	Cat#64-0368
DH-40iL, culture dish incubation system	Warner Instruments	Cat#64-0388
SHD-41/15, slice anchor for RC-41LP chamber	Warner Instruments	Cat#64-1418
SH-8/60, syringe holder with eight 60 cc syringes	Warner Instruments	Cat#64-0385
Model 75 RN syringe, 5 μ L, for DNA and AAV injections into mouse brain	Hamilton Company	Cat#7634-01
Small hub RN needle, 32 gauge, for DNA and AAV injections into mouse brain	Hamilton Company	Cat#7803-04

RESOURCE AVAILABILITY

Lead Contact

Further information and requests for resources and reagents should be directed to and will be fulfilled by the Lead Contact, Edward S. Boyden (edboyden@mit.edu).

Materials Availability

Plasmids generated in this study are available at Addgene (Addgene plasmid # 160722-160728 and 161613-161614).

Data and Code Availability

The accession numbers for the sequences of SiRIs reported in this paper are GenBank: MT449928, GenBank: MT449929, GenBank: MT449930, GenBank: MT449931, GenBank: MT449932, GenBank: MT449933, GenBank: MT449934, GenBank: MT449935.

EXPERIMENTAL MODEL AND SUBJECT DETAILS

All procedures involving animals at MIT were conducted in accordance with the US National Institutes of Health Guide for the Care and Use of Laboratory Animals and approved by the Massachusetts Institute of Technology Committee on Animal Care.

NEB Stable Competent *E. coli* (New England Biolabs) were used for small-scale isolation of plasmids encoding repetitive RNA scaffolds and were grown in a shaking incubator (250 RPM) at 30°C. Small-scale isolations of all other plasmids were done with Z-Competent *E. coli* (Zymo Research) grown in a shaking incubator (250 RPM) at 37°C.

HeLa cells, passage 5-12 (ATCC) were maintained between 10% and 90% confluence at 37°C with 5% CO₂ in DMEM (GIBCO) with the addition of 10% heat inactivated fetal bovine serum (HI-FBS) (Corning), 1% penicillin/streptomycin (GIBCO), and 1% sodium pyruvate (GIBCO). Cells were authenticated by the manufacturer and tested for mycoplasma contamination to their standard levels of stringency and were here used because they are common cell lines for testing new tools (we are not explicitly studying the biology of these cells since they were only used for technology development and testing, in this paper). Transfection and recordings for experiments that did not involve post hoc RNA FISH proceeded in glass 24-well plates treated with 75 μ L diluted Matrigel (250 μ L Matrigel (Corning) diluted in 12 mL DMEM) per well at 37°C for 30-60 minutes. Transfection and recordings for experiments involving post hoc RNA FISH proceeded on glass coverslips (Carolina) treated with diluted Matrigel in glass 24-well plates.

Hippocampal neurons were prepared from postnatal day 0 or 1 Swiss Webster mice (Taconic) (both male and female mice were used) as previously described ([Klapoetke et al., 2014](#)) with the following modifications: dissected hippocampal tissue was digested with 50 units of papain (Worthington Biochem) for 6-8 min, and the digestion was stopped with ovomucoid trypsin inhibitor (Worthington Biochem). Cells were plated at a density of 20,000-30,000 per glass coverslip coated with diluted Matrigel in a 24-well plate. Neurons were seeded in 100 μ L plating medium containing MEM (no glutamine, no phenol, Life Technologies), glucose (33 mM, Millipore Sigma), holo-Transferrin bovine (0.01%, Millipore Sigma), HEPES (10 mM, Millipore Sigma), glutaGRO (2 mM, Corning), insulin (0.13%, Millipore Sigma), B27 supplement (2%, GIBCO), and HI-FBS. After cell adhesion, additional plating medium was added. AraC (0.002 mM, Millipore Sigma) was added when glial density was 50%–70% of confluence. Neurons were grown at 37°C and 5% CO₂ in a humidified atmosphere.

METHOD DETAILS

Molecular Cloning

The DNAs encoding the protein motifs (mammalian-codon optimized), the 24x MS2 binding sites (24x MBS), and the 24x PP7 binding sites (24x PBS) used in this study were synthesized by Epoch Life Science or GenScript. The 48x MS2 binding sites (48x MBS) and

72x PP7 binding sites (72x PBS) were cloned from 24x MS2 and 24x PP7 arrays using the restriction cloning method described in (Golding and Cox, 2004). The reporter vectors for RNA scaffold-based clustering strategies were cloned into the pAAV-UBC backbone. The scaffold vectors for RNA scaffold-based clustering strategies were cloned into the pAAV-CAG backbone. The vectors for protein scaffold-based clustering strategies were cloned into the pAAV-UBC (for transfection in cultured cells and AAV production by the Janelia Viral Tools Facility) and pAAV-CAG (for in utero electroporation) backbones. Constructs for unassembled reporters, pAAV-CAG-GCaMP6f and pcDNA3-CMV-ICUE3, were used in the single reporter control experiments in HeLa cells. Unassembled reporters, GCaMP6f, cAMP_r, ExRaiAKAR, ExRaiCKAR, and RAB_EKAR_{rev}, were cloned into pAAV-UBC backbone for the single reporter control experiments in neurons. See Table S1 for sequences of the motifs; see Table S2 for all tested constructs.

Small-scale isolation of plasmid DNA was performed with Plasmid Mini-Prep kits (QIAGEN), after transformation in either NEB Stable Competent *E. coli* (New England Biolabs) for plasmids encoding repetitive RNA scaffolds or in Z-Competent DH5a *E. coli* (Zymo Research) for plasmids that did not encode repetitive RNA scaffolds, per manufacturer's protocols.

Transfection

The DNA was transiently transfected into HeLa cells using a TransIT-X2 Dynamic Delivery System kit (Mirus Bio). The 250-500 ng of total plasmid DNA per well was transfected into HeLa cells according to the manufacturer's protocol. Cell culture media in the wells was changed to fresh media 24 hours after transfection. The cells were then incubated for another 24 hours before live cell imaging.

Cultured neurons were transfected at 4-5 days *in vitro* (DIV) with a commercial calcium phosphate transfection kit (Invitrogen) as previously described (Piatkevich et al., 2018). Briefly, for transfection in each coverslip/well in the 24-well plate, 250-900 ng of total plasmid of interest (100-300 ng of each plasmid when co-transfecting multiple plasmids), 100-200 ng pAAV-hSyn-miRFP plasmid as a cell morphology marker, and pUC19 plasmid as a 'dummy' DNA plasmid to bring the total amount of DNA to 1500 ng (to avoid variation in DNA-calcium phosphate co-precipitate formation) were used. The cells were washed with acidic MEM buffer (containing 15 mM HEPES with final pH 6.7-6.8 adjusted with acetic acid (Millipore Sigma)) after 45-60 minutes of calcium phosphate precipitate incubation to remove residual precipitates. The neurons were then incubated for another 4-5 days before live cell imaging at 8-9 DIV.

In Utero Electroporation

Embryonic day (E) 15.5 timed-pregnant female Swiss Webster (Taconic Biosciences) mice were deeply anaesthetized with 2% isoflurane. Uterine horns were exposed and periodically rinsed with warm sterile 1X PBS. Plasmid DNA mixture was injected into the lateral ventricle of one cerebral hemisphere of an embryo using a 32-gauge needle (Hamilton Company) attached to a 5 μ L syringe (Hamilton Company). Final plasmid DNA concentration was 4.5 μ g/ μ L in water (DNA mass ratio of pAAV-CAG-S1-GCaMP6f, pAAV-CAG-S3-ExRaiAKAR, and pAAV-CAG-mRuby3-6xFLAG at 1:2:2). Fast Green FCF dye (Millipore Sigma) was added to the DNA mixture to visualize the mixture during injection. Five voltage pulses (50 V, 50 ms duration, 1 Hz) were delivered two times using 5-mm round plate electrodes (Harvard Apparatus), with the cathode placed on top of the skull to target the hippocampus. Electroporated embryos were placed back into the dam, and allowed to mature for delivery.

Fluorescence Microscopy of HeLa cells and Primary Neurons

HeLa cells were imaged 48 hours after transfection. For 10-15 minutes at 37°C right before imaging, 10 μ L of NucBlue Live ReadyProbes Reagent (Invitrogen) was added to the media to stain the cell nucleus after which the media was replaced with Fluorobrite DMEM supplemented with 15 mM HEPES. Live cell imaging of HeLa cells was performed on an inverted epi-fluorescence wide-field Nikon Eclipse Ti microscope with a 40X 1.15 NA water immersion objective (Nikon MRD77410), a SPECTRA X light engine (Lumen-Cor), and a Zyla 5.5 camera (Andor) controlled by NIS-Elements AR software. For imaging GFP intensity-based reporters (GCaMP6f and cAMP_r), a 475/28 nm excitation filter (Semrock) and a 527/50 nm emission filter (Semrock) were used. For imaging the CFP/YFP FRET-based reporters (ICUE3 and AKAR4), a 438/24 nm donor excitation filter (Semrock), a 483/32 nm CFP emission filter (Semrock), and a 542/27 nm YFP emission filter (Semrock) were used. For imaging miRFP, a 631/28 nm excitation filter (Semrock) and a 664 long-pass emission filter (Semrock) were used. Under the 40X objective, cells were recorded by volumetric imaging (1.0-1.5 μ m per Z step) for 5-15 minutes in the GFP, CFP and/or YFP channels at 10 s per volume (0.1 Hz), during which the reagents for extracellular stimulation, 10 mM final concentration of calcium chloride (Millipore Sigma) or 20 μ M final concentration of forskolin (Millipore Sigma), was added into the Fluorobrite media. After recording, images were taken under 40X and 10X objectives in the GFP, CFP, YFP, miRFP, and/or NucBlue channels, and then a tiled image in the NucBlue channel under the 4X objective covering the entire glass coverslip was taken to facilitate registration with the images from downstream immunostaining or RNA FISH. HeLa cells were fixed for 10 minutes in TissuePrep buffered 10% formalin (Electron Microscopy Sciences), followed by washing with 1X phosphate buffered saline (PBS) three times, 5 minutes each. If the cells were intended for downstream immunostaining, cells were stored in 1X PBS at 4°C. If the cells were for downstream RNA FISH, cells were stored in 70% ethanol at 4°C.

Live neuron imaging was performed on a spinning disk confocal microscope (a Yokogawa CSU-W1 Confocal Scanner Unit on a Nikon Eclipse Ti microscope) equipped with a 40X 1.15 NA water immersion objective (Nikon MRD77410) and a Zyla PLUS 4.2 Megapixel camera controlled by NIS-Elements AR software. The filter set for GFP was used for imaging GFP intensity-based reporters (GCaMP6f and cAMP_r), and the filter set for GFP and the 405 nm excitation filter was used for imaging 488 nm/405 nm excitation ratiometric reporters (ExRaiAKAR and ExRaiCKAR). The filter set for RFP was used for imaging RFP intensity-based reporters (RAB_EKAR_{rev}). For electrophysiological characterizations of GCaMP6f and S1-GCaMP6f (Figures 2D-2G and S1A-S1Q), neurons were

recorded in the GFP emission channel at a single focal plane at 20 ms per frame (50 Hz). In the characterization and spatially multiplexed imaging experiments in [Figures S1R–S1V](#), [S3D–S3G](#), and [S3M–S3O](#), neurons were recorded in the GFP emission channel at a single focal plane at 50 ms per frame (20 Hz). In all other primary neuron imaging experiments, neurons were recorded by volumetric imaging (1.0–1.5 μm per Z step) in the GFP emission channel only (about 5 s per volume; each X–Y plane in the volume was captured twice, one under 405 nm excitation and the other under 488 nm excitation; 405 nm excitation is for ExRaiAKAR and ExRaiCKAR) or in the GFP and RFP emission channels (about 30 s per volume; each X–Y plane in the volume was captured three times, one under 405 nm excitation and GFP emission, another under 488 nm excitation and GFP emission, the last one under 561 nm excitation and RFP emission; 561 nm excitation is for RAB_EKARev).

In the experiments in [Figures 2, 6, 7, S1, S3, S4, and S5](#) where the drug stimulations (forskolin, PMA, DHPG, or CaCl_2) were indicated by black downward arrows, drugs diluted in the corresponding media (Fluorobrite MEM for HeLa cells and MEM for cultured neurons) were added into the cell culture by pipetting gently dropwise. In the experiments in [Figures 3, 4, 5, 6, 7, S5, S6, and S7](#) where the drug stimulations (forskolin, PMA, or DHPG) were indicated by black horizontal bars, coverslips of cultured neurons were transferred to a perfusion chamber (Warner Instruments; RC-41LP plus DH-40iL) and continuously perfused with (blank) MEM for 10–15 minutes before imaging started. During the time periods indicated by the black horizontal bars, corresponding drugs diluted in MEM (50 μM for forskolin; 0.1 $\mu\text{g}/\text{ml}$ for PMA; 100 μM for DHPG) were perfused into the perfusion chamber instead of the blank MEM.

After recording, Z-stacks were taken in the GFP and miRFP channels under the 40X objective, and then a tiled image in the GFP channel under the 10X objective covering a 4-by-4 grid and a tiled image in the GFP channel under the 4X objective covering the entire glass coverslip were taken for the registration of live images with the images from downstream immunostaining. Cells were then fixed in TissuePrep buffered 10% formalin for 10–15 minutes at room temperature (RT), followed by incubation in 100 mM glycine (Millipore Sigma) in 1X PBS for 10–15 minutes at RT and three washes in 1X PBS, 5 minutes each at RT. Cells were stored in 1X PBS at 4°C until immunostaining.

Electrophysiology - Current and Voltage Clamp Recording of Cultured Neurons

Whole cell patch clamp recordings were performed using Axopatch 200B or Multiclamp 700B amplifiers, a Digidata 1440 digitizer, and a PC running pClamp (Molecular Devices). Cultured neurons were patched on DIV 14–18 (7–11 days after AAV transduction; AAVs were produced at Janelia Viral Tools Facility). Neurons were bathed in room temperature Tyrode solution containing 125 mM NaCl, 2 mM KCl, 3 mM CaCl_2 , 1 mM MgCl_2 , 10 mM HEPES, 30 mM glucose and the synaptic blockers 0.01 mM NBQX and 0.01 mM GABA_Azine. The Tyrode solution pH was adjusted to 7.3 with NaOH and the osmolarity was adjusted to 300 mOsm with sucrose. Borosilicate glass pipette (Warner Instruments) with an outer diameter of 1.2 mm and a wall thickness of 0.255 mm was pulled to a resistance of 5–10 M Ω with a P-97 Flaming/Brown micropipette puller (Sutter Instruments) and filled with a pipette solution containing 155 mM K-gluconate, 8 mM NaCl, 0.1 mM CaCl_2 , 0.6 mM MgCl_2 , 10 mM HEPES, 4 mM Mg-ATP, and 0.4 mM Na-GTP. The pipette solution pH was adjusted to 7.3 with KOH and the osmolarity was adjusted to 298 mOsm with sucrose.

Electrophysiology and Imaging of Acute Brain Slice

3 to 4 week old mice expressing SiRIs and miRFP (from in utero electroporation) were anesthetized with isoflurane and decapitated; the brains were taken out and placed in ice-cold choline-based cutting solution containing 110 mM choline chloride, 7 mM MgCl_2 , 2.5 mM KCl, 0.5 mM CaCl_2 , 1.25 mM NaHPO_4 , 25 mM NaHCO_3 , 25 mM D-glucose, 11.6 mM ascorbic acid, and 3.1 mM pyruvic acid with a final pH of 7.75. The sagittal brain slices containing the hippocampus (300 μm) were cut in cold choline-based cutting solution with a Compressstone VF-300 (Precisionary Instruments), transferred to a holding chamber containing ACSF (124 mM NaCl, 2 mM MgSO_4 , 2.5 mM KCl, 2 mM CaCl_2 , 1.2 mM NaHPO_4 , 24 mM NaHCO_3 , 5 mM HEPES, and 12.5 mM D-glucose with a final pH of 7.35), and allowed to recover for 20 minutes at 30–32°C. Slices were subsequently maintained at room temperature for 1–4 hours until use. The cutting solution, ACSF, and ACSF with 50 μM forskolin (or ‘forskolin-ACSF’) were constantly bubbled with 95% O_2 , 5% CO_2 . Slices were screened for positive green expression by a hand-held blue LED with a GFP filter set.

For electrophysiology, individual slices were transferred to a submersion perfusion chamber and continuously perfused with room temperature (23–26°C) ACSF, constantly bubbled with 95% O_2 , 5% CO_2 , at a 4–5 ml/minute rate. Recording pipettes (4–6M Ω resistance) for field excitatory postsynaptic potential (fEPSP) recording were pulled from borosilicate glass (Warner) and filled with ACSF. fEPSP recordings were made with a microelectrode amplifier (Multiclamp 700B, Molecular Devices). Signals were low-pass-filtered at 3 kHz and sampled at 20 kHz with a Digidata 1550B plus Humsilencer (Molecular Devices), and data were stored on a computer for subsequent offline analysis. Recording pipettes were placed in the stratum radiatum of CA1. All evoked responses were elicited by delivering constant current pulses (duration 0.2 ms, 0.05 Hz) through a bipolar tungsten stimulating electrode placed into the mid stratum radiatum to activate Schaffer collateral / commissural fibers. The intensity of current pulses was adjusted to about 50% of the intensity for the maximum fEPSP amplitude and maintained at that level throughout the fEPSP recordings for each slice. Chemical LTP was induced by perfusing forskolin-ACSF, instead of ACSF, to the slice for 15 minutes, after which the perfusion was switched back to ACSF. fEPSP was recorded every 3 minutes, from 12 minutes before the onset of forskolin-ACSF perfusion to 57 minutes after the onset of forskolin-ACSF perfusion, resulting in a total of 24 fEPSP responses per slice. fEPSP slopes were measured by calculating the slopes between 10%–60% of the fEPSP rising phase.

Acute brain slice imaging was performed on a spinning disk confocal microscope (a Yokogawa CSU-W1 Confocal Scanner Unit on a Nikon Eclipse Ti microscope) equipped with a 40X 1.15 NA water immersion objective (Nikon MRD77410) and a Zyla PLUS 4.2

Megapixel camera controlled by NIS-Elements AR software. Individual slices were transferred to a submersion perfusion chamber and continuously perfused with room temperature (23–26°C) ACSF, constantly bubbled with 95% O₂, 5% CO₂, at a 4–5 ml/minute rate.

For each slice, a volume containing the soma, apical dendrites, and basal dendrites of CA1 pyramidal neurons was imaged in the GFP (for SiRIs) and RFP (for the morphological marker mRuby3-FLAG) channels under the 40X objective and then under the 10X and 4X objectives. Volumetric time-lapse imaging (1.5–2.0 μm per Z step) of this volume was then performed in the GFP emission channel under the 40X objective (30 s per volume; each X–Y plane in the volume was captured twice, once under 405 nm excitation and the other under 488 nm excitation). Chemical stimulation was applied by perfusing forskolin-ACSF, instead of ACSF, to the slice for 15 minutes, after which the perfusion was switched back to ACSF. Time-lapse imaging started 5 minutes before the onset of forskolin-ACSF perfusion and ended 60 minutes after the onset of forskolin-ACSF perfusion, in a total of 65 minutes.

The slice was then fixed in TissuePrep buffered 10% formalin for 15 minutes at room temperature (RT), followed by incubation in 100 mM glycine in 1X PBS for 30 minutes at RT and three washes in 1X PBS, 5 minutes each at RT. The slice was stored in 1X PBS at 4°C until immunostaining.

Immunostaining of Cultured Cells

All solutions below were made in 1X PBS, and incubations carried out at room temperature. We observed that the miRFP fluorescence was not preserved after fixation, so we could use fluorescent antibodies that had spectral overlap with miRFP for immunostaining. Cells were permeabilized with 0.1% Triton X-100 for 15 minutes and then blocked with 5% normal donkey (ThermoFisher Scientific), horse (ThermoFisher Scientific), or bovine (Abcam) serum for 15 minutes. Cells were incubated with primary antibodies (see [Key Resources Table](#)) in blocking buffer at 1:400 for 1 hour, and then washed in 1X PBS three times for 5 minutes each. Cells were incubated with fluorescently-labeled secondary antibodies (see [Key Resources Table](#)) in blocking buffer at 1:400 for 2 hours for HeLa cells and 1 hour for cultured neurons, then washed in 1X PBS three times. Nuclei were stained with DAPI at 1 μg/ml for 1–5 minutes followed by 1X PBS wash. The cells were then stored in 1X PBS at 4°C until imaging.

Multiplexed Immunostaining of Cultured Cells

We used acryloyl-X (6-((acryloyl)amino)hexanoic acid, succinimidyl ester (AcX) (ThermoFisher Scientific) powder and dissolved in anhydrous DMSO (ThermoFisher Scientific) at a concentration of 10 mg/ml, and stored in a desiccated environment at –20°C. Cell cultures on round coverslips for [Figure 6I–Q](#) and [Figure 7H–K](#) were then incubated in 300–500 μL of AcX at a concentration of 0.1 mg/ml in 1X PBS with 0.5% Triton-X for 30 minutes at 4°C and then for 1.5 hours at 37°C. Then, cells were washed with 1X PBS three times for 5 minutes each.

We then prepared a monomer solution composed of 2 M NaCl (Sigma-Aldrich), 8.625% (w/v) sodium acrylate (Sigma-Aldrich), 2.5% (w/v) acrylamide (Sigma-Aldrich), and 0.10% (w/v) N,N'-methylenebisacrylamide (Sigma-Aldrich) in 1X PBS and aliquoted and stored it at –20°C. Next, we prepared gelling solution composed of monomer solution and the chemicals 4-hydroxy-2,2,6,6-tetramethylpiperidin-1-oxyl (4HT) (Sigma-Aldrich) as an inhibitor, and tetramethylethylenediamine (TEMED) (Sigma-Aldrich) as an accelerator, and ammonium persulfate (APS) (Sigma-Aldrich) was used as an initiator. We then sequentially added to the monomer solution, 4HT, TEMED, and finally APS to prepare the gelling solution (final concentration, 0.01% (w/w) for 4HT, and 0.2% (w/w) for both APS and TEMED). Then, we placed each coverslip containing a neuronal cell culture sample on a glass slide with the cells facing up, and constructed a gel chamber by putting three No. 1.5 coverslips on top of each other onto the glass slide to function as spacers on either end of the neuronal coverslip to avoid compression. The sample was then covered with gelling solution and a coverslip placed over the sample and across the two spacers to ensure the sample was covered with gelling solution and no air bubbles were formed on the sample. Samples were first incubated at 4°C for 30 minutes in a humidified atmosphere to prevent premature gelation and enable diffusion of solution into samples, and subsequently incubated at 37°C for 2.5 hours in a humidified atmosphere to complete gelation.

Afterward, the top coverslip was removed from the samples, and only the sample gel and original coverslip were removed and placed in a 50 mL large conical tube containing 5 mL of denaturation buffer, consisting of 20% (w/v) sodium dodecyl sulfate (SDS), 100 mM β-mercaptoethanol, 25 mM ethylenediaminetetraacetic acid (EDTA) and 0.5% Triton-X in Tris 50 mM at pH 8. Samples were incubated in denaturation buffer for 30 minutes at 37°C followed by 1 hour in an autoclave at 121°C. Samples were then cooled to RT for 30 minutes. At this stage, gels completely fell off the original coverslip during denaturation or immediately afterward following gentle shaking and washing with 1X PBS 5 times for 3 min each at RT. The hydrogel embedded samples attained a final state of ~2.3x linear expansion given the use of an expandable hydrogel. We observed that the fluorescence of SiRI reporters was completely quenched at this stage, so we could use fluorescent antibodies that had spectral overlap with SiRI reporters for immunostaining.

Next, samples underwent blocking by incubating for 30 minutes at 37°C in MAXBlock Blocking medium (Active Motif), followed by three washes for 5 minutes each at RT in MAXWash Washing medium (Active Motif). Next, samples were incubated with primary antibodies (see [Key Resources Table](#)) in MAXStain Staining medium (Active Motif) for 1.5 hours at 37°C or overnight at 4°C. This was followed by three washes for 5 minutes each at RT in MAXWash Washing medium. Then, samples were incubated with fluorescently-labeled secondary antibodies (see [Key Resources Table](#)) in MAXStain Staining medium for 1.5 hours at 37°C or overnight at 4°C. Samples were then washed three times for 5 minutes each at RT in MAXWash Washing medium and stored in 1X PBS until imaging.

For antibody stripping to enable spectral clearance, samples for [Figure 6I-Q](#) were placed in a water tight container with denaturation buffer and incubated for 2 hours at 70°C with shaking at 200 rpm. Then, the excess denaturation buffer was removed, and samples were washed with 1X PBS at RT 5 times for 3 minutes. Samples then underwent immunostaining steps as noted in the previous paragraph for the subsequent rounds of staining.

Immunostaining of Brain Slices

Brain slices were blocked overnight at 4°C in MAXBlock Blocking medium, followed by four washes for 30 minutes each at RT in MAXWash Washing medium. Next, slices were incubated with primary antibodies (see [Key Resources Table](#)) in MAXStain Staining medium at 1:100 for 3 days at 4°C, and then washed in MAXWash Washing medium four times for 30 minutes each at RT. The slices were then incubated in MAXWash Washing medium overnight at 4°C. Next, slices were incubated with fluorescently-labeled secondary antibodies (see [Key Resources Table](#)) in MAXStain Staining medium at 1:500 for 3 days at 4°C, and then washed in MAXWash Washing medium four times for 1 hour each at RT. The slices were then stored in 1X PBS at 4°C until imaging.

RNA Fluorescent *In Situ* Hybridization (RNA FISH)

Quasar 570 conjugated fluorescent oligonucleotides were purchased from LGC Biosearch Technologies as fluorescent RNA FISH probes (see [Key Resources Table](#)). Cells were washed twice for 5 minutes each with wash buffer A (10% formamide in 2X SSC). Afterward, fluorescent RNA FISH probes were added into the hybridization buffer [10% formamide (Millipore Sigma) and 10% dextran sulfate (Millipore Sigma) in 2X SSC] to a total probe concentration of 50 nM. tRNAs or other competitor tRNAs were not added in the hybridization buffer. Cells were incubated in the FISH probe-containing hybridization buffer for 16 hours at 37°C in a humidity controlled incubator. The cells were then washed with wash buffer A twice at 37°C, each for 30 minutes, before nuclear staining with DAPI at 1 µg/ml for 1-5 minutes followed by a 1X PBS wash. The cells were then transferred to 24-well glass plates with 1X PBS for imaging. Imaging was performed on the same wide-field Nikon Eclipse Ti microscope as the live HeLa imaging experiments.

QUANTIFICATION AND STATISTICAL ANALYSIS

Image Analysis

For each sample expressing the RNA scaffolds, the recorded field of view under the 40X objective was located by registration of the tiled image from the NucBlue channel (before fixation) and the tiled image from the DAPI channel (after immunostaining or RNA FISH), in each case taken under the 4X objective. The image and movie under the 40X objective taken from live cell imaging and the image under the 40X objective taken after immunostaining or RNA FISH were then registered by the NucBlue channel and the DAPI channel. For each sample expressing the protein scaffolds, the recorded field of view under the 40X objective was located by registration of the tiled image from the GFP channel before fixation and the tiled image from the GFP channel after immunostaining, in each case taken under the 4X objective. The image and movie under the 40X objective taken from live cell imaging and the image under the 40X objective taken after immunostaining were then registered by the GFP channels taken before fixation and after immunostaining.

The analysis of the recorded movies from live cell imaging was performed in ImageJ (ImageJ National Institutes of Health). For the analysis of the movies from cells expressing fluorescent reporters assembled by RNA scaffolds or protein scaffolds, the time course of the fluorescence intensity from a punctum in the recorded optical channel was measured as the time course of the average fluorescence intensity within the apparent boundary of the punctum. For the 65-minute-long recordings in acute mouse brain slice, motion correction for each punctum was performed by the StackReg and MultiStackReg plugins ([Thévenaz et al., 1998](#)) in ImageJ. Then the time course of the net fluorescence, F , from that punctum was obtained by subtracting the background fluorescence intensity measured from a region that had no cells in it from that movie. For the analysis of the movies from cells expressing non-assembled fluorescent reporters as control groups, the time course of the fluorescence intensity from a cell in the recorded optical channel was measured as the time course of the average fluorescence intensity within a random ROI in the cytosol of the cell with the area of that ROI similar to the size of individual puncta in the cells expressing assembled fluorescent reporters that these control groups were compared to, about 1 µm² in HeLa cells, 5-10 µm² in the somata of neurons, and 1 µm² in the neurites of neurons. This is for keeping the noise from the camera contained in the measured fluorescence time courses at a comparable level between cells expressing assembled fluorescent reporters and cells expressing non-assembled fluorescent reporters as control groups. Then the time course of the net fluorescence, F , from that cell was obtained by subtracting the background fluorescent intensity measured from a region that had no cells in it from that movie. For each neurite-localized ROI in neurons, we calculated the cumulative distance between the ROI and the soma by measuring along the neurite. For the CA1 pyramidal neurons recorded from acute mouse brain slice, apical dendrites and basal dendrites were identified by cell morphology. For ExRaiAKAR or ExRaiCKAR, the time courses of the fluorescence intensity in the GFP emission channel under 488 nm and 405 nm excitations were measured as F_{488} and F_{405} , respectively.

We observed significant photobleaching in the fluorescence time courses measured from cAMP_r and RAB_EKAR_{rev} in recordings longer than 5 minutes in cultured neurons, as well as those measured from GCaMP6f and ExRaiAKAR in the 65-minute-long recordings in slice. Photobleaching correction was performed on these fluorescence time courses as described below. Baseline fluorescence time courses during the pre-stimulation periods measured from cAMP_r or RAB_EKAR_{rev} were fitted to exponential decay functions, and the exponential decay components were then removed from the full-length time courses. Baseline fluorescence time courses during the pre-stimulation periods measured from GCaMP6f in the 65-minute-long recordings in slice were fitted to

a bi-exponential decay function, and the bi-exponential decay components were then removed from the full-length time courses. Baseline fluorescence time courses during the pre-stimulation periods measured from ExRaiAKAR in the 65-minute-long recordings in slice under 488 nm excitation, i.e., $F_{488_baseline}$, were fitted to a bi-exponential decay function, and the bi-exponential decay components were then removed from the full-length time courses. Baseline fluorescence time courses during the pre-stimulation periods measured from ExRaiAKAR in slice under 405 nm excitation, i.e., $F_{405_baseline}$, were fitted to a bi-exponential decay function with the time constants fixed to those obtained from the curve fitting of the corresponding $F_{488_baseline}$ time courses (so that the resultant time constants from the bi-exponential fitting were identical between each $F_{488_baseline}/F_{405_baseline}$ pair), and the resulted bi-exponential decay components were then removed from the full-length time courses.

To calculate the dF/F_0 for GCaMP6f, cAMPr, or RAB_EKARev expressing HeLa cells or neurons, we first calculated the baseline fluorescence, F_0 , as the average net fluorescence during the pre-stimulation baseline period. dF/F_0 was then calculated as $dF/F_0 = (F - F_0) / F_0$. To calculate the signal-to-noise ratio (SNR) we divided the maximum dF/F_0 by the standard deviation of the net fluorescence during the pre-stimulation baseline period.

To calculate the dR/R_0 for ExRaiAKAR or ExRaiCKAR expressing HeLa cells or neurons, we first calculated the baseline fluorescence, F_{0_488} and F_{0_405} , as the average net fluorescence during the pre-stimulation baseline period in the GFP emission channel under 488 nm and 405 nm excitations, respectively. dR/R_0 was then calculated as $dR/R_0 = (F_{488} / F_{405}) / (F_{0_488} / F_{0_405}) - 1$. To calculate the signal-to-noise ratio (SNR) we divided the maximum dF/F_0 by the standard deviation of the net fluorescence during the pre-stimulation baseline period.

To calculate the change of CFP/YFP ratio, $d(C/Y)/(C/Y)$, for ICUE3 expressing HeLa cells, we first calculated the CFP/YFP ratio, C/Y , by dividing the net fluorescence from the CFP channel by the net fluorescence from the YFP channel. Then the baseline of the CFP/YFP ratio, $(C/Y)_0$, was calculated as the average of the CFP/YFP ratio during the 2-minute period right before adding the extracellular stimulation. $d(C/Y)/(C/Y)$ was then calculated as $d(C/Y)/(C/Y) = [C/Y - (C/Y)_0] / (C/Y)_0$. To calculate the signal-to-noise ratio (SNR) we divided the maximum $d(C/Y)/(C/Y)$ by the standard deviation of the $d(C/Y)/(C/Y)$ during the pre-stimulation baseline period.

Half rise time was calculated as the duration between the onset of stimulation and the time when dF/F_0 (or dR/R_0) increased to half of the peak value. Half decay time was calculated as the duration between the time when dF/F_0 was at the peak value and the time when dF/F_0 decreased to half of the peak value.

For puncta size analysis and the distance to the nearest punctum analysis, StarDist (Schmidt et al., 2018; Weigert et al., 2019) was used to identify and segment the boundaries of puncta followed by geometrical analysis with a custom MATLAB script. For the analysis of puncta spatial separation, a punctum with less than 5% overlap with the puncta of other sensors after immunostaining was counted as a spatially separate punctum. For the analysis of the motion of puncta in time-lapse movies (1 minute per frame; 1 hour total), puncta were automatically identified and tracked by the TrackMate plugin (Tinevez et al., 2017) in ImageJ. Then mean squared displacement (MSD) and diffusion coefficient were calculated in MATLAB (Mathworks) with the script msdanalyzer (Tarantino et al., 2014) based on the tracking results from TrackMate.

Statistical analysis:

All statistical analysis was performed using the built-in statistical analysis tools in Prism (GraphPad), JMP (SAS), or MATLAB. The statistical details of each statistical analysis can be found in the figure legends and Table S4.

Supplemental Figures

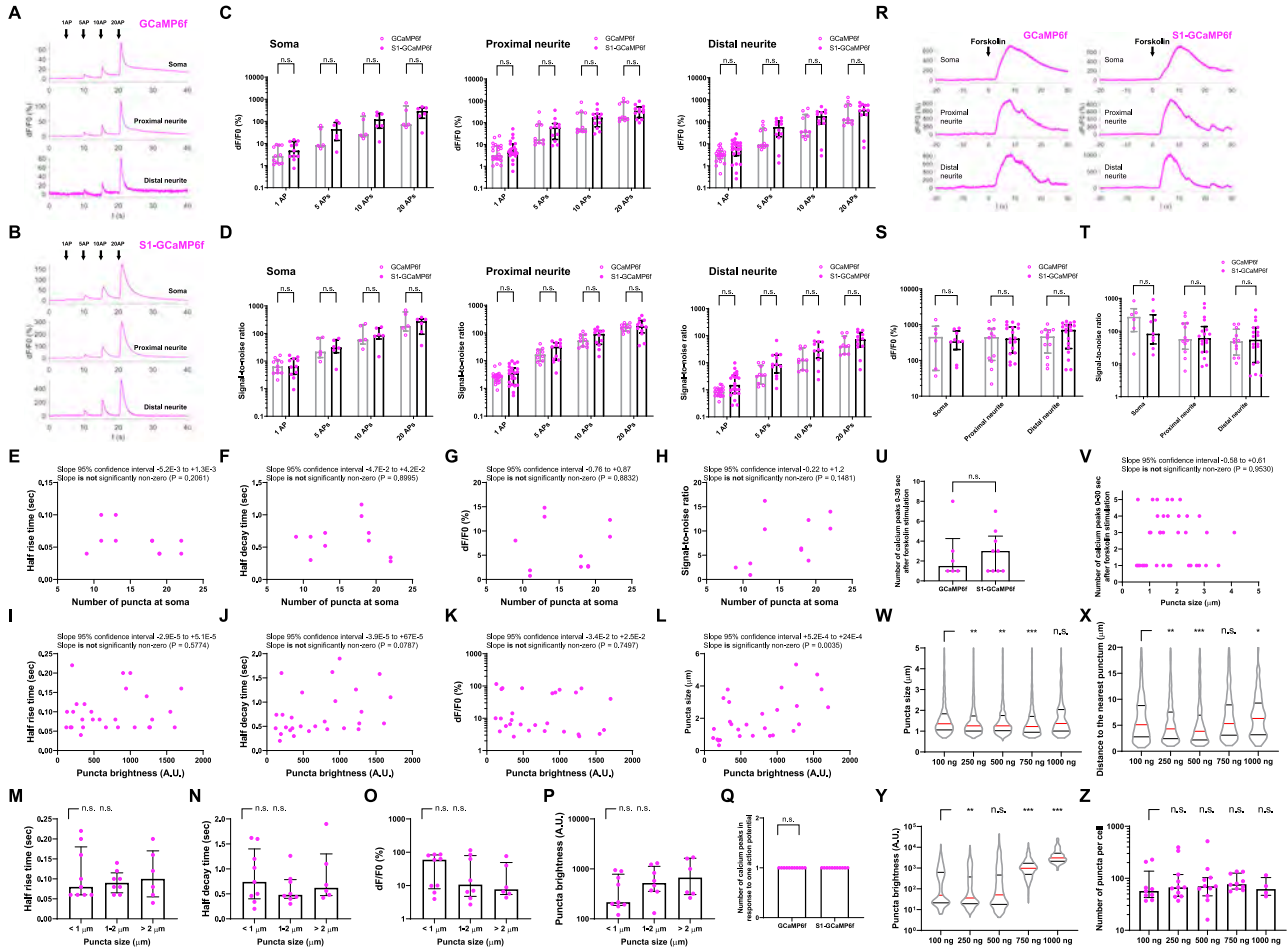
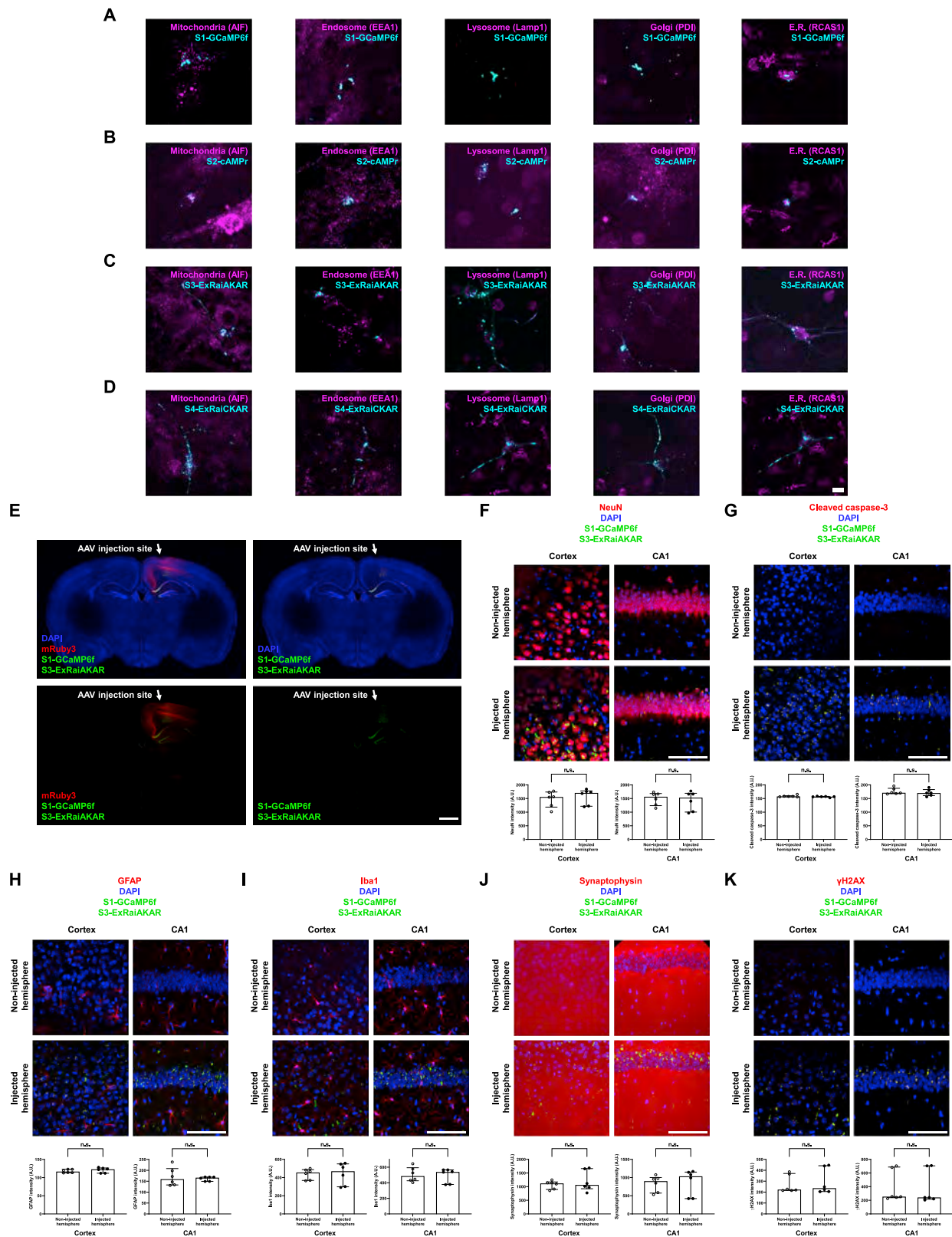


Figure S1. Further Characterization of S1-GCaMP6f, Related to Figure 2

(A-B) Representative fluorescent signals recorded from the soma, proximal neurites (5–25 μm away from soma throughout this figure), and distal neurites (50–250 μm away from soma throughout this figure) of a cultured mouse hippocampal neuron expressing GCaMP6f (A) or S1-GCaMP6f (B) in response to a single action potential (1AP), 5 action potentials (5AP), 10 action potentials (10AP), and 20 action potentials (20AP) triggered by current injection via whole-cell patch clamp at the soma. dF/F0, fluorescence change in the GFP channel. Each fluorescent signal for S1-GCaMP6f was measured from a single punctum. (C) Bar plots of the peak fluorescence changes in the GFP channel at the soma, proximal neurites, and distal neurites of cultured mouse hippocampal neurons expressing GCaMP6f or S1-GCaMP6f in response to a single ($n = 11$ values from soma, 22 values from proximal neurites, and 22 values from distal neurites from 11 total trials from 6 neurons from 3 cultures for each of GCaMP6f and S1-GCaMP6f; for each trial, the calcium responses from the soma and two proximal neurites and two distal neurites were analyzed) or multiple (5AP, 10AP, or 20AP; $n = 5$ values from soma, 10 values from proximal neurites, and 10 values from distal neurites from 5 total trials from 5 neurons from 3 cultures for GCaMP6f; $n = 6$ values from soma, 12 values from proximal neurites, and 12 values from distal neurites from 6 total trials from 6 neurons from 3 cultures for S1-GCaMP6f; for each trial, the calcium responses from the soma and two proximal neurites and two distal neurites were analyzed) action potentials. Bar plots of medians with interquartile ranges are used throughout this figure, with individual values plotted as dots. n.s., not significant; two-way analysis of variance followed by post hoc Bonferroni corrected multiple comparisons test; see Table S4 for full statistics for Figure S1. (D) Bar plots of the signal-to-noise ratio in the GFP channel at the soma, proximal neurites, and distal neurites for the neurons of (C). (E-H) Scatterplots of half rise time (E), half decay time (F), peak fluorescence change (G), and signal-to-noise ratio (H) versus the number of puncta at the soma, per cell, for the recorded somatic calcium transients in response to a single action potential in S1-GCaMP6f expressing neurons ($n = 6$ neurons from 3 cultures). (I-L) Scatterplots of half rise time (I), half decay time (J), peak fluorescence change (K), and punctum size (L) versus punctum brightness for the recorded somatic calcium transients in response to a single action potential in S1-GCaMP6f expressing neurons ($n = 6$ neurons from 3 cultures). (M-P) Bar plots of half rise time (M), half decay time (N), peak fluorescence change (O), and punctum brightness (P) versus somatic punctum size for the recorded somatic calcium transients in response to a single action potential in S1-GCaMP6f expressing neurons ($n = 6$ neurons from 3 cultures). n.s., not significant; Kruskal-Wallis analysis of variance followed by post hoc test via Dunn's test with ' $< 1 \mu\text{m}$ ' as control group. (Q) Bar plot of the number of somatic calcium peaks in response to a single action potential for GCaMP6f and S1-GCaMP6f expressing neurons of (C). n.s., not significant; Wilcoxon rank sum test. (R) Representative fluorescent signals recorded from the soma, proximal neurites, and distal of a cultured mouse hippocampal neuron expressing GCaMP6f and a neuron expressing S1-GCaMP6f, with 5 μM forskolin stimulation at

(legend continued on next page)

$t = 10$ s. dF/F_0 , fluorescence changes in GFP channel. Each fluorescent signal for S1-GCaMP6f was measured from a single punctum. **(S)** Bar plot of the peak fluorescence changes in the GFP channel at the soma, proximal neurites, and distal neurites of cultured mouse hippocampal neurons expressing GCaMP6f or S1-GCaMP6f under 5 μ M forskolin stimulation ($n = 6$ somata, 12 proximal neurites, and 12 distal neurites from 6 neurons from 4 cultures for GCaMP6f; $n = 9$ somata, 18 proximal neurites, and 18 distal neurites from 9 neurons from 9 cultures for S1-GCaMP6f). n.s., not significant; two-way analysis of variance followed by post hoc Bonferroni corrected multiple comparisons test. **(T)** Bar plot of the signal-to-noise ratio in the GFP channel at the soma, proximal neurites, and distal neurites for the neurons of **(S)**. **(U)** Bar plot of the number of somatic calcium peaks 0-30 s after forskolin stimulation for the neurons of **(S)**. **(V)** Scatterplot of the number of S1-GCaMP6f reported somatic calcium spikes 0-30 s after forskolin stimulation versus somatic punctum size in S1-GCaMP6f expressing neurons ($n = 5$ neurons from 5 cultures). **(W-Z)** Violin plots of the puncta size **(W)**, distance to the nearest punctum **(X)**, and puncta brightness **(Y)**, and bar plot of number of puncta per cell **(Z)**, for S1-GCaMP6f in neurons ($n = 792, 1314, 1230, 881,$ and 283 puncta in 9, 11, 11, 10, and 4 neurons from 1, 1, 1, 1, and 1 culture for 100 ng, 250 ng, 500 ng, 750 ng, and 1000 ng, respectively). Red line, median; black line, interquartile ranges; 100 ng, 250 ng, 500 ng, 750 ng, and 1000 ng, the mass of DNA of the SiRI construct used in calcium phosphate transfection per well in 24-well plates, with extra pUC19 dummy DNA added so that the total transfected DNA per well was 1500 ng; Dc was measured in live neurons 4 days after transfection on DIV 9; n.s., not significant; * $p < 0.05$; ** $p < 0.01$; *** $p < 0.001$; Kruskal-Wallis analysis of variance followed by post hoc test via Dunn's test with '100 ng' as control group.



(legend on next page)

Figure S2. Immunostaining of Cellular Organelles in Cultured Mouse Neurons Expressing SiRIs and Immunohistochemical Characterization of Cellular and Synaptic State Markers in Mouse Brains Expressing SiRIs, Related to Figures 2, 4, and 6

Representative confocal images of cultured mouse hippocampal neurons expressing (A) S1-GCaMP6f (anti-AIF staining, n = 5 neurons from 2 cultures; anti-EEA1 staining, n = 5 neurons from 2 cultures; anti-Lamp1 staining, n = 5 neurons from 2 cultures; anti-PDI staining, n = 4 neurons from 2 cultures; anti-RCAS1 staining, n = 4 neurons from 2 cultures), (B) S2-cAMP_r (anti-AIF staining, n = 4 neurons from 1 culture; anti-EEA1 staining, n = 6 neurons from 1 culture; anti-Lamp1 staining, n = 2 neurons from 1 culture; anti-PDI staining, n = 2 neurons from 1 culture; anti-RCAS1 staining, n = 4 neurons from 1 culture), (C) S3-ExRaiAKAR (anti-AIF staining, n = 6 neurons from 1 culture; anti-EEA1 staining, n = 5 neurons from 1 culture; anti-Lamp1 staining, n = 2 neurons from 1 culture; anti-PDI staining, n = 5 neurons from 1 culture; anti-RCAS1 staining, n = 5 neurons from 1 culture), or (D) S4-ExRaiCKAR (anti-AIF staining, n = 4 neurons from 1 culture; anti-EEA1 staining, n = 4 neurons from 1 culture; anti-Lamp1 staining, n = 6 neurons from 1 culture; anti-PDI staining, n = 4 neurons from 1 culture; anti-RCAS1 staining, n = 5 neurons from 1 culture). Cells were immunostained against mitochondria (via anti-AIF), endosomes (via anti-EEA1), lysosomes (via anti-Lamp1), Golgi apparatus (via anti-PDI), or endoplasmic reticulum (ER; via anti-RCAS1). SiRI puncta in the GFP channel were colored cyan and immunostaining signals were colored magenta. Scale bar, 10 μ m. (E) Representative confocal images of brain slices from 5-7 week old mice expressing S1-GCaMP6f, S3-ExRaiAKAR, and mRuby3-6xFLAG in the right cerebral hemisphere following AAV injection. Swiss Webster mice were injected with a mixture of three AAVs (AAV-DJ-UBC-S1-GCaMP6f, AAV-2/9-UBC-S3-ExRaiAKAR, and AAV-2/9-hSyn-mRuby3-6xFLAG; Janelia Viral Tools Facility) in both the visual cortex and the hippocampus of the right cerebral hemisphere. When the mice reached the age of 5-7 weeks old, they were euthanized, perfused with 4% PFA, and brains were sliced coronally at 100 μ m in 1X PBS, and stained with antibodies against one of the cellular and synaptic markers below (see F-K) together with DAPI to label nuclei. Staining intensities of cellular and synaptic markers in the cortex (or CA1) were imaged volumetrically using a 40x objective on a spinning disk confocal microscope, with identical imaging conditions, measured in ImageJ as the averaged fluorescent intensities of the fluorescent secondary antibodies over imaged fields of view (185 μ m \times 185 μ m \times 50 μ m for each fields of view), and compared between the injected hemisphere and the non-injected hemisphere. Scale bar, 1 mm. (F-K, top) Representative confocal images of cortex and CA1 in the injected hemisphere and non-injected hemisphere in the brain slices stained with antibodies against each of the cellular and synaptic markers indicated, and DAPI. Scale bars, 100 μ m. (F-K, bottom) Bar plots of the staining intensities for each of the cellular and synaptic markers between the injected hemisphere and the non-injected hemisphere; for each marker, n = 6 fields of view from 3 mice in the cortex (or in CA1) in the injected hemisphere (or non-injected hemisphere). Bar plots are medians with interquartile ranges, with individual values in arbitrary units (A.U.) plotted as circles and dots. (F) NeuN (neuronal nuclei marker). (G) Cleaved caspase-3 (apoptotic marker). (H) GFAP (astrocyte marker). (I) Iba1 (microglial marker). (J) Synaptophysin (a synaptic protein marker). (K) γ H2AX (DNA damage marker). n.s., not significant; Wilcoxon rank sum test; see Table S4 for full statistics for Figure S2.

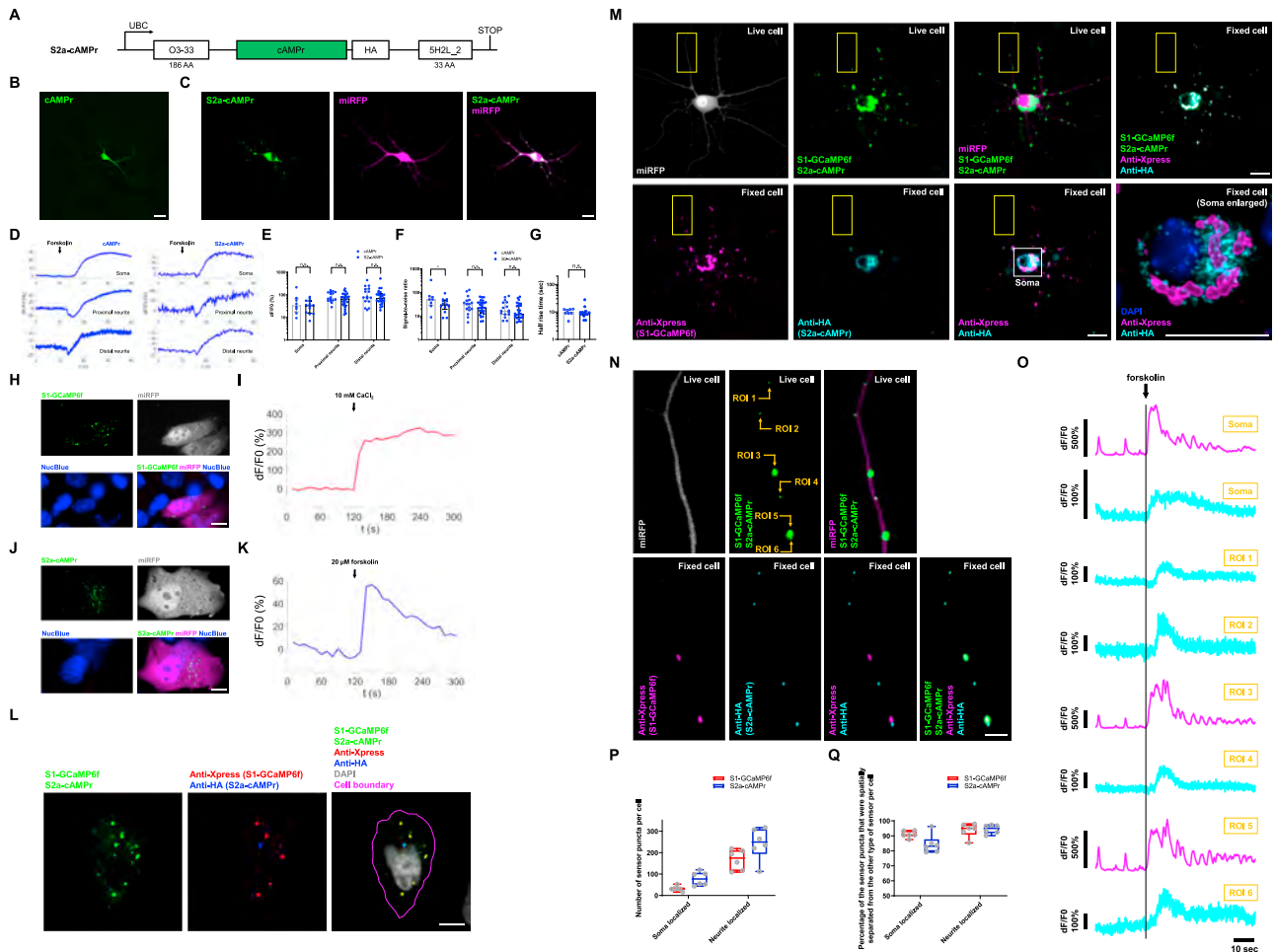


Figure S3. Design of S2a-cAMPr and Utilization for Multiplexed SiRI Imaging, Related to Figure 2

(A) Construct design of S2a-cAMPr. O3-33, self-assembling subunit of O3-33 octahedron (24-mer); HA, influenza hemagglutinin epitope; 5H2L_2, a homopentamer; AA, amino acid (see Table S1 for sequences of the motifs; see Table S2 for all tested constructs). (B) A representative confocal image of a live cultured mouse hippocampal neuron expressing cAMPr. Scale bar, 20 μm . (C) Representative confocal images of a live cultured mouse hippocampal neuron expressing S2a-cAMPr and miRFP as a cell morphology marker. Scale bar, 20 μm . (D) Representative fluorescent signals recorded from the soma, proximal neurites (5–25 μm away from soma), and distal neurites (50–250 μm away from soma) of cultured mouse hippocampal neurons expressing cAMPr or S2a-cAMPr with 5 μM forskolin stimulation at $t = 10$ s. dF/F0, fluorescence changes in GFP channel. Each fluorescent signal for S2a-cAMPr was measured from a single punctum. (E) Bar plot of the peak fluorescence changes in GFP channel at the soma, proximal neurites (5–25 μm away from soma), and distal neurites (50–250 μm away from soma) of cultured mouse hippocampal neurons expressing cAMPr or S2a-cAMPr after 5 μM forskolin stimulation ($n = 8$ somata, 16 proximal neurites, and 16 distal neurites from 8 neurons from 5 cultures for cAMPr; $n = 13$ somata, 26 proximal neurites, and 26 distal neurites from 13 neurons from 9 cultures for S2a-cAMPr). Bar plots of medians with interquartile ranges are used throughout this figure, with individual values plotted as dots. n.s., not significant; two-way analysis of variance followed by post hoc Sidak’s multiple comparisons test; see Table S4 for full statistics for Figure S3. (F) Signal-to-noise ratio in the GFP channel at the soma, proximal neurites, and distal neurites for the neurons of (E). n.s., not significant. (G) Half rise time of reported cAMP signals at the soma, for the neurons of (E). n.s., not significant. (H) A representative confocal image of live HeLa cells expressing S1-GCaMP6f, as well as the morphological marker miRFP, and stained with a live cell nuclear stain, NucBlue. Scale bars, 10 μm throughout this figure. (I) Representative fluorescent signal recorded during live cell imaging from the HeLa cell in (H) under 10 mM CaCl_2 stimulation at $t = 120$ s. Throughout this figure: dF/F0, fluorescence changes in the GFP channel. (J) A representative confocal image of a live HeLa cell expressing S2a-cAMPr, as well as the morphological marker miRFP, and stained with NucBlue. (K) Representative fluorescent signal recorded during live cell imaging from the HeLa cell in (J) under 20 μM forskolin stimulation at $t = 120$ s. (L) Representative images of HeLa cells co-expressing S1-GCaMP6f and S2a-cAMPr. All images in (L) were taken after fixation, immunostaining against the Xpress epitope and HA epitope, and DAPI staining against the cell nucleus. (M) Representative confocal images of live cultured mouse hippocampal neurons co-expressing S1-GCaMP6f, S2a-cAMPr, and the morphological marker miRFP (first three panels in the top row) and after fixation, immunostaining (with anti-Xpress to mark GCaMP6f and anti-HA to mark cAMPr), and DAPI staining to mark the cell nucleus (the remaining five panels). Yellow rectangle, boundary of the region shown in enlarged view in (N). White square, boundary of the soma region shown in the enlarged view in the right most panel in the bottom row. All scale bars, 20 μm . (N) Enlarged views of the neurite region in the yellow rectangle in (M). Arrows indicate the regions-of-interest (ROIs) of individual puncta whose fluorescent signal time courses are plotted in (O). Scale bar, 5 μm . (O) Recorded fluorescent signals at the soma and the ROIs along the neurite marked in N during live cell imaging with 5 μM forskolin stimulation. (P) Boxplot of the number of soma-localized or neurite-localized S1-GCaMP6f or S2a-cAMPr puncta per cell identified by immunostaining in neurons co-expressing S1-GCaMP6f, S2a-cAMPr, and miRFP ($n = 6$ neurons from 6 cultures). Boxplots throughout this figure: middle horizontal line, median; top and bottom

(legend continued on next page)

horizontal lines, 25% and 75% percentiles; top and bottom whiskers, minimum and maximum values; hollow circles, individual values. (Q) Boxplot of the percentage of the soma-localized or neurite-localized fluorescent reporter puncta that did not contain the other type of reporter, per cell, as identified by immunostaining in neurons co-expressing S1-GCaMP6f, S2a-cAMP_r, and miRFP (n = 6 neurons from 6 cultures).

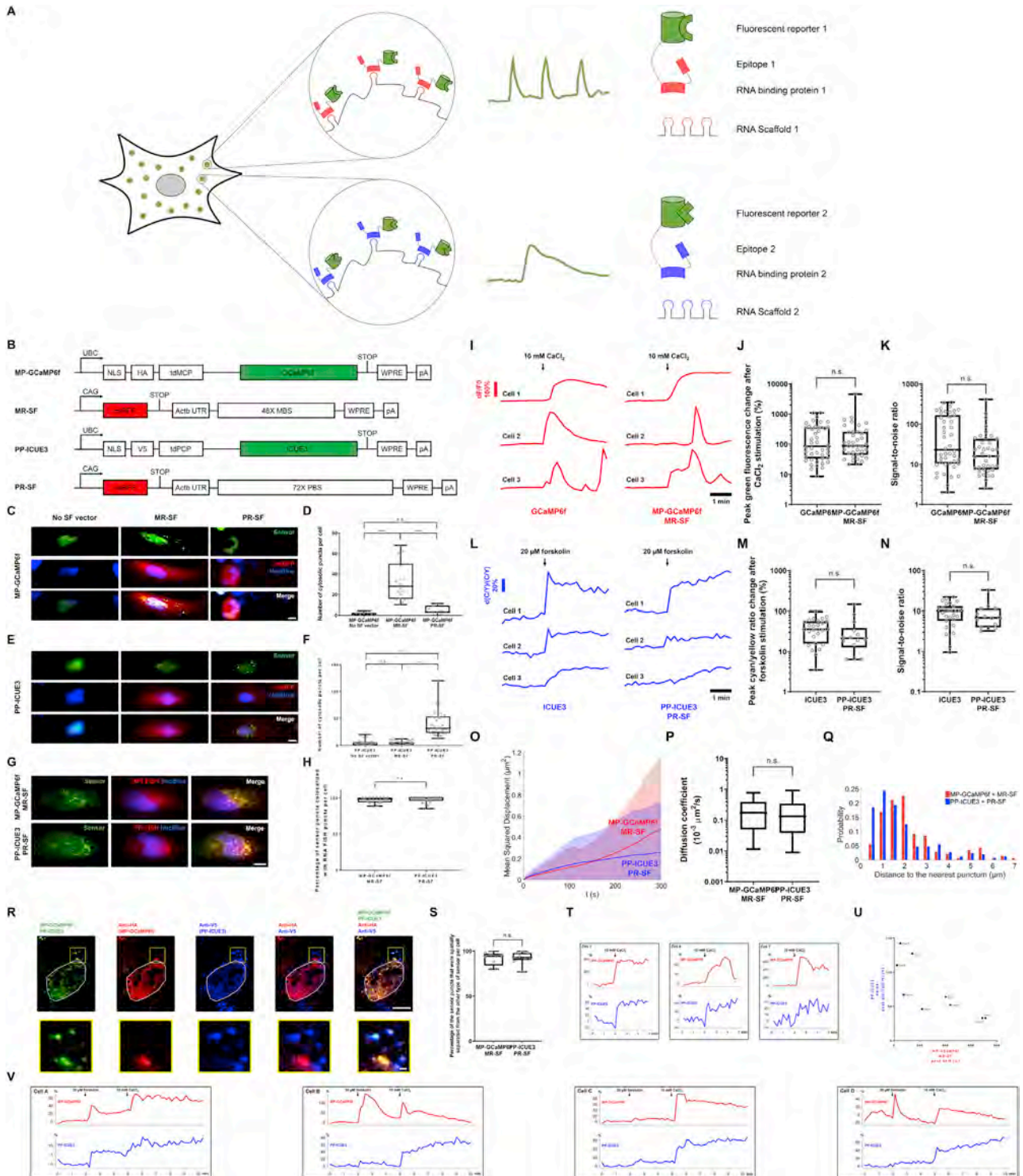


Figure S4. Design of RNA Scaffold-Based SiRI Reporters and Utilization for Simultaneous Recording of Ca²⁺ and cAMP Activities in Mammalian Cells, Related to Figure 2

(A) Schematic of how fluorescent reporter clustering could be achieved by assembling different fluorescent reporters onto distinct RNA scaffolds (“RNA SiRIs”); post hoc multiplexed RNA fluorescent *in situ* hybridization (FISH) allows reporter identification. (B) Construct designs of the reporter vectors (MS2 protein with GCaMP6f, or MP-GCaMP6f; PP7 protein with a CFP/YFP FRET-based fluorescent cAMP reporter ICUE3, or PP-ICUE3) and the scaffold vectors (MS2 RNA scaffold, MR-SF; PP7 RNA scaffold, PR-SF). UBC, ubiquitin C promoter; CAG, CMV early enhancer/chicken β actin promoter; NLS, SV40 nuclear localization

(legend continued on next page)

sequence; HA, influenza hemagglutinin epitope; V5, simian virus 5-derived epitope; tdMCP, tandem dimer MS2 coat protein; tdPCP, tandem dimer PP7 coat protein; MBS, MS2 binding site; PBS, PP7 binding site; Actb UTR, 3' untranslated region of mouse β actin mRNA (nucleotides 1-441); STOP, stop codon; WPRE, woodchuck hepatitis virus posttranscriptional regulatory element; pA, poly(A) tail (see [Table S1](#) for sequences of the motifs; see [Table S2](#) for all tested constructs).

(C) Representative images of live HeLa cells transfected with MP-GCaMP6f transfected alone (left), with MR-SF (middle), or with PR-SF (right). Scale bars, 10 μ m throughout this figure. **(D)** Boxplot of the number of cytosolic fluorescent puncta per cell from the transfected HeLa cells described in **(C)** ($n = 9$ cells from 3 cultures for MP-GCaMP6f only; $n = 18$ cells from 9 cultures for MP-GCaMP6f + MR-SF; $n = 11$ cells from 5 cultures for MP-GCaMP6f + PR-SF). *** $p < 0.001$; n.s., not significant; Kruskal-Wallis analysis of variance followed by post hoc Dunn's multiple comparison test; see [Table S4](#) for full statistics for [Figure S4](#); boxplots throughout this figure: middle horizontal line, median; top and bottom horizontal lines, 25% and 75% percentiles; top and bottom whiskers, unless specifically noted in caption, minimum and maximum values; hollow circles, individual values. **(E)** Representative images of live HeLa cells transfected with PP-ICUE3 alone (left), with MR-SF (middle), or PR-SF (right). **(F)** Boxplot of the number of cytosolic fluorescent puncta per cell from the transfected HeLa cells described in **(E)** ($n = 28$ cells from 5 cultures for PP-ICUE3 only; $n = 35$ cells from 5 cultures for PP-ICUE3 + MR-SF; $n = 38$ cells from 11 cultures for PP-ICUE3 + PR-SF). *** $p < 0.001$; n.s., not significant; Kruskal-Wallis analysis of variance followed by post hoc Dunn's multiple comparison test. **(G)** Representative images of fixed HeLa cells co-transfected with MP-GCaMP6f and MR-SF or PP-GCaMP6f and PR-SF after RNA FISH against the expressed mRNA from MR-SF ("MR FISH") or PR-SF ("PR FISH"). **(H)** Boxplot of the percentage of fluorescent reporter puncta that also bear RNA FISH puncta per cell ($n = 19$ cells from 4 cultures for MP-GCaMP6f and MR-SF; $n = 22$ cells from 5 cultures for PP-ICUE3 and PR-SF). n.s., not significant; Wilcoxon rank sum test. **(I)** Representative fluorescent signals recorded during live cell imaging from 3 HeLa cells expressing GCaMP6f (left) and from 3 fluorescent reporter puncta from 3 different HeLa cells expressing MP-GCaMP6f and MR-SF (right), after 10 mM CaCl_2 stimulation. dF/F_0 , fluorescence changes in the GFP channel. **(J)** Boxplot of the peak fluorescence changes from the HeLa cells described in **I** under 10 mM CaCl_2 stimulation ($n = 44$ cells from 2 cultures for GCaMP6f; $n = 39$ cells from 5 cultures for MP-GCaMP6f and MR-SF). n.s., not significant; Wilcoxon rank sum test. **(K)** Boxplot of the signal-to-noise ratio (with noise defined as the standard deviation of the baseline pre-stimulus throughout this paper) from the HeLa cells described in **I** under 10 mM CaCl_2 stimulation ($n = 44$ cells from 2 cultures for GCaMP6f; $n = 39$ cells from 5 cultures for MP-GCaMP6f and MR-SF). n.s., not significant; Wilcoxon rank sum test. **(L)** Representative fluorescent signals recorded during live cell imaging from 3 HeLa cells expressing ICUE3 (left) and from 3 fluorescent reporter puncta from 3 different HeLa cells expressing PP-ICUE3 and PR-SF (right), after 20 μ M forskolin stimulation. $d(C/Y)/(C/Y)$, change of the fluorescence ratio between CFP channel and YFP channel. **(M)** Boxplot of the peak fluorescence changes from the transfected HeLa cells described in **L** under 20 μ M forskolin stimulation ($n = 27$ cells from 3 cultures for ICUE3; $n = 14$ cells from 7 cultures for PP-ICUE3 and PR-SF). n.s., not significant; Wilcoxon rank sum test. **(N)** Boxplot of the signal-to-noise ratio from the HeLa cells described in **L** under 20 μ M forskolin stimulation ($n = 27$ cells from 3 cultures for ICUE3; $n = 14$ cells from 7 cultures for PP-ICUE3 and PR-SF). n.s., not significant; Wilcoxon rank sum test. **(O)** Mean squared displacement of the fluorescent reporter puncta locations in live HeLa cells expressing MP-GCaMP6f and MR-SF (red) or PP-ICUE3 and PR-SF (blue) versus time ($n = 314$ puncta from 14 cells from 6 cultures for MP-GCaMP6f and MR-SF; $n = 678$ puncta from 14 cells from 7 cultures for PP-ICUE3 and PR-SF). Red and blue lines, mean; red and blue shaded boundaries, standard deviation. **(P)** Boxplot of the diffusion coefficients of the fluorescent reporter puncta in **(O)**. n.s., not significant; Wilcoxon rank sum test. In this specific boxplot, top and bottom whiskers represent 10% and 90% percentiles; individual values are not shown. **(Q)** Histogram of the distances between one puncta and its nearest-neighbor punctum in HeLa cells expressing MP-GCaMP6f and MR-SF or PP-ICUE3 and PR-SF ($n = 142$ puncta from 5 cells from 5 cultures for MP-GCaMP6f and MR-SF; $n = 254$ puncta from 5 cells from 5 cultures for PP-ICUE3 and PR-SF). **(R)** Representative epifluorescent images (top row) of HeLa cells quadruply transfected with MP-GCaMP6f, MR-SF, PP-ICUE3, and PR-SF (MP-GCaMP6f, PP-ICUE3 shown in green), and then fixed and immunostained against HA epitope (anti-HA, red) and V5 epitope (anti-V5, blue); White line, boundary of the cell nucleus; scale bar, 10 μ m. Enlarged images of the regions highlighted by yellow boxes in the top row are shown in the bottom row; scale bar, 1 μ m. **(S)** Boxplot of the percentage of the puncta of the indicated reporter that did not contain the other type of reporter, per cell, as identified by dual immunostaining ($n = 9$ cells from 5 cultures, each; n.s., not significant; Wilcoxon rank sum test). **(T)** Representative fluorescent signals recorded from live HeLa cells co-transfected with MP-GCaMP6f, MR-SF, PP-ICUE3, and PR-SF after 10 mM CaCl_2 stimulation at $t = 2$ min ($n = 9$ cells from 7 cultures). Red traces, dF/F_0 (%) of a single punctum in the cell that was identified as clustered GCaMP6f by post hoc immunostaining; blue traces, change of the CFP/YFP fluorescence ratio, $d(C/Y)/(C/Y)$ (%), of a punctum in the cell that was identified as clustered ICUE3 by post hoc immunostaining. **(U)** Scatterplot of the peak fluorescent responses of the cells in **(T)** after 10 mM CaCl_2 stimulation ($n = 9$ cells from 7 cultures). **(V)** Fluorescent signals recorded from live HeLa cells co-transfected with MP-GCaMP6f, MR-SF, PP-ICUE3, and PR-SF under 20 μ M forskolin stimulation at $t = 2$ min and then 10 mM CaCl_2 stimulation at $t = 5$ min ($n = 4$ cells from 2 cultures). Red traces, dF/F_0 (%) of a punctum in the cell that was identified as assembled GCaMP6f by post hoc immunostaining; blue traces, $d(C/Y)/(C/Y)$ (%) of a punctum in the cell that was identified as assembled ICUE3 by post hoc immunostaining.

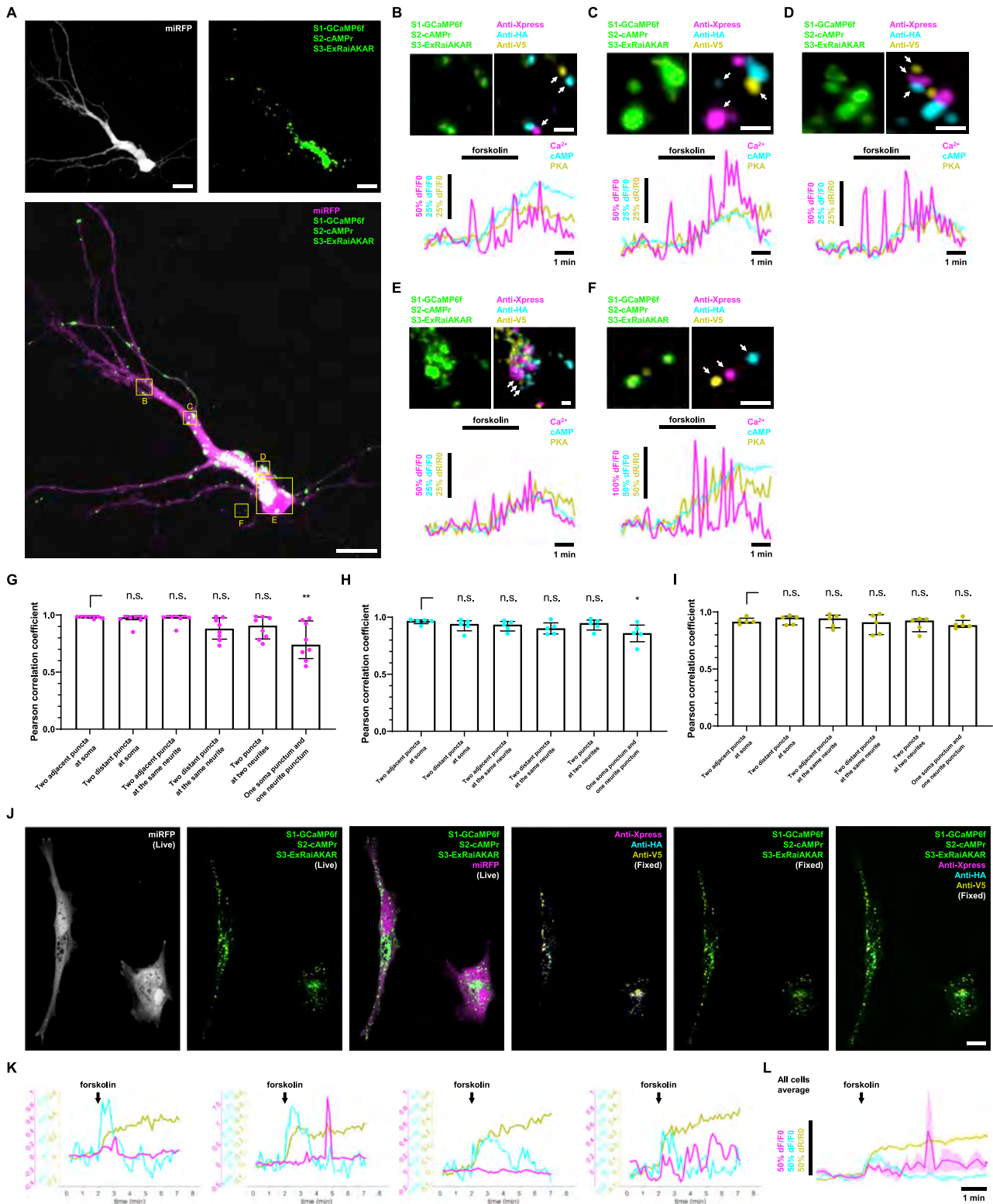


Figure S5. Spatially Multiplexed Imaging of Three GFP-Based Reporters for Calcium, cAMP, and PKA Activities at Different Subcellular Locations in Single Mouse Neuron and in a Human Cell Line, Related to Figure 3

(A) Maximum intensity projection (MIP) confocal images of the live cultured mouse hippocampal neuron co-expressing S1-GCaMP6f, S2-cAMPPr, S3-ExRaiAKAR, and miRFP shown in Figure 3A. Upper left panel, under miRFP channel; upper right panel, under GFP channel; bottom panel, a composite image from

(legend continued on next page)

GFP and miRFP channels. Orange squares, boundaries of the regions to be shown in enlarged views in (B)-(F). Scale bars, 20 μm . (B-F) Top left, an enlarged view of the corresponding region marked in (A) (by the corresponding letter) under green channel. Top right, an MIP confocal image of the same region after fixation and immunostaining against Xpress (magenta), HA (cyan), and V5 (yellow). Bottom, recorded Ca^{2+} (magenta), cAMP (cyan), and PKA (yellow) activities measured from puncta indicated by white arrowheads in the top right view during live cell imaging under 50 μM forskolin stimulation for 3 minutes. Scale bars, 2 μm . Note that (E) and (C) in this figure are identical to Figure 3B and Figure 3C, respectively. (G-I) Bar plots of Pearson correlation coefficients of the Ca^{2+} (G); $n = 8$ neurons from 8 cultures), cAMP (H); $n = 5$ neurons from 5 cultures), or PKA (I); $n = 5$ neurons from 5 cultures) responses recorded from soma- and neurite- localized puncta within single cultured mouse hippocampal neurons co-expressing S1-GCaMP6f, S2-cAMPPr, S3-ExRaiAKAR, and miRFP. Two puncta at the soma (or along a neurite) were defined to be adjacent if they were less than 5 μm apart, and as distant if they were at least 10 μm apart at the soma (or at least 20 μm apart along a neurite). Neurite-localized puncta in this analysis were 20-60 μm away from the soma. Bar plots of medians with interquartile ranges are used, with individual values plotted as dots. n.s., not significant; * $p < 0.05$; ** $p < 0.01$; Kruskal-Wallis analysis of variance followed by post hoc Dunn's multiple comparisons test with 'two adjacent puncta at soma' as control group; see Table S4 for full statistics for Figure S5. (J) Maximum intensity projection (MIP) confocal images of HeLa cells co-expressing S1-GCaMP6f, S2-cAMPPr, S3-ExRaiAKAR, and the cell morphological marker, miRFP. Live, images taken from live cell imaging; Fixed, images taken after fixation and immunostaining against Xpress (magenta), HA (cyan), and V5 (yellow). Scale bar, 20 μm . (K) Recorded fluorescent signals of Ca^{2+} (magenta), cAMP (cyan), and PKA (yellow) activities of individual HeLa cells under forskolin stimulation by pipetting 100 μL of 100 μM forskolin in FluoroBrite DMEM dropwise onto a HeLa cell culture in 1.9 mL FluoroBrite DMEM (for a 5 μM final concentration of forskolin applied to the HeLa cell culture) at $t = 2$ min ($n = 4$ cells co-expressing S1-GCaMP6f, S2-cAMPPr, S3-ExRaiAKAR, and miRFP from 2 cultures). Ca^{2+} and cAMP signals are plotted as dF/F_0 (fluorescence intensity change) and PKA signals are plotted as dR/R_0 (change of fluorescence ratio between 488 nm excitation and 405 nm excitation when imaging in the GFP emission channel). (L) Averaged fluorescent signals of Ca^{2+} (magenta), cAMP (cyan), and PKA (yellow) activities of HeLa cells shown in (K) ($n = 4$ cells co-expressing S1-GCaMP6f, S2-cAMPPr, S3-ExRaiAKAR, and miRFP from 2 cultures). Colored lines, mean; colored and shaded boundaries, standard error of mean.

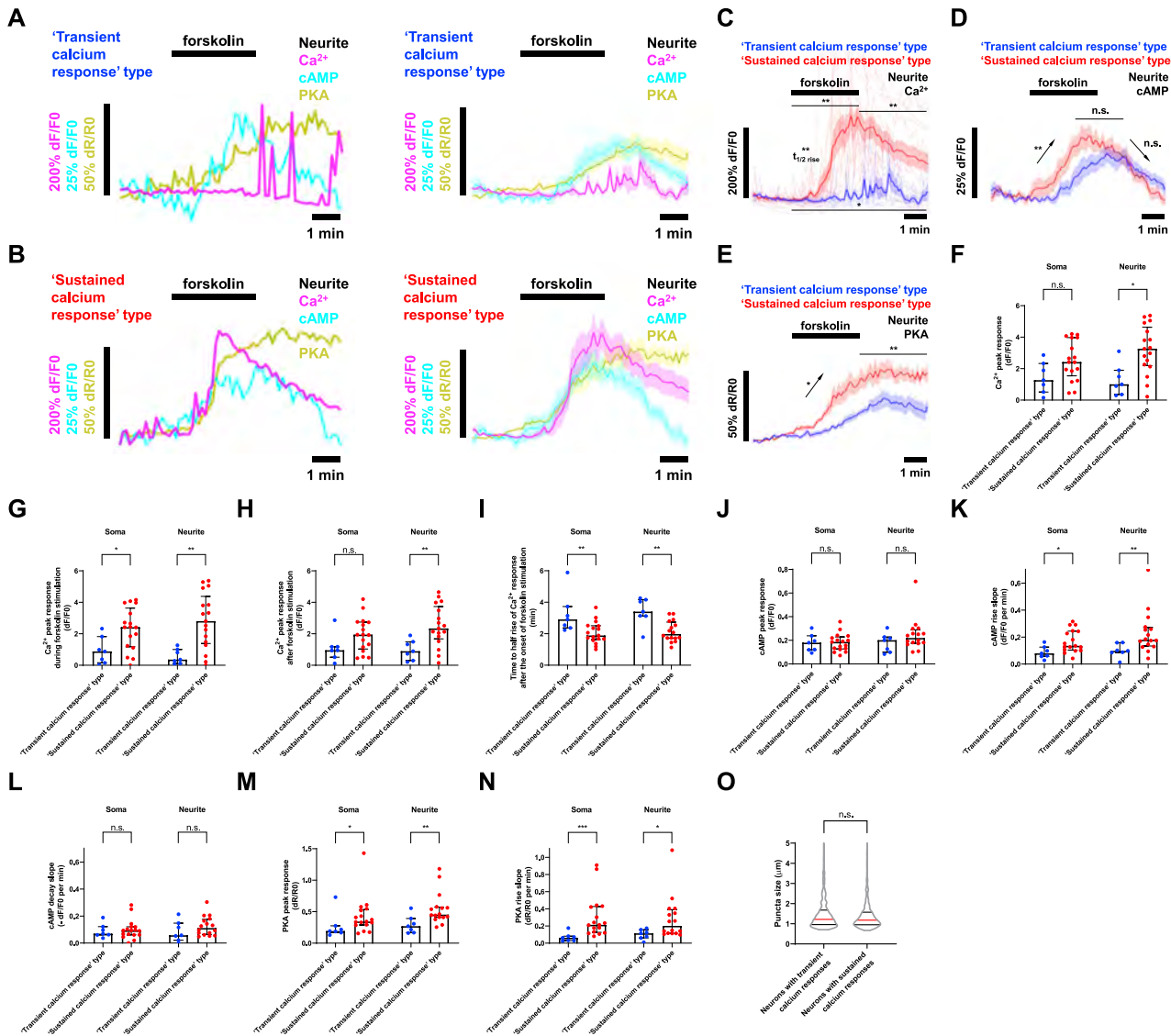
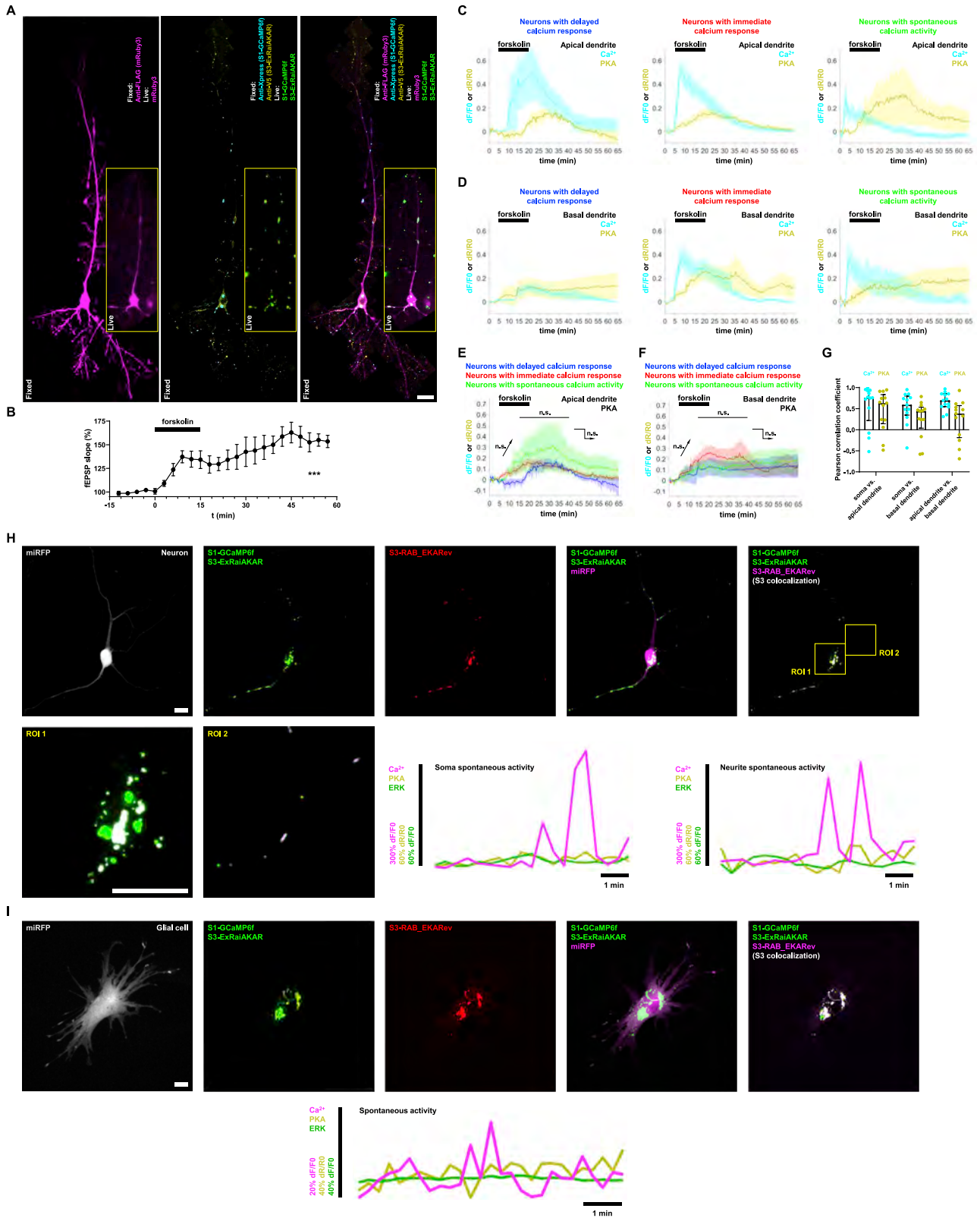


Figure S6. Waveform Analysis of Ca^{2+} , cAMP, and PKA Responses at Soma and Neurite Locations in Cultured Mouse Hippocampal Neurons under Forskolin Stimulation, Related to Figure 3

(A) Neurite Ca^{2+} , cAMP, and PKA activities from a representative neuron with a 'transient calcium response' at a neurite location (neurite locations were 20–60 μm away from soma) (left) and averaged across all neurons with 'transient calcium responses' (at neurite locations 20–60 μm away from soma) (right; $n = 7$ neurons from 7 cultures; colored lines throughout this figure, mean; colored, shaded boundaries throughout this figure, standard error of mean). (B) Neurite Ca^{2+} , cAMP, and PKA activities from a representative neuron with a 'sustained calcium response' at a neurite location (left) and averaged across neurons with 'sustained calcium responses' (right; $n = 16$ neurons from 12 cultures). (C) Averaged neurite Ca^{2+} activity from neurons with 'transient calcium responses' at neurite locations (blue; $n = 7$ neurons from 7 cultures) and from neurons with 'sustained calcium responses' at neurite locations (red; $n = 16$ neurons from 12 cultures) under 50 μM forskolin stimulation for 3 minutes. Thin and light colored lines, neurite Ca^{2+} activities from individual neurons. Results from statistical tests for peak responses over indicated time windows (horizontal lines), and times to half rise ($t_{1/2}$ rise), are indicated. (D) Averaged neurite cAMP activity for the neurons of (C). (E) Averaged neurite PKA activity for the neurons of (C). Results from statistical tests for the rise slope, decay slope, and peak response were indicated on (D) and (E) by the arrow near the rise phase, the arrow near the decay phase, and the horizontal line near the peak response, respectively. Throughout this figure: n.s., not significant; $p < 0.05$; $**p < 0.01$; $***p < 0.001$; Wilcoxon rank sum tests; see Table S4 for full statistics for Figure S6. (F) Ca^{2+} peak response over the entire recording. (G) Ca^{2+} peak response during forskolin stimulation, (H) Ca^{2+} peak response after the end of forskolin stimulation, (I) time to half rise of Ca^{2+} response after the onset of forskolin stimulation, (J) cAMP peak response, (K) cAMP rise slope, (L) cAMP decay slope, (M) PKA peak response, and (N) PKA rise slope for neurons with 'transient calcium responses' and neurons with 'sustained calcium responses' at soma and neurite locations (20–60 μm away from soma) under 50 μM forskolin stimulation for 3 minutes. Bar plots of medians with interquartile ranges are used throughout this figure, with individual values plotted as dots. For 'transient calcium responses' type neurons, $n = 7$ somata from 7 neurons from 6 cultures and $n = 7$ neurites from 7 neurons from 7 cultures. For 'sustained calcium responses' type neurons, $n = 17$ somata from 17 neurons from 12 cultures and $n = 16$ neurites from 16 neurons from 12 cultures. (O) Violin plots

(legend continued on next page)

of the punctum size of all puncta in the GFP channel in neurons with 'transient calcium responses' or neurons with 'sustained calcium responses' under 50 μ M forskolin stimulation for 3 minutes ($n = 512$ and 630 puncta in 5 and 5 neurons co-expressing S1-GCaMP6f, S2-cAMP α r, S3-ExRaiAKAR, and miRFP from 5 and 5 cultures for neurons with 'transient calcium responses' and neurons with 'sustained calcium responses', respectively). Red line, median; black line, interquartile ranges.



(legend on next page)

Figure S7. Waveform Analysis of Ca^{2+} and PKA Responses at Sites on Apical Dendrites and Basal Dendrites of CA1 Pyramidal Neurons in Acute Mouse Brain Slices under Forskolin Stimulation; for Some Combinations of SiRI Reporters of More Than One Color, Reporter Types Can Be Inferred during Live-Cell Imaging, without Requiring Post Hoc Immunostaining, Related to Figures 4, 5, and 7

(A) Maximum intensity projection (MIP) confocal images of the CA1 pyramidal neuron shown in Figures 4B and 4C in acute mouse brain slices (insets labeled 'Live') and after fixation and immunostaining (images labeled 'Fixed'). Scale bar, 20 μm . (B) Field excitatory postsynaptic potential (fEPSP) slopes (normalized to the baseline period before forskolin treatment) before, during, and after a 15-min-long 50 μM forskolin treatment starting at $t = 0$ min ($n = 7$ experiments on 7 slices from 5 mice co-expressing S1-GCaMP6f, S3-ExRaiAKAR, and mRuby3-6xFLAG, although imaging of these reporters was not performed). Black dots, mean; error bars, standard error of mean. $***p < 0.001$; Wilcoxon rank sum test for fEPSP slopes before and 45 minutes after the onset of forskolin treatment. (C) Ca^{2+} and PKA activities at locations on apical dendrites (30–100 μm away from soma) of CA1 pyramidal neurons from acute mouse brain slices averaged from neurons with delayed calcium responses (left; $n = 5$ neurons from 5 slices from 3 mice), immediate calcium responses (middle; $n = 6$ neurons from 2 slices from 2 mice), and spontaneous calcium responses (right; $n = 3$ neurons from 2 slices from 2 mice), under 50 μM forskolin treatment for 15 minutes. Throughout this figure: colored lines, mean; colored, shaded boundaries, standard error of mean. (D) Ca^{2+} and PKA activities at locations on the basal dendrites (10–40 μm away from soma) of CA1 pyramidal neurons from acute mouse brain slices, averaged across neurons with delayed calcium responses (left; $n = 5$ neurons from 5 slices from 3 mice), immediate calcium responses (middle; $n = 6$ neurons from 2 slices from 2 mice), and spontaneous calcium responses (right; $n = 3$ neurons from 2 slices from 2 mice), under 50 μM forskolin treatment for 15 minutes. Throughout this figure: colored lines, mean; colored, shaded boundaries, standard error of mean. (E) PKA activities at locations on the apical dendrites of CA1 pyramidal neurons from acute mouse brain slices, averaged across neurons with delayed calcium responses (blue; $n = 5$ neurons from 5 slices from 3 mice), immediate calcium responses (red; $n = 6$ neurons from 2 slices from 2 mice), and spontaneous calcium responses (green; $n = 3$ neurons from 2 slices from 2 mice), under 50 μM forskolin treatment for 15 minutes. For (E) and (F), n.s., not significant; Kruskal-Wallis analysis of variance for rise slopes (arrow near the rise phase), peak responses (horizontal line near the peak response), and durations of PKA activation (arrow on the right hand side of the panel), followed by post hoc test via Dunn's test. See Table S4 for full statistics for Figure S7. (G) Bar plot of Pearson correlation coefficients of the Ca^{2+} or PKA responses recorded from soma-, apical dendrite-, and basal dendrite- localized puncta within single CA1 pyramidal neurons ($n = 13$ neurons from 6 slices from 3 mice). Bar plots of medians with interquartile ranges are used, with individual values plotted as dots. (H) Maximum intensity projection (MIP) confocal images of a live cultured mouse hippocampal neuron co-expressing S1-GCaMP6f (a GFP based reporter), S3-ExRaiAKAR (a GFP based reporter), S3-RAB_EKARev (an RFP based reporter), and the cell morphological marker mRFP, as well as the recorded fluorescent signals of spontaneous Ca^{2+} (magenta), PKA (yellow), and ERK (green) activities at soma and at locations along neurites. Throughout this figure: in the composite images (those labeled 'S3 colocalization') from GFP and RFP channels, GFP and RFP channels were pseudo-colored in green and magenta, respectively, thus the puncta appearing in both channels would have white color in the composite images; puncta appearing in both GFP and RFP channels were identified as the puncta containing both S3-ExRaiAKAR (in the GFP channel) and S3-RAB_EKARev (in the RFP channel); puncta that appeared in the GFP channel only, were identified as puncta of S1-GCaMP6f. No punctum appeared in the RFP channel only. Scale bars, 20 μm . (I) Maximum intensity projection (MIP) confocal images of a live cultured mouse hippocampal glial cell co-expressing S1-GCaMP6f, S3-ExRaiAKAR, S3-RAB_EKARev, and the cell morphological marker mRFP, as well as recorded fluorescent signals of spontaneous Ca^{2+} (magenta), PKA (yellow), and ERK (green) activities. Scale bar, 20 μm .